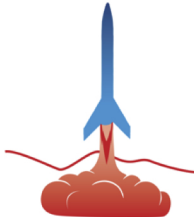
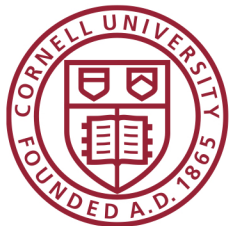


---

**Caleb Farrelly [CLF77]**  
**Cornell Rocketry Team**  
**Spring 2025 Masters Design Report**  
**1250lbf Regeneratively Cooled Bipropellant Rocket**  
**Engine**

**Cornell University**  
**Sibley School of Mechanical and Aerospace Engineering**  
**124 Hoy Road**  
**Ithaca, NY 14850**



**SPACEPORT AMERICA®**  
**CUP**

# 1 Executive Summary

## 1. What are the desired function(s) of your design?

The primary desired function of the design is to serve as a development platform for the Cornell Rocketry Team to advance the capability of designing, building, and testing bipropellant rocket engines. This engine will use ethanol as the fuel and nitrous oxide ( $\text{N}_2\text{O}$ ) as the oxidizer, providing a familiar foundation for gaining expertise in liquid bipropellant propulsion systems.

The design must deliver reliable, efficient, and repeatable performance while incorporating modern manufacturing techniques, such as metal additive manufacturing, to streamline fabrication and enable complex geometries that enhance engine performance. Critical components, including the combustion chamber and nozzle, will utilize additive manufacturing to allow for rapid iteration, optimized thermal management, and lightweight, integrated designs.

Furthermore, the engine should be designed for modularity to support future research and development efforts. This includes the ability to integrate additional instrumentation, such as temperature, pressure, and flow sensors, to monitor critical parameters during testing. It must also be adaptable for functional upgrades, such as implementing a throttling pintle injector for variable thrust capability. These features will ensure that the engine serves as a robust experimental platform for iterative learning, testing new ideas, and advancing the team's expertise in propulsion system development.

## 2. What constraints related to the main function(s) must your design satisfy?

### 1.1 Constraints

#### 1.1.1 Additive Manufacturing Compatibility

- The combustion chamber and nozzle must be entirely 3D-printed using metal additive manufacturing techniques.
- The design must conform to the capabilities and limitations of the selected additive manufacturing process:
  - **Maximum height:** The components must fit within a print bed with a height limit of **250 mm**.
  - **Minimum feature size:** The design must respect a minimum feature size of **0.3 mm** to ensure all features are resolvable by the printer.
  - **Overhang angle:** Unsupported overhangs must not exceed **45 degrees**. Steeper angles will require the inclusion of support structures or design modifications.
  - **Bridge gap:** Unsupported bridge gaps are limited to **2 mm**, necessitating careful planning for flow passages and internal features.
- Material properties used in the additive manufacturing process, such as thermal conductivity, strength, and durability, must align with the engine's operating conditions and withstand thermal and structural loads.

### **1.1.2 Thermal and Structural Durability**

- The combustion chamber and nozzle must endure high thermal loads and pressures generated by the combustion of ethanol and nitrous oxide.
- Materials and geometry must provide sufficient thermal resistance and structural integrity under both transient and steady-state conditions.
- The design must account for surface roughness and anisotropy inherent to the additive manufacturing process.

### **1.1.3 Dimensional Constraints**

- The design must comply with the dimensional constraints of the testing facilities and launch vehicle integration.
- Compactness must be maintained to optimize thrust-to-weight ratio and facilitate efficient testing setups.

### **1.1.4 Ease of Post-Processing**

- The design must minimize the need for extensive post-processing (e.g., machining, polishing), while maintaining required tolerances for critical features such as injector orifices and sealing surfaces.
- Internal cooling channels, injector ports, and other intricate features must be accessible for inspection and cleaning after fabrication.

### **1.1.5 Future Modification and Instrumentation**

- The design must be modular to allow for future additions, such as:
  - Instrumentation (e.g., thermocouples) for monitoring chamber conditions.
  - Functional upgrades like a throttling pintle injector
- Modularity should enable future improvements without requiring significant redesigns and re-manufacturing.

## **3. What are the performance objectives of your design? (Give quantitative metrics as much as possible).**

- Achieve a thrust of 1250 lbf.
- Optimize the cooling effectiveness to ensure the chamber wall temperatures remain below the 250C material limit.
- The engine must operate under a chamber pressure of 350 psi and sustain peak thermal and structural loads for a burn time of 10 seconds, producing at least 25,000 Newton seconds of impulse

- The engine should achieve a specific impulse of at least 180s.
- The engine should be able to be reused at least 10 times.

#### **4. What alternative design concepts were considered?**

- Bell nozzle versus TIC nozzle designs.
- Pintle injector versus showerhead injector for fuel and oxidizer delivery.
- Materials trade-offs: Inconel, aluminum, and copper for the chamber and nozzle.
- CNC machined injector body vs 3D printed injector body
- Fully 3D printed combustion chamber

#### **5. What analyses were used to select among these alternative design concepts?**

- Finite Element Analysis (FEA) for structural and thermal stress evaluation.
- MATLAB-based analysis for injector and cooling channel design.
- RPA 4.01 (Rocket Propulsion Analysis) for combustion optimization, thermal simulations, thrust optimization, nozzle design.
- Trade studies were used extensively to objectively compare qualitative aspects of different concepts

#### **6. What industry or society standards were used to inform or evaluate your design?**

- **SAE AS5857 - O-ring and Sealing Groove Design:**

This standard specifies the design requirements for O-ring gland dimensions, including groove width, depth, and edge tolerances for aerospace and high-pressure applications. The injector and combustion chamber sealing interfaces were designed with Parker O-ring Handbook guidelines based on SAE AS5857 standards.

- **ASME B1.1 - Unified Inch Screw Threads (UTS):**

Threaded components such as the injector bolts, manifold retaining rings, and sensor ports followed ASME B1.1 specifications. Threads will be machined using the Class 2A fit for external threads and Class 2B for internal threads to balance ease of assembly and reliable mechanical engagement.

- **ASME B18.2.1 - Square and Hex Bolt Standards:**

All bolts and fasteners used in the engine assembly conformed to ASME B18.2.1 specifications for head size, thread length, and mechanical strength.

#### **8. Evaluate your design, relative to its function(s) and constraints. How well did your design meet each of the performance objectives?**

The design successfully met its performance objectives in simulations. The thrust, thermal, and structural parameters were validated to achieve 1250 lbf thrust while keeping the wall temperature well below 500K. The design was able to be designed to be 3D printed almost entirely. Experimental validation remains to be conducted which may prove the analysis wrong. Accurately modeling the combustion and fluid flow within the combustion chamber is quite involved, and out of the scope of this project.

## 2 Design Overview

The Cornell Rocketry Team's 1250 lbf bipropellant rocket engine is designed as a high-performance liquid rocket engine using ethanol as the fuel and nitrous oxide ( $\text{N}_2\text{O}$ ) as the oxidizer. This bipropellant combination was selected for its ease of handling, and proven performance in collegiate and industry rocket engines. Ethanol is a widely used hydrocarbon fuel due to its relatively high energy density and compatibility with regenerative cooling designs, while nitrous oxide offers a self-pressurizing oxidizer that simplifies propellant feed system design.

A bipropellant engine operates by injecting fuel and oxidizer into the combustion chamber, where they mix and combust, producing high-temperature gases. These gases are accelerated through a converging-diverging nozzle, generating thrust. The engine employs a pressure-fed propellant delivery system, relying on pressurized propellant tanks to feed the fuel and oxidizer through the injector assembly.

The engine's injector system uses a pintle injector, a configuration known for its efficient mixing, potential for throttling capability, and combustion stability. The pintle injector could in the future be modified to allow independent throttling of fuel and oxidizer, enabling precise thrust control and optimal mixture ratio adjustments during engine operation. This capability is critical for missions requiring dynamic thrust modulation, such as precision landings or controlled ascents.

Thermal management is achieved through regenerative and film cooling. Ethanol flows through regenerative cooling channels along the combustion chamber walls, absorbing heat and preventing thermal failure. Film cooling orifices inject a thin layer of ethanol directly onto the inner chamber walls, providing additional thermal protection in high-heat regions, particularly for nozzle throat, where heat flux can reach  $2.5 \text{ MW/m}^2$ .

The engine is designed and optimized for metal additive manufacturing, enabling the production of complex internal geometries that enhance fuel and oxidizer flow distribution, thermal management, and structural integrity. This approach reduces overall engine mass while minimizing manufacturing costs and lead times.

The 1250 lbf liquid engine is the most ambitious propulsion project undertaken by the Cornell Rocketry Team to date. Its development builds on the team's extensive experience with hybrid propulsion systems, integrating lessons learned from previous projects such as the Volta III hybrid rocket. This project pushes the team into advanced liquid propulsion technologies, expanding the team's technical expertise and industry visibility.

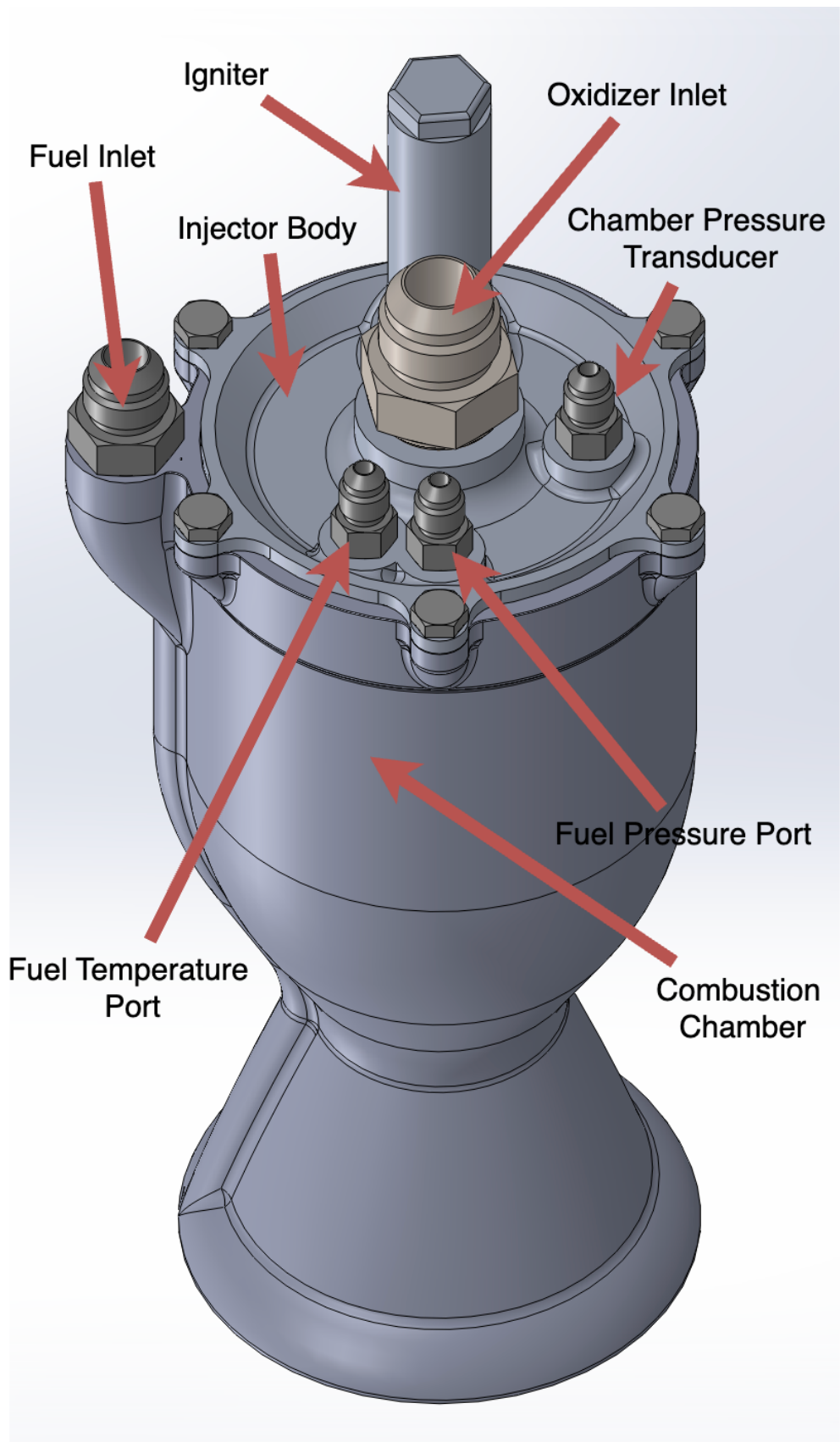


Figure 1: Full assembly view of the 1250 lbf bipropellant rocket engine

### 3 Igniter Design

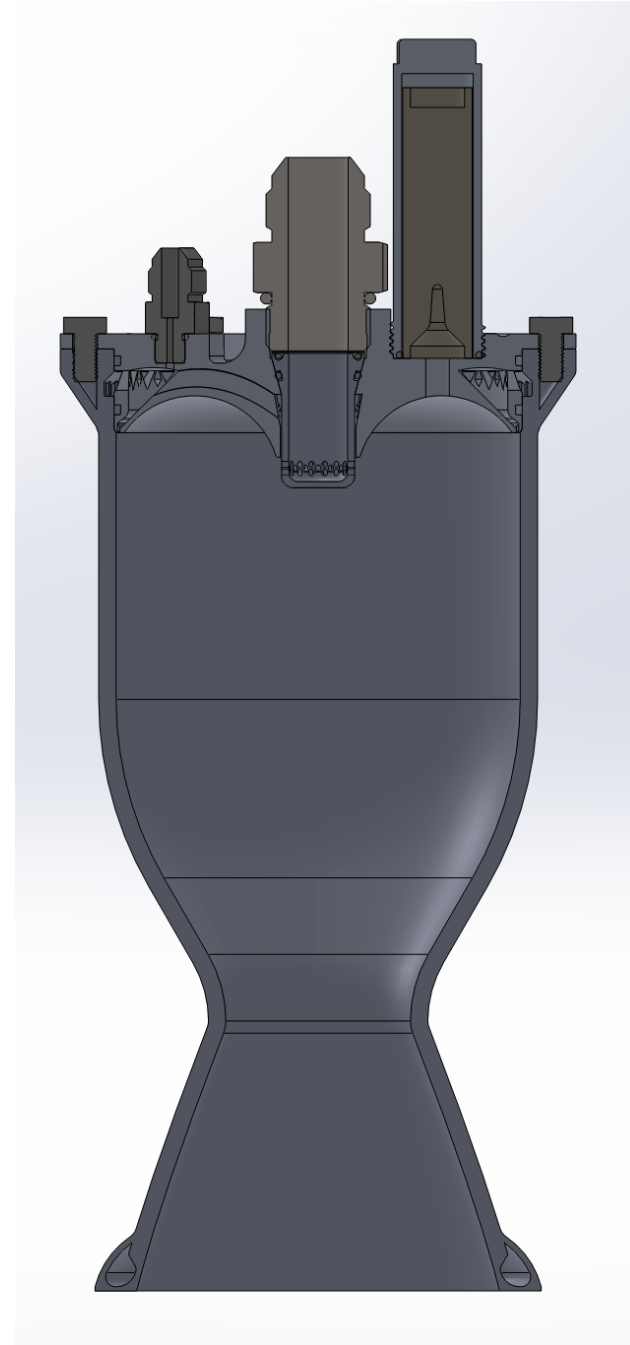


Figure 2: Igniter assembly view

The igniter is a crucial component in the ethanol/nitrous oxide engine, as it initiates combustion and ensures stable ignition of the propellants. Designing the igniter for this engine requires careful consideration to prevent overpressure events, ensure reliable ignition under varying conditions, and integrate with the pintle injector manifold.

### 3.1 Ignition Requirements

For the ethanol/nitrous oxide engine, the igniter must:

- Reliably ignite the propellants without causing a hard start or damaging the combustion chamber.
- Provide sufficient heat flux to the ethanol and ( $N_2O$ ) spray pattern to ensure rapid and uniform ignition.
- Minimize the risk of debris or residue that could disrupt the flow through the injector.
- Be compact, reusable (if possible), and compatible with the injector and chamber configuration.

### 3.2 Solid Motor Cartridge Igniters

The selected baseline for ignition is a solid motor cartridge igniter, which is available off the shelf as a Quest Q-jet motor and burns independently of the chamber conditions. A solid cartridge igniter simplifies integration and ensures consistent heat flux to the ethanol/nitrous oxide propellants.

#### 3.2.1 Baseline Design

The proposed igniter is based on a Quest 18 mm motor, with a burn time of approximately 1.5 seconds [?]. This motor is positioned to fire directly into the pintle injector's spray pattern, providing uniform heating to the propellants as they are atomized.

##### Advantages:

- **Independent Combustion:** The solid motor burns consistently regardless of chamber pressure or propellant flow conditions, ensuring reliable ignition.
- **No Debris Ejection:** Unlike loose APCP igniters, the cartridge design fully contains the burning propellant, preventing ejection of chunks that could cause a hard start.
- **Ease of Integration:** The solid motor cartridge is compact, easy to install, and fires directly into the pintle spray, ensuring optimal heat transfer.
- **Reduced Maintenance:** Compared to black powder igniters, the APCP-based cartridge produces minimal corrosive residue, reducing wear and tear on the chamber.

##### Challenges:

- **High Heat Flux:** The high-temperature gases produced during ignition could potentially damage chamber walls or the pintle if not carefully controlled.
- **Limited Burn Duration:** The 1.5-second burn time must be sufficient to ignite the ethanol/nitrous propellants; insufficient ignition time could lead to incomplete combustion initiation.

### 3.3 Advanced Ignition Options: N<sub>2</sub>O Torch Igniter

An advanced option for ignition is a nitrous oxide (N<sub>2</sub>O) monopropellant torch igniter. This system uses the catalytic decomposition of nitrous oxide to produce high-temperature gases for ignition. While more complex than a solid motor cartridge, this method offers several advantages specific to ethanol/nitrous engines.

#### Advantages:

- **Clean Combustion:** The catalytic decomposition of N<sub>2</sub>O produces minimal residue, ensuring a clean chamber environment.
- **Chamber Independence:** Like the solid motor, the torch igniter is choked so it operates independently of chamber conditions, providing consistent ignition performance.
- **Heat Control:** By regulating the flow rate of nitrous oxide, the torch igniter can deliver adjustable heat flux tailored to the ignition needs of the engine.

#### Challenges:

- **System Complexity:** The need for a catalytic bed and controlled flow system increases hardware complexity and integration challenges.
- **Development Time:** The N<sub>2</sub>O torch igniter requires further testing to ensure compatibility with the pintle injector and ethanol spray.

### 3.4 Igniter Placement and Integration

For both solid motor cartridges and N<sub>2</sub>O torch igniters, the placement within the engine is critical. The igniter is positioned directly adjacent to the pintle injector, ensuring that the igniter flame impinges on the atomized spray pattern. This direct ignition ensures uniform and rapid startup of the engine, and minimises the risk of a hard-start.

### 3.5 Comparative Analysis

Criteria	Solid Motor Cartridge	N <sub>2</sub> O Torch Igniter
Combustion Residue	Minimal	None
Ignition Consistency	High	High
Complexity	Low	High
Adjustability	None (fixed burn)	Adjustable
Development Effort	Mature technology	Requires further development

Table 1: Comparison of Solid Motor and N<sub>2</sub>O Torch Igniters

### 3.6 Igniter Conclusion

The baseline igniter for the ethanol/nitrous oxide engine is the solid motor cartridge igniter, specifically the Aerotech Q-Jet 18 mm motor. This choice offers a reliable, low-complexity ignition solution that is compatible with the pintle injector and ensures consistent ignition.

While the N<sub>2</sub>O monopropellant torch igniter presents an exciting alternative due to its clean combustion and adjustable heat flux, its increased complexity and development effort make it more suitable for future iterations of the engine.

## 4 Injector Design: Pintle vs. Showerhead

The injector is one of the most critical components in liquid rocket engines, responsible for introducing, atomizing, and mixing propellants in the combustion chamber. It determines the combustion efficiency, combustion stability, and thermal profile within the combustion chamber, making its design a critical aspect of engine performance. Two primary injector designs are considered in this trade study: the **pintle injector** and the **showerhead injector**. This section explores the operating principles, advantages, limitations, and suitability of each design for various rocket engine applications.

### 4.1 Pintle Injector

#### 4.1.1 Design and Operating Principles

The pintle injector consists of a central pintle element, through which one propellant—typically the oxidizer—flows axially. The second propellant—commonly the fuel—is introduced radially or tangentially through an annular slot or discrete orifices around the pintle. As the two propellants impinge on each other, they generate a spray cone and a turbulent recirculation zone downstream of the pintle tip, leading to highly efficient mixing and combustion.

In more advanced designs, the pintle injector's geometry allows precise control over the mixing of the propellants by adjusting the pintle's axial position. This feature, combined with its inherent simplicity, makes it a preferred design for engines requiring high stability and variable thrust.

**Historical Use:** The pintle injector gained prominence in the Apollo Lunar Module Descent Engine (LMDE). The injector's ability to throttle smoothly and deliver stable combustion under varying conditions was pivotal for the success of precision lunar landings. The same fundamental design has been employed in numerous other rocket engines, including the SpaceX Merlin engines.

#### 4.1.2 Advantages

- **Superior Combustion Stability:** The pintle's self-contained recirculation zone promotes effective mixing and mitigates acoustic and thermal instabilities, making it inherently more stable than multi-element designs.

- **Exceptional Throttling Capability:** Pintle injectors can achieve deep throttling ratios (up to 10:1 or greater) with minimal performance degradation, making them suitable for reusable and landing systems.
- **Manufacturability and Cost-Effectiveness:** Compared to the showerhead injector, the pintle's simpler geometry reduces manufacturing complexity, especially for small-to-medium thrust engines.
- **Proven Heritage:** Decades of successful operation in space missions demonstrate the reliability and robustness of the pintle injector design.
- **Adaptability to Diverse Propellants:** Pintle injectors have been demonstrated with various combinations of cryogenic, storable, and hypergolic propellants.

#### 4.1.3 Challenges and Limitations

- **Flow Asymmetry:** The pintle injector's flow dynamics can lead to asymmetric combustion and uneven heat flux distributions on the chamber walls, which may lead to chamber failure.
- **Thermal Stress and Erosion:** The high temperatures and high oxidizer environment near the pintle tip can increase erosion rates and thermal stress, potentially shortening component life.

## 4.2 Showerhead Injector

### 4.2.1 Design and Operating Principles

The showerhead injector consists of a faceplate with an array of small orifices through which propellants are injected into the combustion chamber. Each orifice produces its own spray plume, resulting in multiple discrete mixing zones. The showerhead design focuses on distributing propellants uniformly across the combustion chamber to achieve even combustion and thermal loading.

This injector design has been widely used in high-thrust engines, such as the RS-25 (Space Shuttle Main Engine) and RL10, where precise control of propellant distribution is critical.

### 4.2.2 Advantages

- **Uniform Propellant Distribution:** The distributed flow from multiple orifices ensures even heat flux and reduces the risk of localized hotspots, promoting longer chamber life.
- **Scalability:** The modular nature of the design allows for easy scaling by increasing or decreasing the number and size of orifices.
- **Thermal Management:** Uniform combustion mitigates thermal gradients, reducing thermal stress on chamber walls.

- **Performance at High Thrust Levels:** The showerhead design excels in engines requiring extremely high thrust outputs, as it evenly distributes large mass flow rates.

#### 4.2.3 Challenges and Limitations

- **Susceptibility to Combustion Instabilities:** The absence of natural recirculation zones increases the likelihood of acoustic and thermal instabilities.
- **Throttling Limitations:** Fixed orifice geometries limit the showerhead's ability to throttle effectively without significant modifications to the flow control systems.
- **Manufacturing Complexity:** Precision machining of multiple orifices adds cost and complexity, particularly for engines requiring highly uniform flow.
- **Non-Optimal Mixing:** Mixing efficiency depends heavily on the orifice layout and may require extensive testing to optimize. The showerhead is not optimal for liquid-liquid bipropellant engines due to poor atomization.

### 4.3 Comparative Analysis

Criteria	Pintle Injector	Showerhead Injector
Combustion Stability	High; robust against instabilities	Moderate; prone to instabilities
Throttling Capability	Deep throttling (up to 10:1)	Limited; fixed orifice geometry
Mixing Efficiency	Excellent; natural recirculation	Moderate; depends on orifice layout
Heat Flux Distribution	Asymmetric; requires cooling	Uniform; manageable cooling demands
Manufacturability	Relatively simple	Complex; precision machining required
Scalability	Suitable for small-to-medium thrust engines	Ideal for high-thrust applications

Table 2: Comparison of Pintle and Showerhead Injectors

## 4.4 Injector Pintle Design

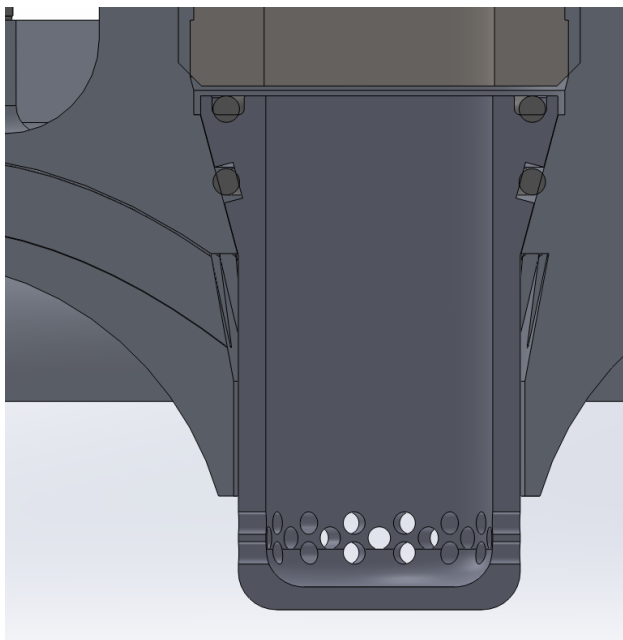


Figure 3: View of the pinte injector and Injector Manifold

The injector system consists of two primary components: the **pinte insert** and the **pinte annulus**. These components form the basis of the fuel-oxidizer delivery system. Fuel is injected axially through the annulus, while oxidizer (nitrous oxide) is injected radially through 44 orifices drilled into the pinte tip. The oxidizer and fuel impinge at the interface, creating a high-shear, turbulent mixing zone, which causes effective atomization and mixing of the propellants.

### 4.4.1 Pinte Alignment

Maintaining precise concentric alignment between the pinte insert and the outer annulus is essential for ensuring symmetric propellant flow and preventing asymmetric combustion, which could damage the combustion chamber walls. Any deviation in alignment can cause uneven oxidizer-fuel mixing, leading to incomplete combustion, reduced specific impulse ( $I_{sp}$ ), and even combustion instabilities such as chugging or hard starts.

The mechanical interface between the pinte and the annulus is designed with tight tolerances, ensuring minimal misalignment. The orifices characteristics for Nitrous injection were determined with empirical data from the Waxman paper "*An Investigation of Injectors for Use with High Vapor Pressure Propellants with Applications to Hybrid Rockets*" [?]

### 4.4.2 Fuel and Oxidizer Flow Characteristics

**Oxidizer Flow Regulation:** According to the findings in Benjamin Waxman's paper *An Investigation of Injectors for Use with High Vapor Pressure Propellants with Applications*

*to Hybrid Rockets*, nitrous oxide injection operates in a **near-critical flow** regime rather than a fully choked flow condition due to the thermodynamic properties of nitrous oxide. While traditional gases can easily achieve fully choked flow when the pressure ratio ( $P_{\text{upstream}}/P_{\text{downstream}}$ ) exceeds the critical value of approximately 1.89 for diatomic gases, liquid nitrous oxide's high vapor pressure and compressibility introduce additional complexity.

The Waxman study demonstrated that nitrous oxide experiences a *pseudo-choked* condition near the orifice exit, where the flow rate stabilizes but may still respond to minor downstream pressure fluctuations. This occurs because nitrous oxide behaves as a saturated vapor-liquid mixture at typical injector inlet conditions, causing a flow regime shift depending on injector pressure and temperature.

Despite this complexity, the mass flow rate is still largely controlled by the upstream pressure, minimizing the effect of downstream pressure oscillations when the upstream-to-downstream pressure ratio is sufficiently high. This quasi-stable condition ensures relatively consistent oxidizer flow, making nitrous oxide viable for pressure-fed bipropellant engines with carefully designed injector geometries. In the engine's pintle injector, the orifice dimensions are selected based on empirical flow data from the Waxman paper, ensuring predictable mass flow behavior under operating conditions.

#### 4.4.3 Orifice Design and Validation

The pintle orifice design was selected based on experimental data from the Waxman paper, which provided validated flow characteristics for an orifice with a diameter of 1.5 mm and a length of 3.2 mm. This specific orifice size was chosen due to its well-characterized mass flow performance, enabling accurate prediction of the oxidizer flow rate under various pressure conditions.

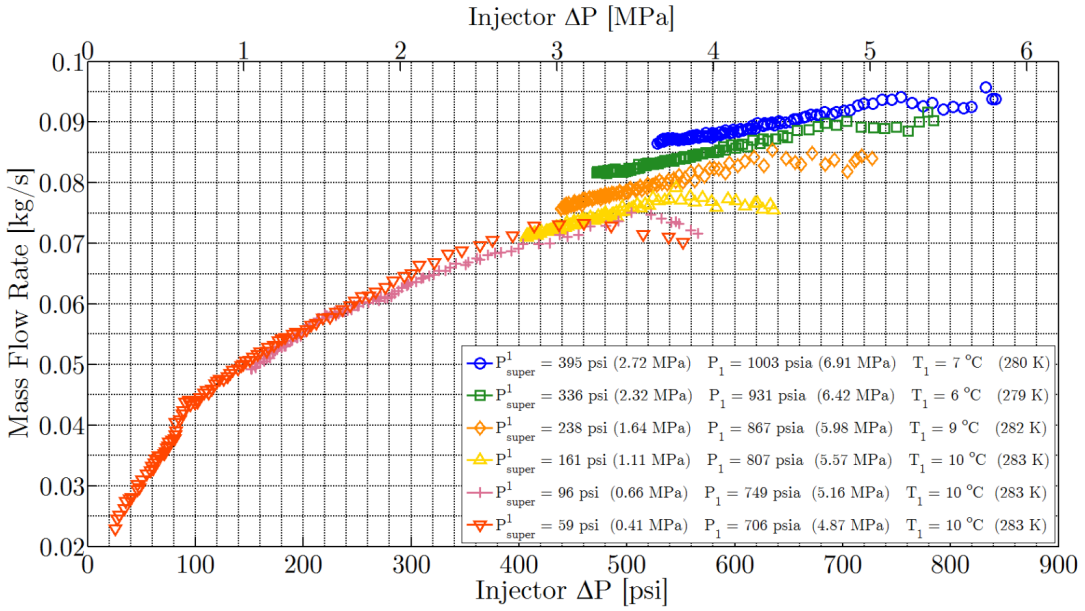


Figure A.17:  $\dot{m}$  vs.  $\Delta P$  and supercharge for injector number 6 with carbon dioxide.

Figure 4: Waxman 1.5mm diameter, 3.2mm length orifice data

The Imperial College London (ICL) team reported using a similar pintle design, achieving a pressure drop of 4.1 bar (59.47 psi) across 48 orifices, resulting in a total oxidizer mass flow rate of 1.55 kg/s. This corresponds to a flow rate of approximately 0.0322 kg/s per orifice, matching Waxman's experimental results for CO<sub>2</sub> as an analog for N<sub>2</sub>O.

**Mass Flow Rate Calculation:** Based on the desired oxidizer mass flow rate of 2.5788 kg/s for the engine, the required number of orifices was calculated as follows:

$$n = \frac{\dot{m}_{ox}}{\dot{m}_{\text{orifice}}} = \frac{2.5788}{0.06} \approx 43 \quad (1)$$

Given that three rows of orifices were selected, each row contains approximately 14 orifices:

$$n_{\text{row}} = \frac{43}{3} \approx 14.33 \quad (2)$$

#### 4.4.4 Injection Pressure and Stiffness

The injector's effect on combustion stability is heavily influenced by its **injection stiffness**, defined as:

$$\text{Stiffness} = \frac{P_{\text{feed}} - P_{\text{chamber}}}{P_{\text{chamber}}} \quad (3)$$

Injection stiffness must be maintained at or above 30% to remain insensitive to combustion chamber pressure fluctuations caused by combustion instabilities. A stiffness of 60% or higher is recommended to ensure stable oxidizer and fuel delivery even under off-nominal conditions.

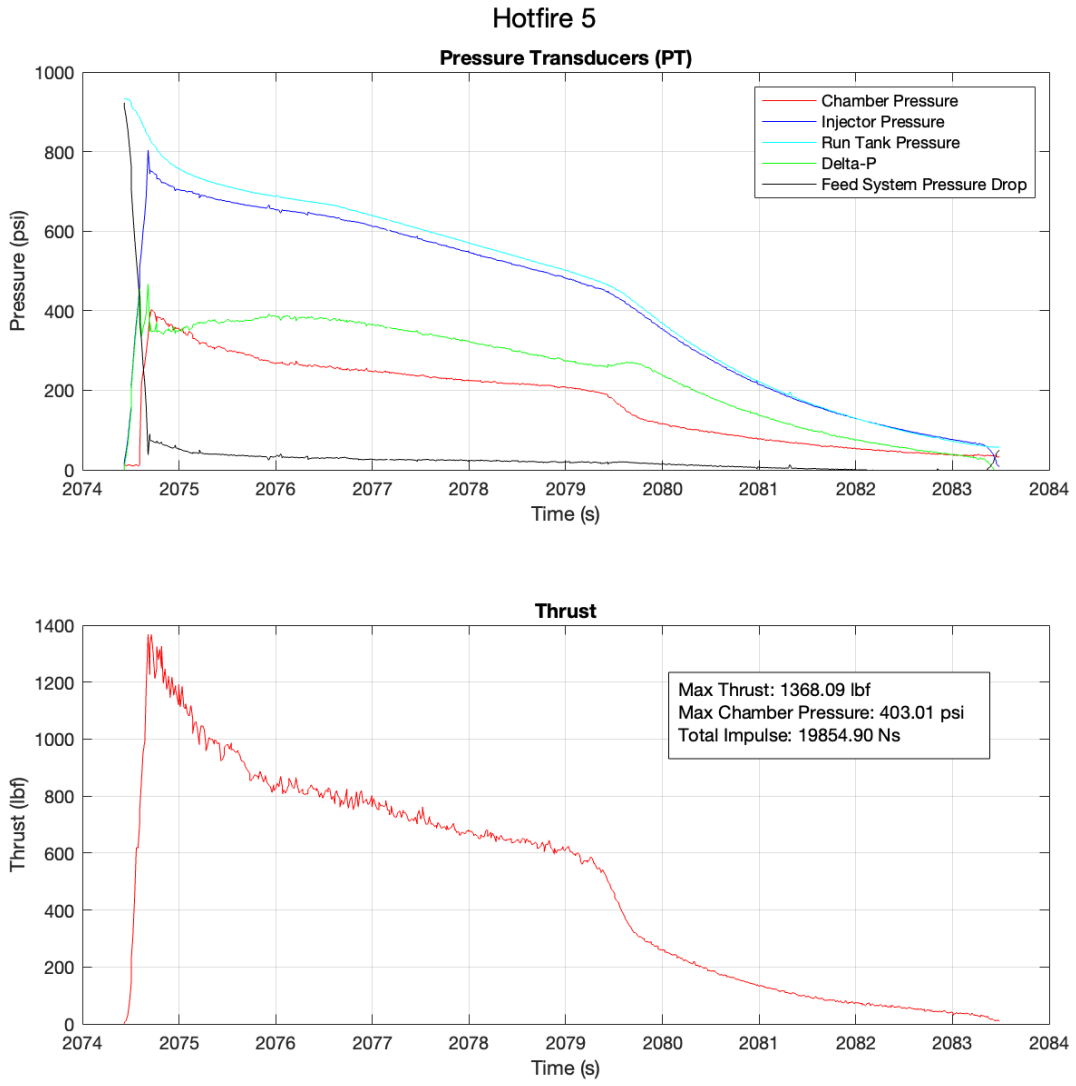


Figure 5: Volta III Delta-P Data

Based on CRT hybrid engine data from the Volta III engine, a pressure delta ( $\Delta P$ ) of approximately 390 psi was assumed. This value aligns with previous injector configurations and provides sufficient stiffness to maintain critical flow conditions in the oxidizer orifices [?]

## 4.5 Injector CAD Images

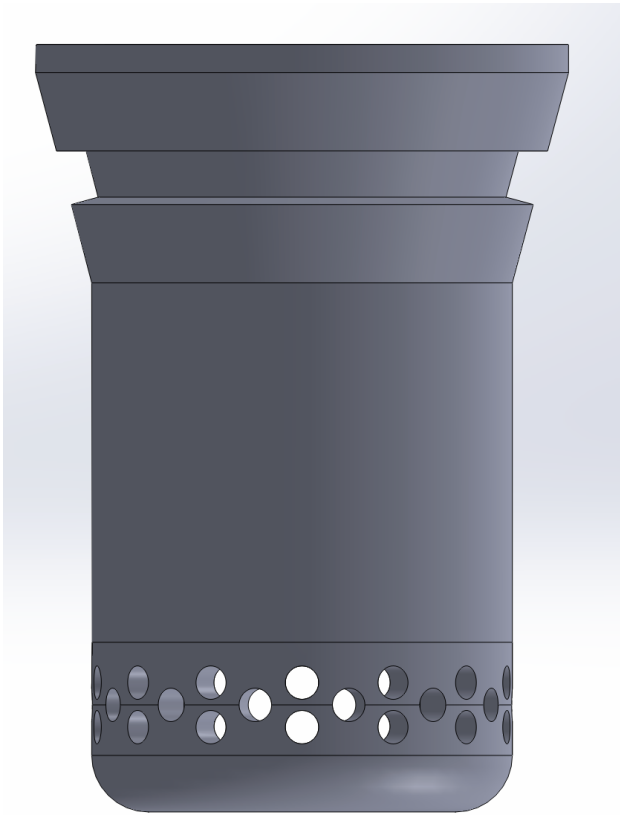


Figure 6: Injector pintle design used for regulating oxidizer flow into the combustion chamber. The geometry ensures optimal mixing of the oxidizer and fuel for efficient combustion.

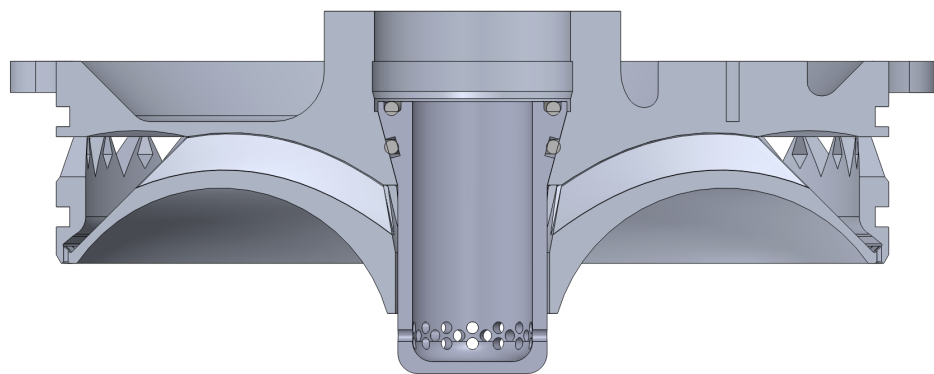


Figure 7: Cross-section of the injector manifold showing the internal flow paths for oxidizer distribution. The design ensures uniform flow to the injector pintle.

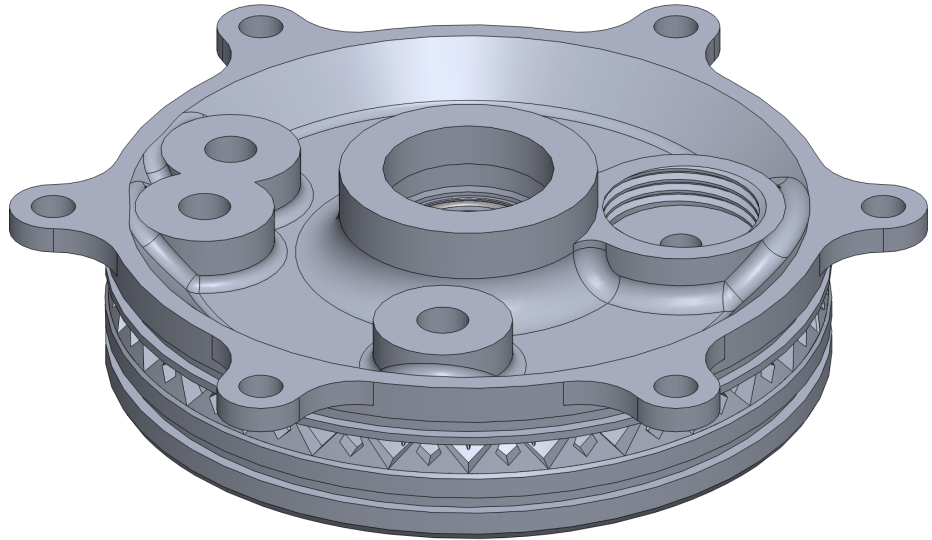


Figure 8: Isometric view of the injector manifold highlighting its external features and mounting points.

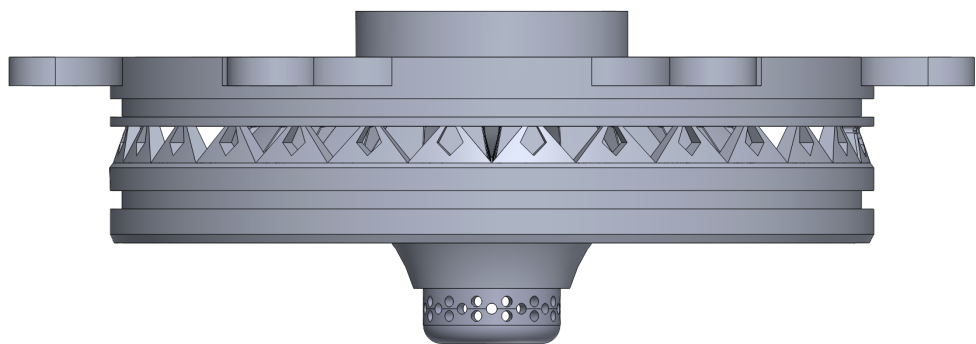


Figure 9: Side view of the injector manifold showing the integration with the combustion chamber assembly.

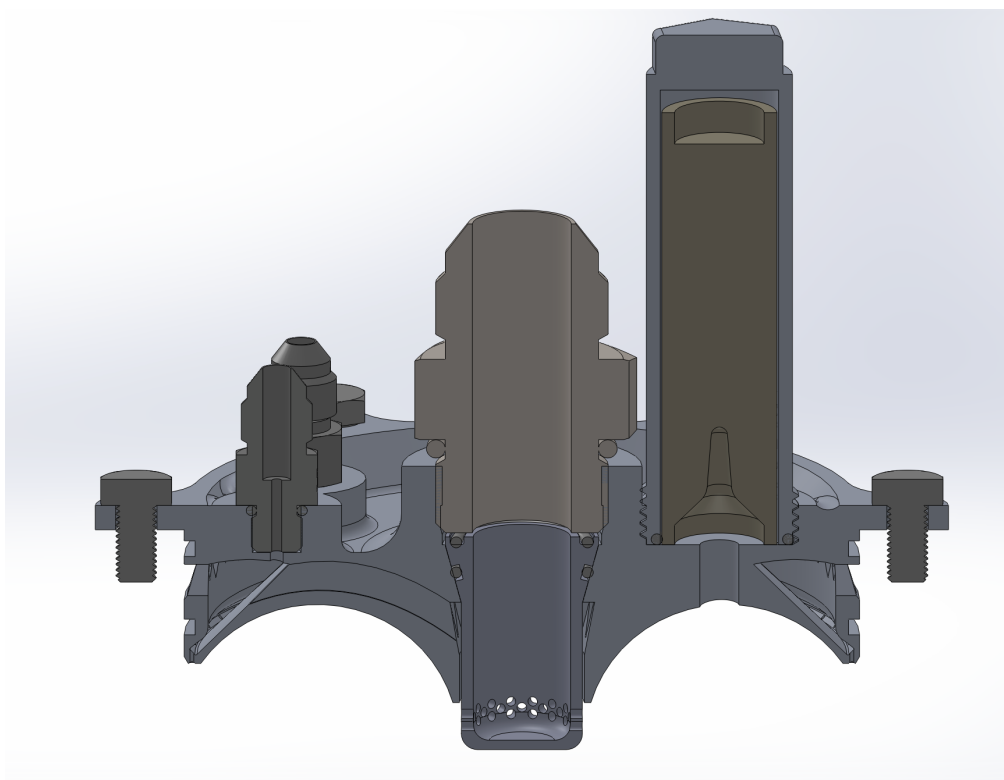


Figure 10: Injector assembly featuring all integrated components. This view shows the assembled state for proper alignment and sealing.

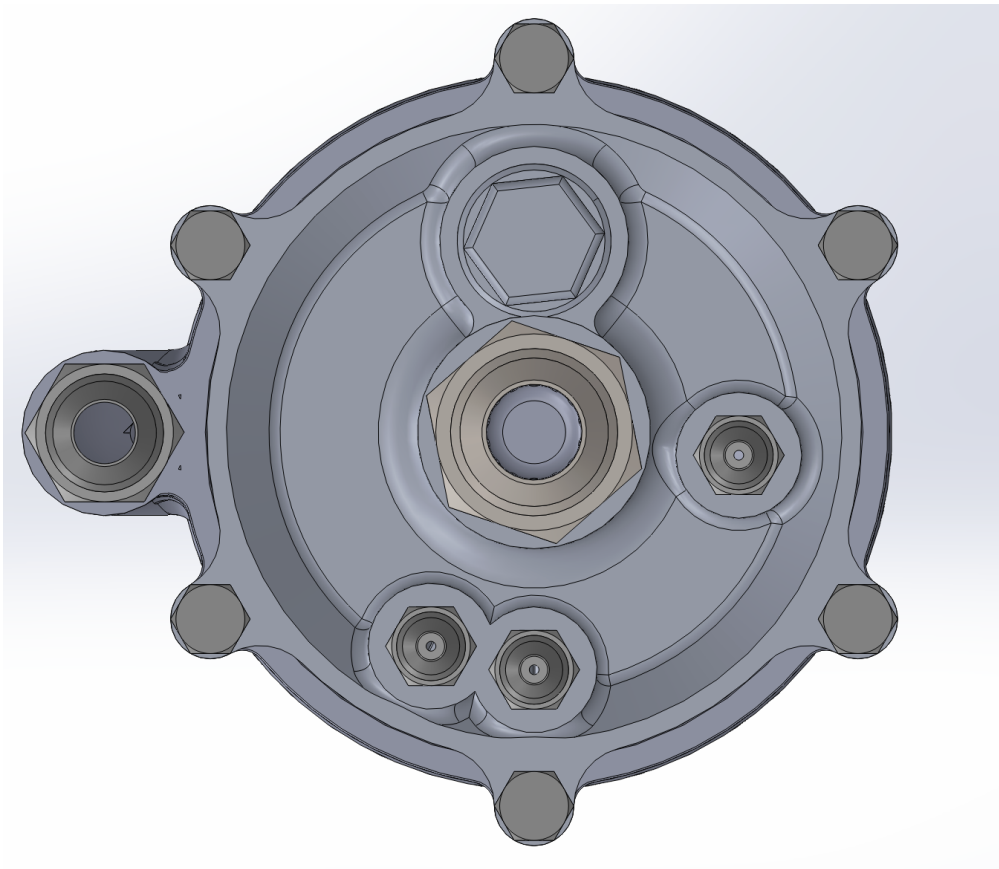


Figure 11: Top-down view of the combustion chamber and injector assembly. Demonstrates the alignment and layout of the injector with the chamber.

## 5 Fuel Selection Trade Study

### 5.1 Ethanol vs. IPA vs. Kerosene

Ethanol was selected due to its lower viscosity and cleaner combustion compared to kerosene. IPA was less desirable due to higher cost and similar properties.

### 5.2 Oxidizer: N<sub>2</sub>O

Nitrous oxide was chosen due to our extensive experience working with this oxidizer. It is also not a cryogenic so this makes procurement much easier than LOX for example.

## 6 Motor Calculations

### 6.1 O/F and Chamber Pressure Selection

To determine the most optimal O/F ratio for this application I plotted specific impulse vs O/F ratio for a variety of chamber pressures. I selected a chamber pressure of 350 PSI and

an O/F of 3.8 because there was little ISP to be gained by increasing these parameters, and increasing O/F leads to thermal issues. Increasing chamber pressure is possible but does add risk for marginal benefit in this situation.

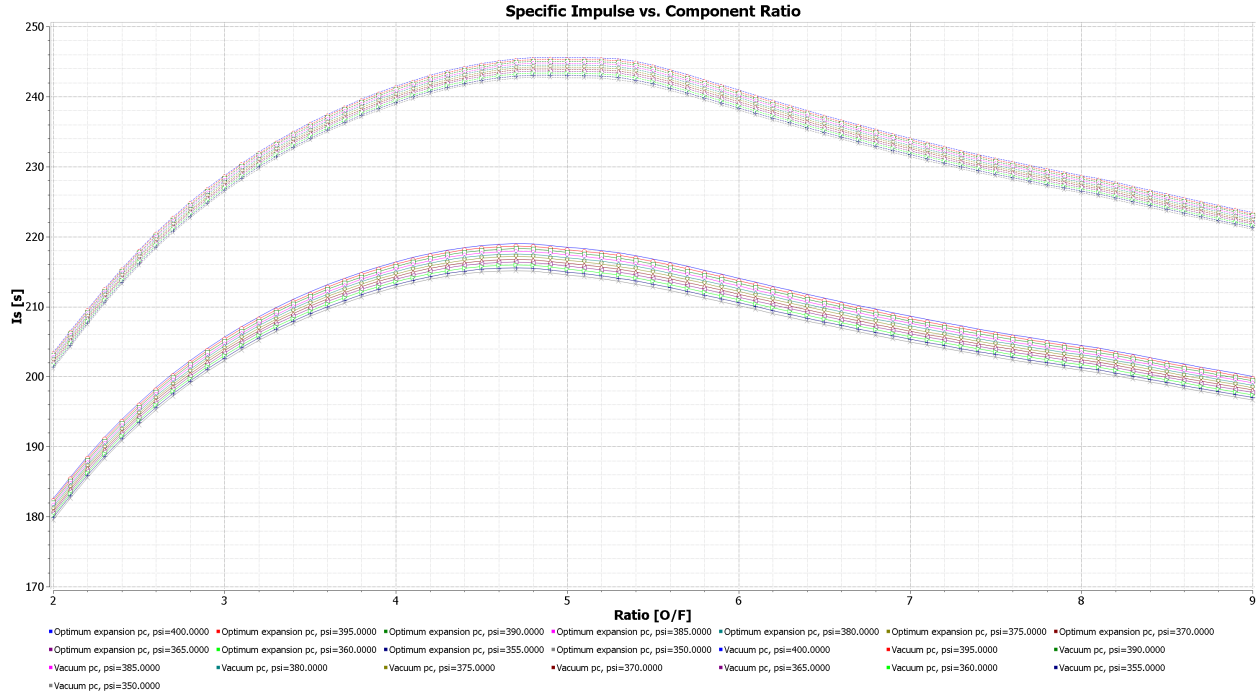


Figure 12: ISP vs OF ratio

## 6.2 Chamber Sizing

To size the chamber

Fig. 4-8 Frequently used geometrical shapes for combustion chambers.

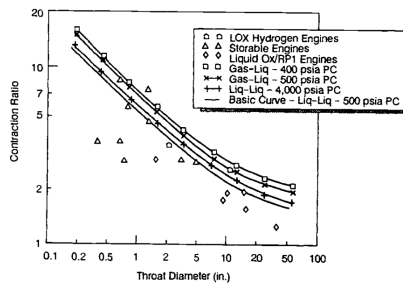


Fig. 4-9 Contraction ratio relationships used in scaling program.

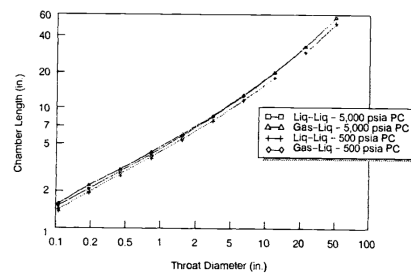


Fig. 4-10 Chamber length relationships used in scaling program.

Figure 13: Characteristic Sizes

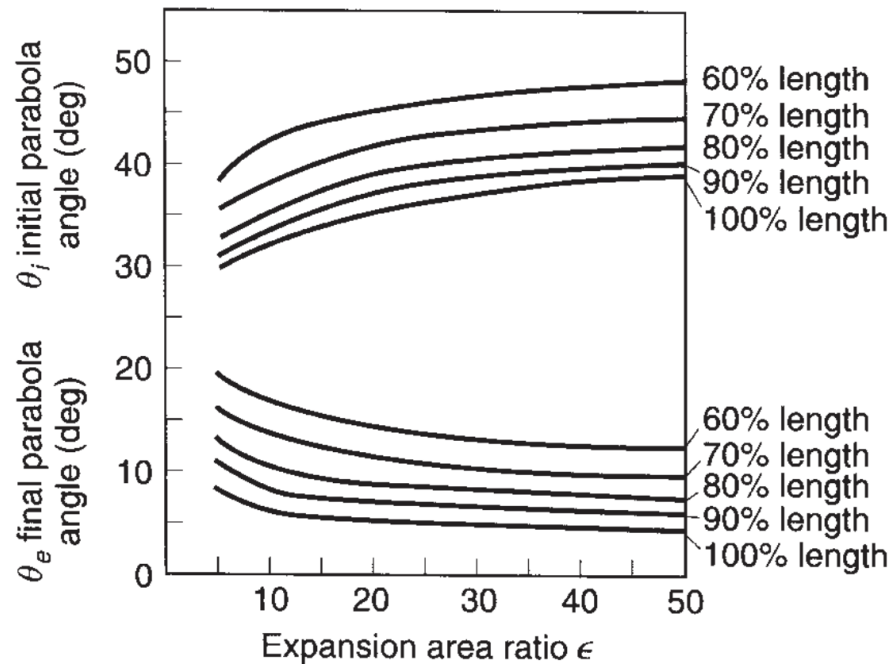


Figure 14: Bell Nozzle Parabola Angles

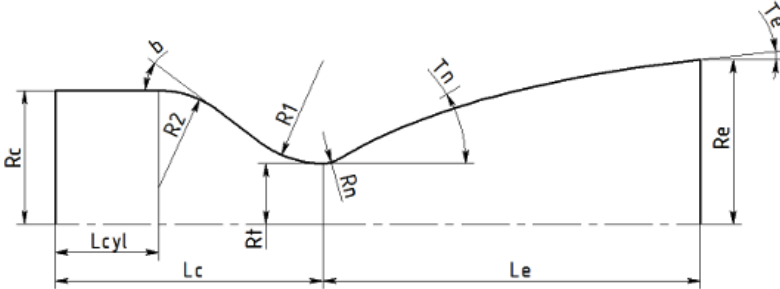
1. Use the relationship between throat diameter and contraction ratio to determine the contraction ratio based on the most relevant curve which happens to be the liq-liq curve at 500 psia (left graph).
2. Again map the throat diameter to find the corresponding characteristic chamber length ( $L^*$ ) within the 250mm limitation of the 3D printer bed.

Using RPA, the following parameters were inputted:

- Chamber pressure: 350 psi
- Desired thrust: 1250lbf
- Fuel mixture: 80:20 Ethanol to water ratio
- Oxidizer: N2O

## 7 Engine Parameters

### 7.1 Combustion Chamber Geometry



Combustion chamber size		Nozzle size	
		Type	
$D_c$	102.82 mm	$R_n$	Parabolic nozzle 8.78 mm
$D_t$	45.98 mm	$T_n$	21.00 deg
$L_{cyl}$	69.02 mm	$T_e$	14.00 deg
$L_c$	152.23 mm	$D_e$	92.15 mm
$L^*$	600.00 mm	$L_e$	69.84 mm
$R_1$	34.49 mm	$L_e/D_t$	1.52
$R_2$	92.37 mm	$L_e/L_{cyl}$	80.00 %
$b$	30.00 deg	$A_e/A_t$	4.02
$A_c/A_t$	5.00		

Parameter	Engine	Chamber
Thrust	sea level	5.3906 kN
	opt exp	5.3906 kN
	vacuum	6.2353 kN
Specific impulse	sea level	1654.8696 N·s/kg
	opt exp	1654.8696 N·s/kg
	vacuum	1914.1616 N·s/kg
Mass flow rate	total	3.2574 kg/s
	oxidizer	2.5788 kg/s
	fuel	0.6786 kg/s
Number of chambers	1	

Figure 15: Chamber Parameters

Parameter	Symbol	Value
Combustion chamber diameter	$D_c$	102.82 mm
Throat diameter	$D_t$	45.98 mm
Cylindrical section length	$L_{\text{cyl}}$	69.02 mm
Combustion chamber length	$L_c$	152.23 mm
Characteristic length	$L^*$	600 mm
Radius of curvature at inlet	$R_1$	34.49 mm
Radius of curvature at outlet	$R_2$	92.37 mm
Convergence half-angle	$b$	30°
Area contraction ratio	$A_c/A_t$	5.00

Table 3: Combustion Chamber Geometry

Parameter	Symbol	Value
Nozzle type	–	Parabolic nozzle
Nozzle radius of curvature	$R_n$	8.78 mm
Throat angle	$T_n$	21.00°
Exit angle	$T_e$	14.00°
Exit diameter	$D_e$	92.15 mm
Nozzle length	$L_e$	69.84 mm
Exit-to-throat area ratio	$A_e/A_t$	4.02

Table 4: Nozzle Geometry

## 7.2 Performance Parameters

Parameter	Condition	Value
Thrust	Sea level	5.3906 kN
Thrust	Vacuum	6.2353 kN
Specific impulse	Sea level	168.6 s
Specific impulse	Vacuum	195.1 s
Mass flow rate	Total	$3.2574 \text{ kg s}^{-1}$
Mass flow rate	Oxidizer	$2.5788 \text{ kg s}^{-1}$
Mass flow rate	Fuel	$0.6786 \text{ kg s}^{-1}$
Number of combustion chambers	–	1

Table 5: Performance Parameters

## 8 Thermal Analysis

The thermal analysis is likely the most difficult part of designing a rocket engine. Staying below a maximum wall temperature of 500k for the aluminum engine took many iterations. RPA solves the heat transfer equations based on the input parameters of film cooling and

regenerative cooling channels. Levlev and Bartz combined heat transfer calculations were implemented in RPA. Initially, the wall temperature was too high, so water was added to the fuel up to 20 percent, which increased regenerative cooling mass flow rate and also slightly lowered combustion temperatures. Aluminum ended up being the optimal material based on yield strength at wall temperature, and based on widespread availability. Copper offered some marginal benefits which could possibly have been optimized further but the fact that it is less available to 3D print is a large disadvantage.

Inconel 718 was initially selected due to its exceptional high-temperature strength, corrosion resistance, and widespread use in aerospace applications. However, several challenges emerged during the design process, ultimately leading to the exclusion of Inconel in favor of aluminum.

The first thermal analysis used 100% ethanol as the fuel, relying solely on regenerative cooling. Due to Inconel's low thermal conductivity of approximately  $11.4 \text{ W m}^{-1} \text{ K}^{-1}$ , the heat transfer from the chamber walls to the coolant was insufficient. This resulted in excessively high wall temperatures, exceeding 1000 K.

To mitigate this, film cooling was added by introducing ethanol along the chamber walls through dedicated orifices, however it required significantly more film cooling mass flux than aluminum.

Inconel's thermal properties required ultra-thin chamber walls to facilitate regenerative cooling effectively. This posed significant manufacturing challenges because printing Inconel with thin walls is prone to defects such as warping and cracking due to the high residual stresses induced during metal 3D printing. Additionally, Inconel's extreme hardness and tendency to destroy tools would make post-processing and machining time-consuming and expensive, reducing its feasibility.

After considering thermal analysis and manufacturability constraints Inconel was ultimately replaced with aluminum AlSi10Mg, which offered better thermal conductivity ( $150 \text{ W m}^{-1} \text{ K}^{-1}$ ) and was more optimal for regenerative cooling. Its lower melting point was offset by optimized film and regenerative cooling designs, allowing for operation while staying below the 500 K maximum wall temperature. While copper provided slightly better thermal performance, its limited availability for 3D printing made aluminum the most practical and effective material choice.

Parameter	Value
Maximum heat flux at the throat	$246.80 \text{ kW m}^{-2}$
Maximum wall temperature (gas side)	467.98 K
Maximum wall temperature (coolant side)	452.74 K
Maximum coolant temperature	353.00 K
Average coolant velocity	$6.16 \text{ m s}^{-1}$
Average coolant density	$800.92 \text{ kg m}^{-3}$

Table 6: Aluminum Engine Thermal Analysis

## 8.1 Material Specifications

Property	AlSi10Mg (EOS)	Inconel 718 (EOS)	CuZnZn (EOS)
Material Type	Aluminum Alloy	Nickel Alloy	Copper Alloy
Yield Strength at 250°C	125 MPa	1030 MPa	150 MPa
Ultimate Tensile Strength	230 MPa	1240 MPa	315 MPa
Density	2700 kg/m <sup>3</sup>	8190 kg/m <sup>3</sup>	8500 kg/m <sup>3</sup>
Thermal Conductivity at 250°C	150 W m <sup>-1</sup> K <sup>-1</sup>	11.4 W m <sup>-1</sup> K <sup>-1</sup>	320 W m <sup>-1</sup> K <sup>-1</sup>
Melting Point	570 °C	1350 °C	1083 °C

Table 7: Material Specifications for EOS 3D-Printed Alloys

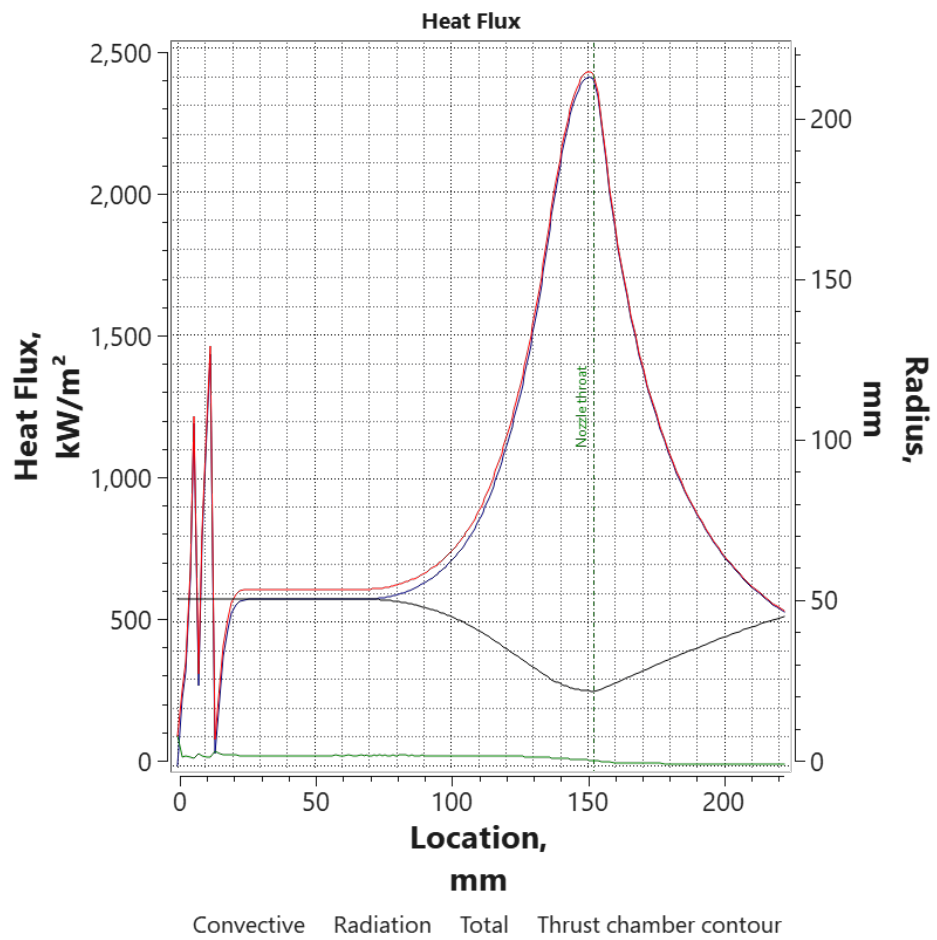


Figure 16: Aluminum Engine Heat Flux along Profile

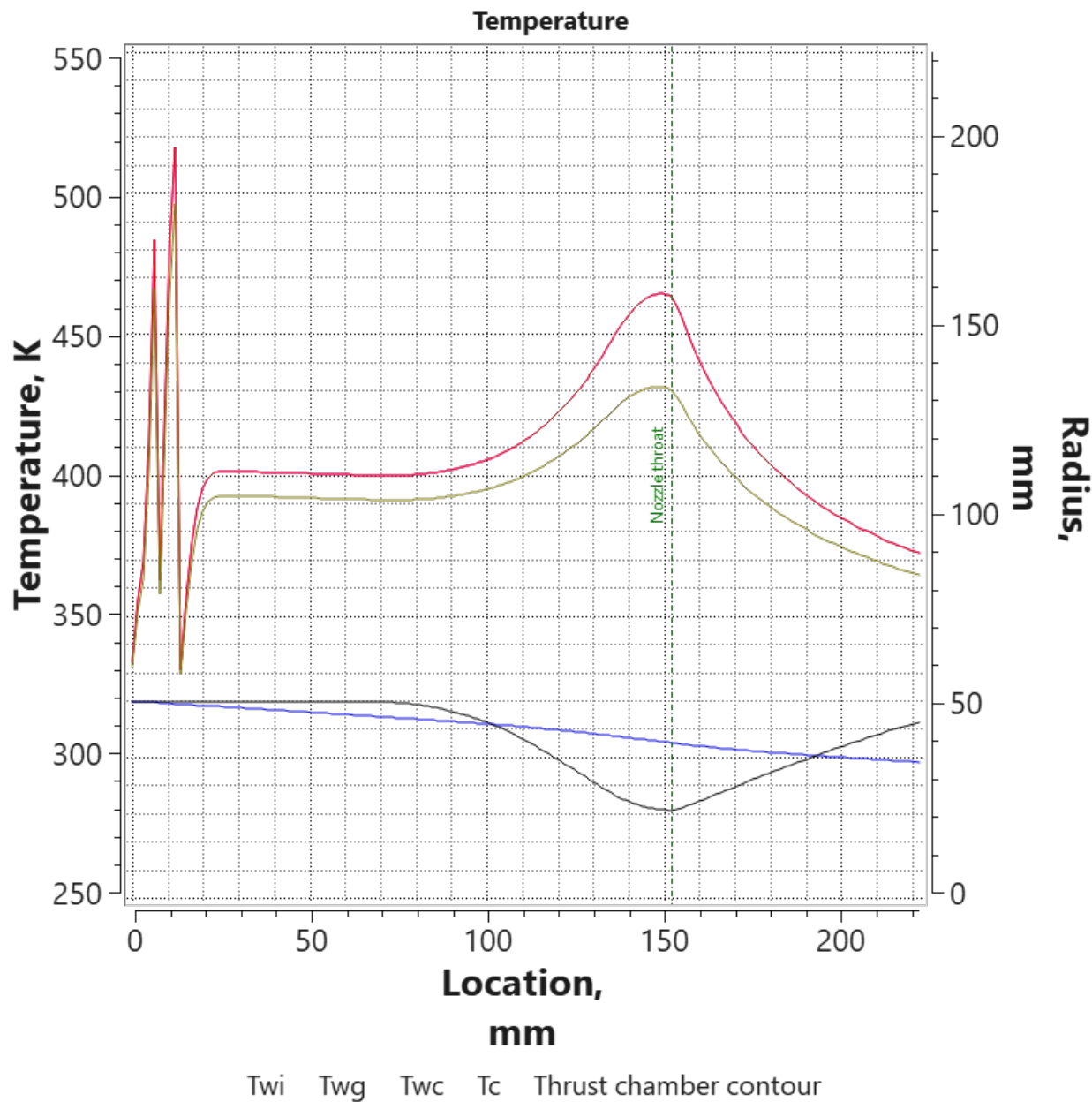


Figure 17: Aluminum Engine Temperature Profile under Nominal Operation

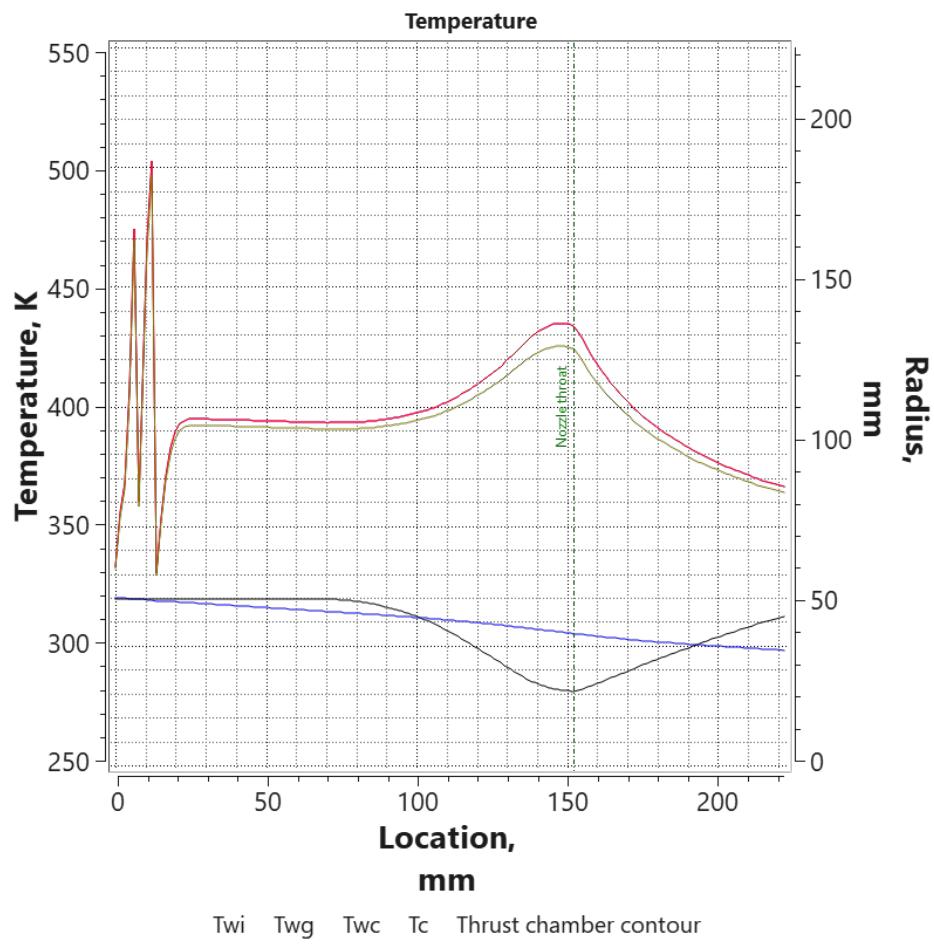


Figure 18: Copper Engine Temperature Profile under Nominal Operation

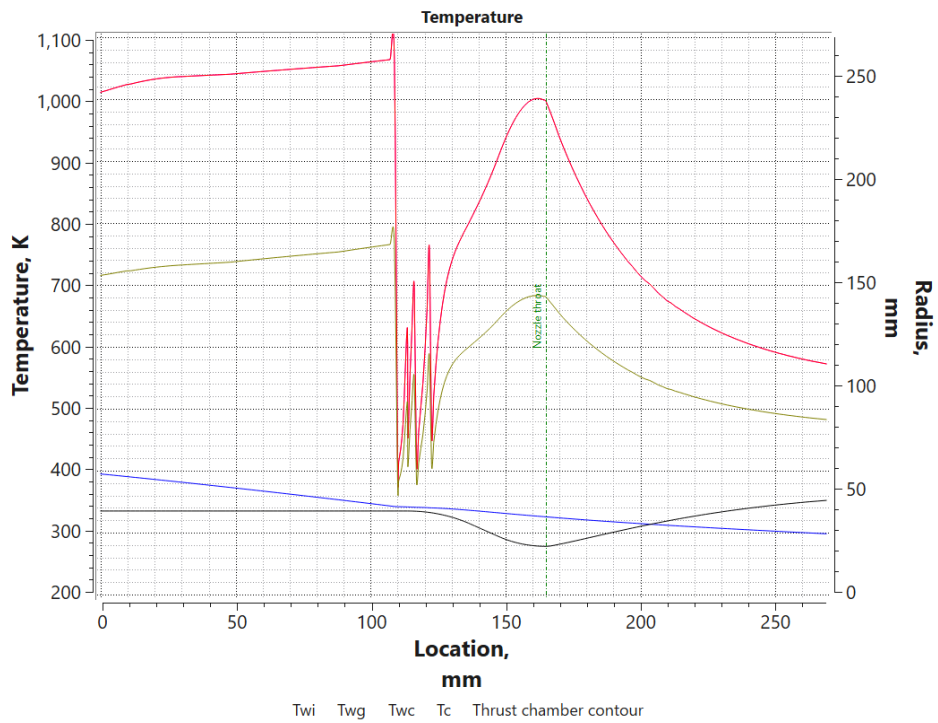


Figure 19: Engine Temperature Profile under Nominal Operation

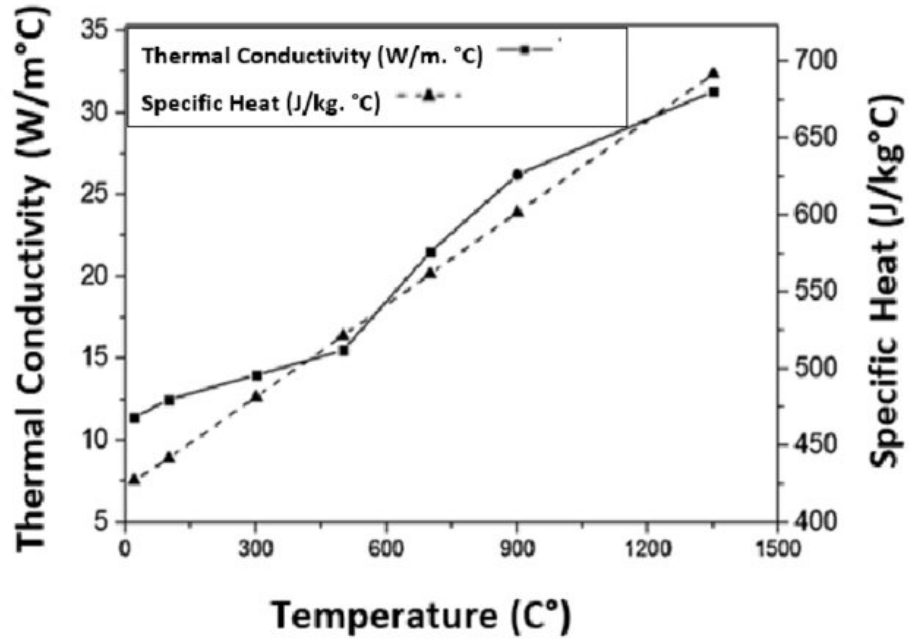


Figure 20: Inconel Thermal Conductivity vs Temperature

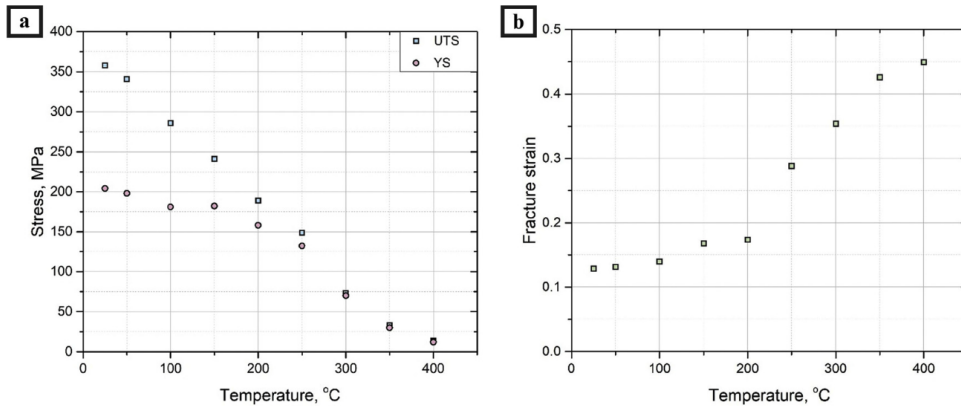


Fig. 3. Temperature-dependence of the yield and ultimate stresses (a), and strain at fracture (b).

Figure 21: AlSi10Mg Strength vs Temperature

## 9 Cooling Channel Design

### 9.1 Input Parameters

- Chamber Mass Flux:

$$\dot{m}_{\text{chamber}} = 3.2574 \text{ kg s}^{-1} \quad (\text{from RPA})$$

- Cooling Fraction:

$$f_{\text{cool}} = 0.053$$

- Fuel Injector Mass Flow Rate:

$$\dot{m}_{\text{fuel, injector}} = 0.6786 \text{ kg s}^{-1}$$

The total fuel mass flow rate is:

$$\dot{m}_{\text{cool}} = f_{\text{cool}} \cdot \dot{m}_{\text{chamber}} = 0.053 \times 3.2574 = 0.1726 \text{ kg s}^{-1}$$

$$\dot{m}_{\text{total}} = \dot{m}_{\text{fuel, injector}} + \dot{m}_{\text{cool}} = 0.6786 + 0.1726 = 0.8512 \text{ kg s}^{-1}$$

The percentage of fuel used for regenerative cooling is:

$$\text{Percent for Regenerative Cooling} = \frac{\dot{m}_{\text{total}}}{\dot{m}_{\text{chamber}}} = \frac{0.8512}{3.2574} = 0.2612 \text{ or } 26.1\%$$

## 10 Cooling Channel Geometry

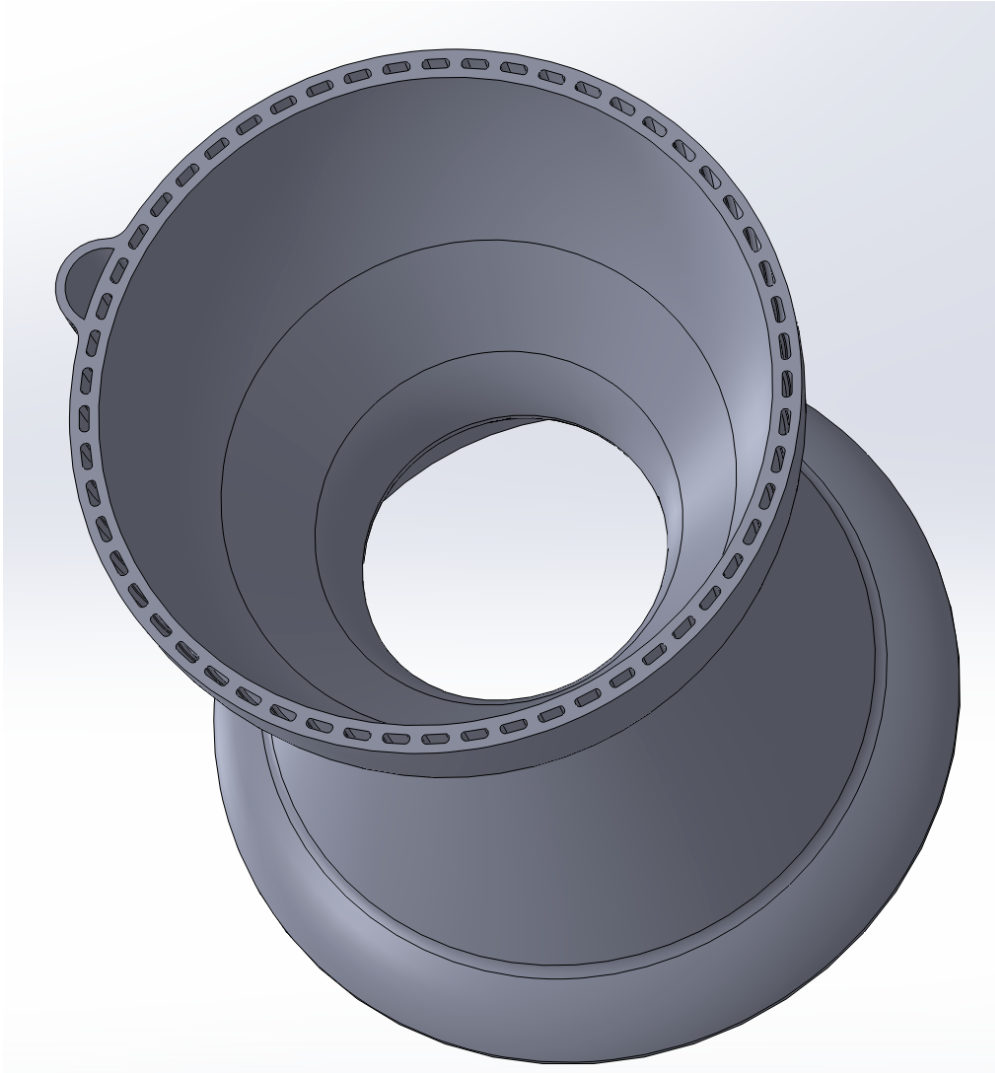


Figure 22: Cross-sectional view of the cooling channels. Highlights the thermal management design for heat dissipation during combustion.

Optimal Cooling Channel Geometry was determined by RPA based on a 1.5mm wall thickness.

- **Channel Length:**

$$L = 0.25 \text{ m}$$

- **Number of Channels:**

$$N = 58$$

- **Cross-sectional Area (from CAD):**

$$A_{\text{channel}} = 2.66291 \times 10^{-6} \text{ m}^2$$

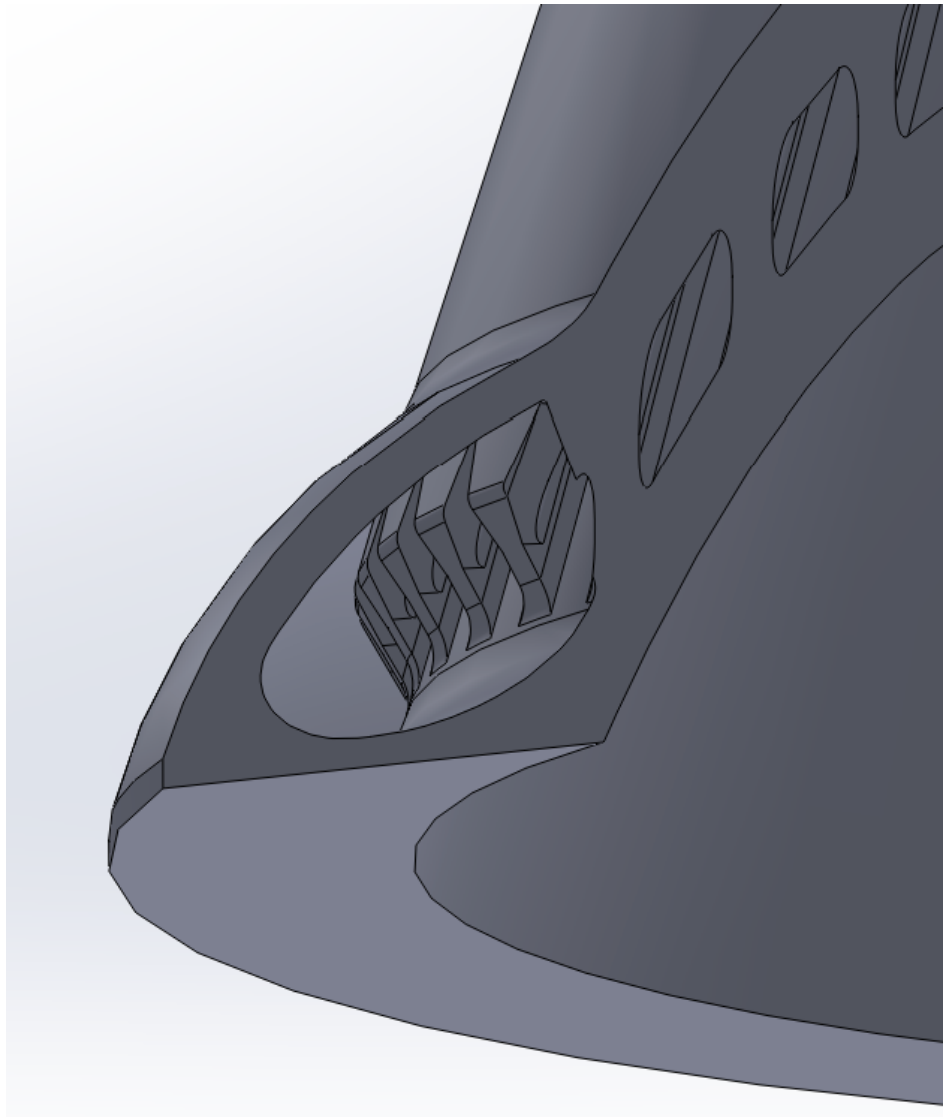


Figure 23: Nozzle Coolant Distribution Manifold

- **Perimeter (from CAD):**

$$P = 5.938 \times 10^{-3} \text{ m}$$

*Note:* The perimeter was calculated by taking the cross-section of the cooling channels at the smallest area, located around the throat. This design was intentional because thinner channels at the throat increase flow velocity, which enhances heat transfer from the walls to the fluid.

The hydraulic diameter is:

$$D_h = \frac{4A_{\text{channel}}}{P} = \frac{4 \times 2.66291 \times 10^{-6}}{5.938 \times 10^{-3}} = 1.794 \times 10^{-3} \text{ m}$$

## 10.1 Regen Channel Flow Calculations

The volumetric flow rate per channel is:

$$Q = \frac{\dot{m}_{\text{total}}}{\rho N} = \frac{0.8512}{780 \times 58} = 1.904 \times 10^{-5} \text{ m}^3/\text{s}$$

The flow velocity is:

$$v = \frac{Q}{A_{\text{channel}}} = \frac{1.904 \times 10^{-5}}{2.66291 \times 10^{-6}} = 7.07 \text{ m s}^{-1}$$

The Reynolds number is:

$$Re = \frac{\rho v D_h}{\mu} = \frac{780 \times 7.07 \times 1.794 \times 10^{-3}}{0.001095} = 9028.82$$

### 10.1.1 Friction Factor Calculation

The friction factor depends on the flow regime:

- **Laminar Flow ( $Re < 2300$ ):**

$$f = \frac{64}{Re}$$

- **Transitional Flow ( $2300 \leq Re < 4000$ ):**

Using the Blasius approximation:

$$f = 0.079 \cdot Re^{-0.25}$$

- **Turbulent Flow ( $Re \geq 4000$ ):**

Using the Colebrook-White equation:

$$\frac{1}{\sqrt{f}} = -2 \log_{10} \left( \frac{\epsilon}{3.7D_h} + \frac{2.51}{Re \sqrt{f}} \right)$$

Given the calculated Reynolds number  $Re = 9028.82$ , the flow is turbulent. Solving the Colebrook-White equation numerically yields:

$$f = 0.0629$$

### 10.1.2 Pressure Drop using Darcy-Weisbach Equation

The Darcy-Weisbach equation is:

$$\Delta P = f \cdot \frac{L}{D_h} \cdot \frac{\rho v^2}{2}$$

Substituting the known values:

$$\Delta P = 0.0629 \cdot \frac{0.25}{1.794 \times 10^{-3}} \cdot \frac{780 \cdot 7.07^2}{2}$$

Simplifying:

$$\Delta P = 1.707 \times 10^5 \text{ Pa}$$

Converting to PSI:

$$\Delta P_{\text{PSI}} = \frac{\Delta P}{6894.76} = 24.76 \text{ psi}$$

### 10.1.3 Regen Channel Flow Results Summary

- **Total Fuel Mass Flow Rate:**  $\dot{m}_{\text{total}} = 0.85 \text{ kg s}^{-1}$
- **Reynolds Number:**  $Re = 9028.82$  (Turbulent)
- **Flow Velocity:**  $v = 7.07 \text{ m s}^{-1}$
- **Friction Factor:**  $f = 0.0629$
- **Pressure Loss:**  $\Delta P = 1.707 \times 10^5 \text{ Pa}$
- **Pressure Loss in PSI:**  $\Delta P_{\text{PSI}} = 24.76 \text{ psi}$

## 10.2 Structural Analysis of Cooling Channels

Parameter	Symbol	Value
Chamber Pressure	$P_c$	$350 \text{ psi} = 2.413 \times 10^6 \text{ Pa}$
Fuel Maximum Expected Operating Pressure (MEOP)	$P_f$	$1000 \text{ psi} = 6.895 \times 10^6 \text{ Pa}$
Minimum Wall Thickness	$t$	$0.0015 \text{ m}$
Cooling Channel Inner Radius	$r_i$	$0.046 \text{ m}$
Cooling Channel Width	$r_{\text{cooling}}$	$0.0015 \text{ m}$
Material Allowable Yield Strength at 250°C (AlSi10Mg)	$\sigma_{\text{allow}}$	$125 \times 10^6 \text{ Pa}$
Safety Factor	$SF$	1.5

Table 8: Design Parameters for Structural and Thermal Calculations

### 10.2.1 Cooling Channel Hoop Stress

The hoop stress in the cooling channel wall is calculated using the thin-walled pressure vessel approximation:

$$\sigma_{\text{cool}} = \frac{P_c \cdot SF \cdot r_{\text{cooling}}}{t}$$

Substituting values:

$$\sigma_{\text{cool}} = \frac{2.413 \times 10^6 \times 1.5 \times 0.0015}{0.0015} = 3.62 \times 10^6 \text{ Pa} = 3.62 \text{ MPa}$$

### 10.2.2 Outer Wall Stress

The outer wall stress is calculated as:

$$\sigma_{\text{main}} = \frac{P_f \cdot SF \cdot r_i}{t}$$

Substituting values:

$$\sigma_{\text{main}} = \frac{6.895 \times 10^6 \times 1.5 \times 0.046}{0.0015} = 1.1101 \times 10^8 \text{ Pa} = 111.01 \text{ MPa}$$

Margin of Safety

The margin of safety is given by:

$$\text{Margin} = \frac{\sigma_{\text{allow}}}{\sigma_{\text{main}}} - 1$$

Substituting values:

$$\text{Margin} = \frac{125 \times 10^6}{1.1101 \times 10^8} - 1 = 0.126 = 12.60\%$$

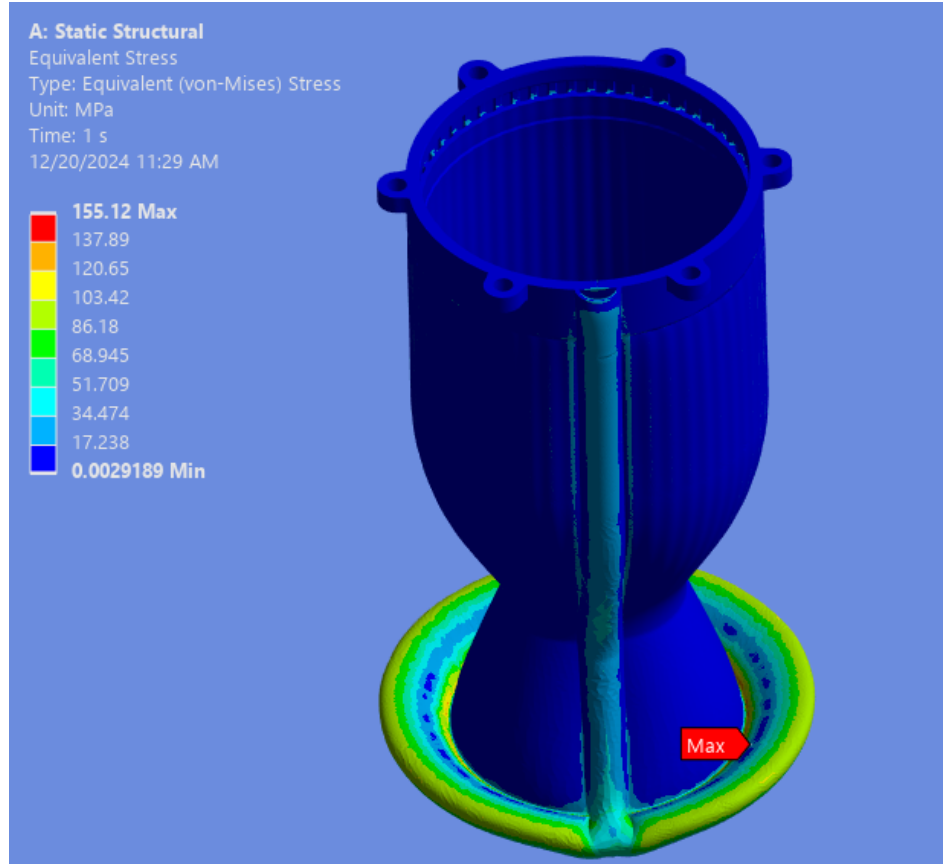


Figure 24: FEA Analysis

### 10.2.3 Cooling Channel Structural Results

- **Cooling Channel Stress:**  $\sigma_{\text{cool}} = 3.62 \text{ MPa}$
- **Outer Wall Stress:**  $\sigma_{\text{main}} = 111.01 \text{ MPa}$
- **Material Allowable Stress:**  $\sigma_{\text{allow}} = 125 \text{ MPa}$
- **Margin of Safety:** Margin = 12.60%

FEA results show a higher peak stress, but this is at a nonphysical mesh location.

# 11 Ethanol Pintle Flow Calculations

Parameter	Symbol	Value
Discharge Coefficient (From ICL Technical Report)	$C_d$	0.82
Ethanol Density	$\rho$	$780 \text{ kg/m}^3$
Orifice Inner Diameter (Given)	$d_{\text{inner}}$	0.74525 inches = 0.01893 m
Desired Mass Flow Rate	$\dot{m}_{\text{desired}}$	$0.68 \text{ kg s}^{-1}$
Upstream Pressure	$P_1$	700 psi = $4.826 \times 10^6 \text{ Pa}$
Downstream Pressure	$P_2$	350 psi = $2.413 \times 10^6 \text{ Pa}$
Pressure Drop	$\Delta P$	350 psi = $2.413 \times 10^6 \text{ Pa}$

Table 9: Pintle Fuel Flow Rate Design Parameters

## 11.1 Pintle Gap Calculation

The outer diameter of the annular orifice is determined by:

$$d_{\text{outer}} = d_{\text{inner}} + 2 \cdot g$$

Where:

- $d_{\text{outer}}$ : Outer diameter of the annular gap (m)
- $d_{\text{inner}}$ : Inner diameter of the orifice (m)
- $g$ : Pintle gap (m)

The annular flow area is calculated as:

$$A = \frac{\pi}{4} (d_{\text{outer}}^2 - d_{\text{inner}}^2)$$

The volumetric flow rate is:

$$Q = C_d \cdot A \cdot \sqrt{\frac{2\Delta P}{\rho}}$$

The corresponding mass flow rate is:

$$\dot{m} = \rho Q = \rho \cdot C_d \cdot A \cdot \sqrt{\frac{2\Delta P}{\rho}}$$

Solving this equation for the pintle gap  $g$ , the MATLAB numerical solution yields:

$$g = 0.000223 \text{ m} = 0.008793 \text{ inches}$$

## 11.2 Pintle Gap Results

- **Desired Mass Flow Rate:**  $\dot{m}_{\text{desired}} = 0.68 \text{ kg s}^{-1}$
- **Pressure Drop:**  $\Delta P = 350 \text{ psi}$
- **Orifice Inner Diameter:**  $d_{\text{inner}} = 0.74525 \text{ inches}$
- **Calculated Pintle Gap:**

$$g = 0.000223 \text{ m} = 0.008793 \text{ inches}$$

## 12 Throttle Level Thermal Profiles

Throttling significantly decreases the regen flow rates, but does not decrease combustion temperature. This poses a significant challenge as the engine would otherwise melt at low throttle levels. If fuel and oxidizer can be throttled independently, the OF ratio can be programmed to shift more fuel rich when a low throttle maneuver is commanded. This will decrease combustion temperature as well as maintain nominal regenerative cooling flow. The film cooling can also be independent of throttle level if the engine is throttled by moving the pintle components directly rather than throttling upstream of the engine by closing valves. For precision landing scenarios like the Lunar Lander Challenge, where the engine may need to operate at as low as 12% to achieve a thrust-to-weight (T/W) ratio of 1 for a 150-lb vehicle, running fuel-rich under these conditions ensures sustained cooling and prevents thermal failure.

### 12.1 Thermal Profiles by Throttle Level

The following figures present the thermal profiles of the engine at various throttle levels, highlighting the impact of reduced propellant flow on chamber wall temperatures. Each simulation assumes a 1.5 mm chamber wall thickness and an aluminum construction, and a 600 mm characteristic length ( $L^*$ ) with 58 regenerative cooling channels.

### 12.1.1 Low Throttle Operation

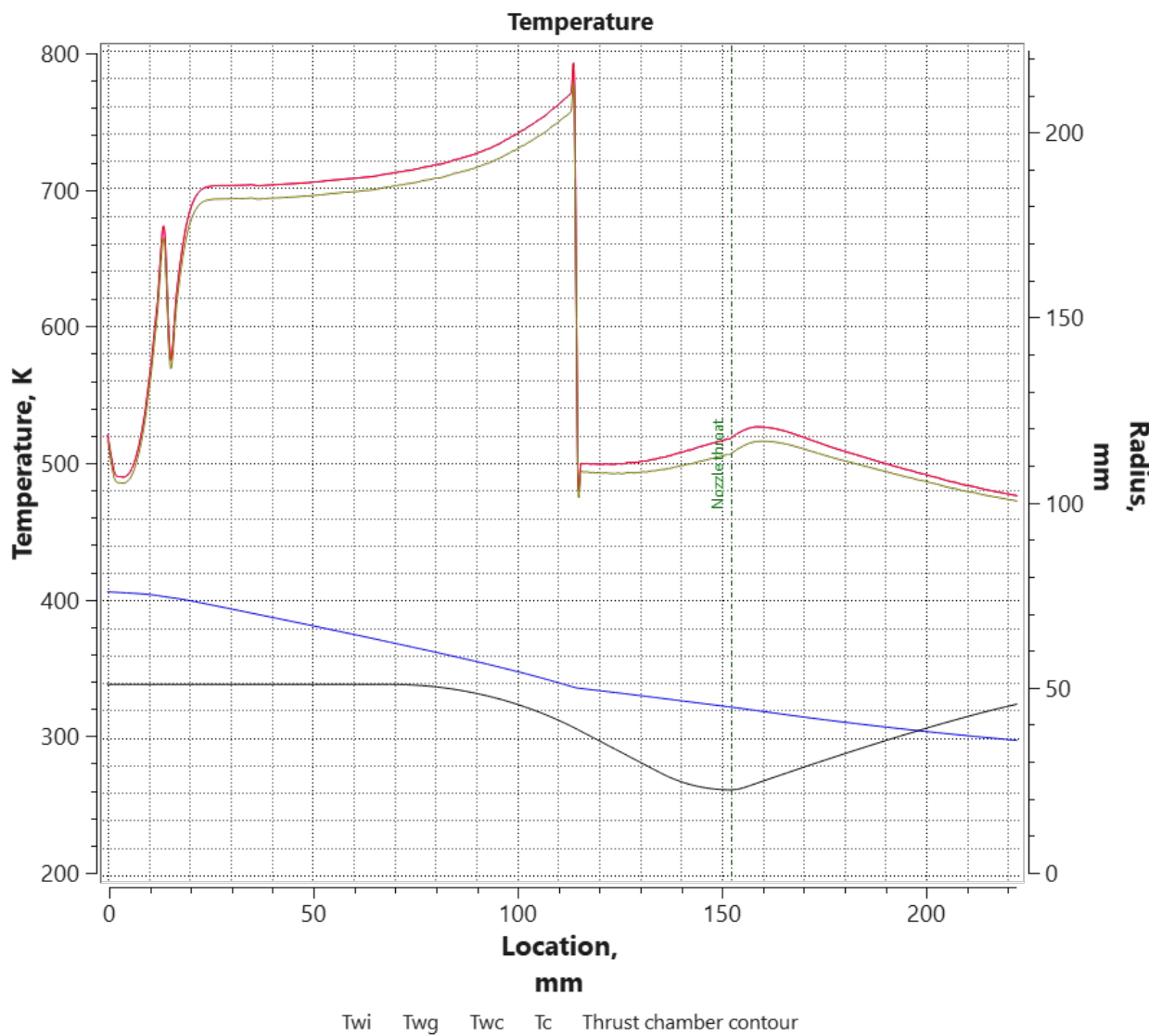


Figure 25: Thermal Profile at 12% Throttle

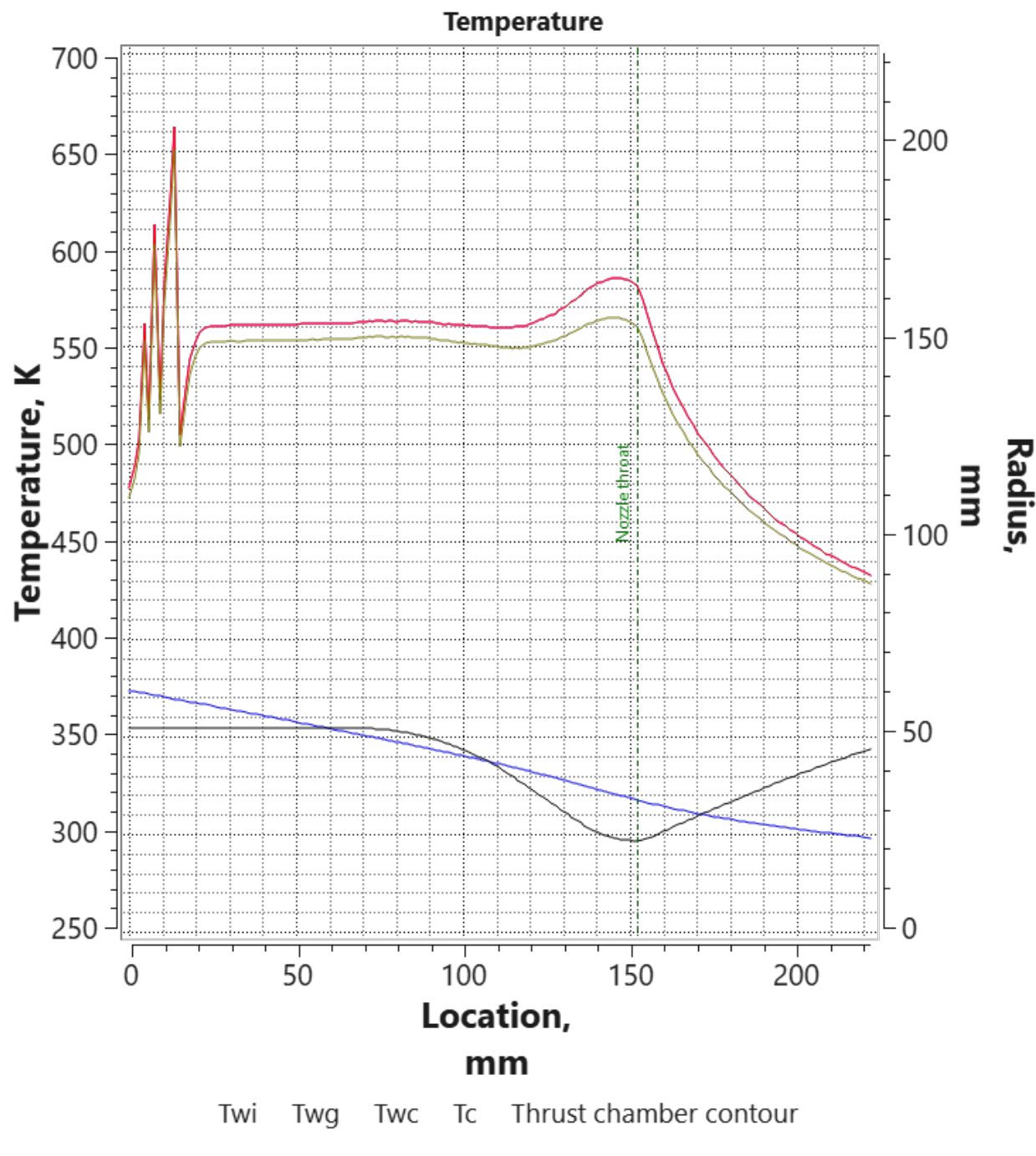


Figure 26: Thermal Profile at 20% Throttle

### 12.1.2 Mid-Level Throttle Operation

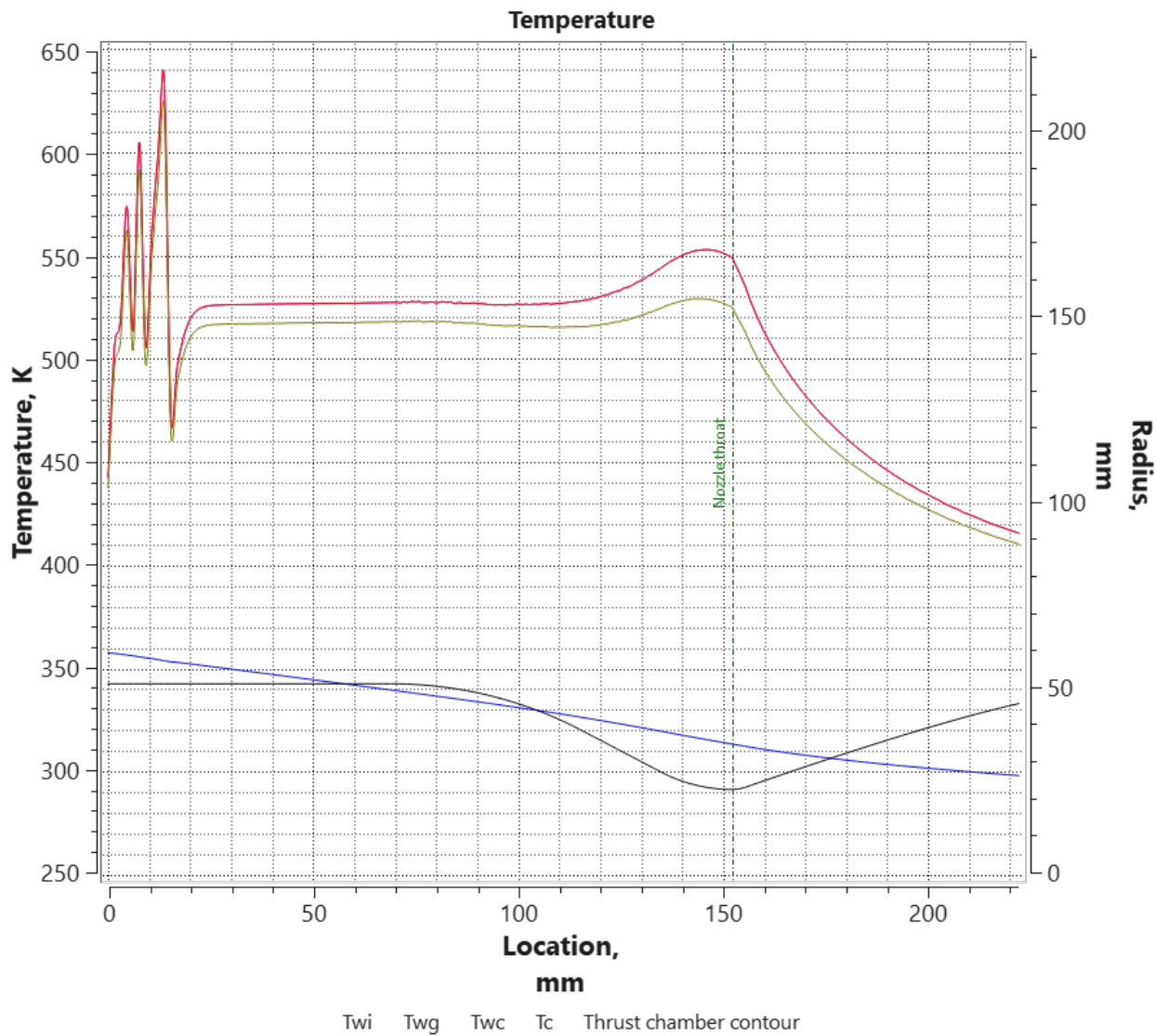


Figure 27: Thermal Profile at 30% Throttle

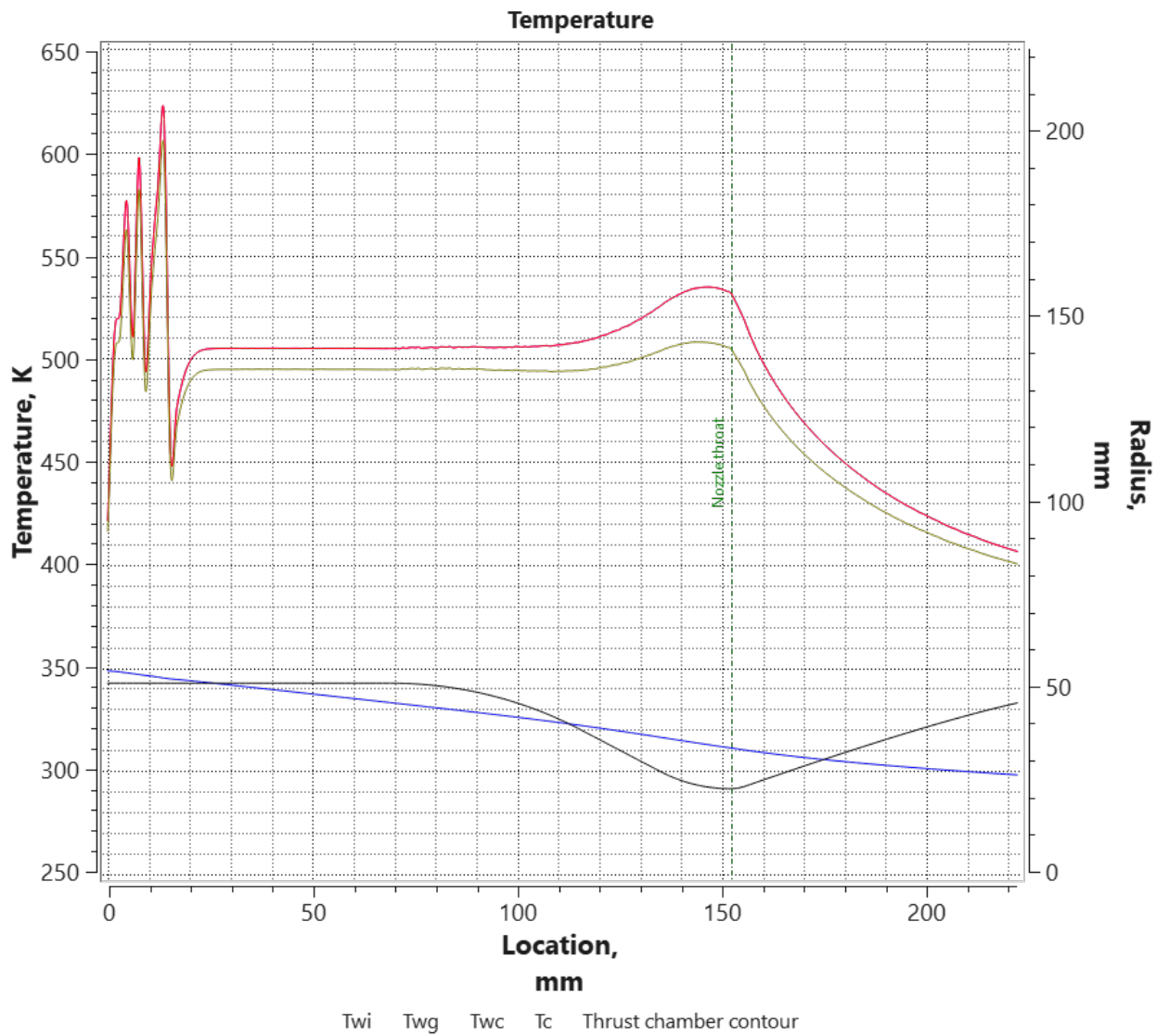


Figure 28: Thermal Profile at 40% Throttle

### 12.1.3 High Throttle Operation

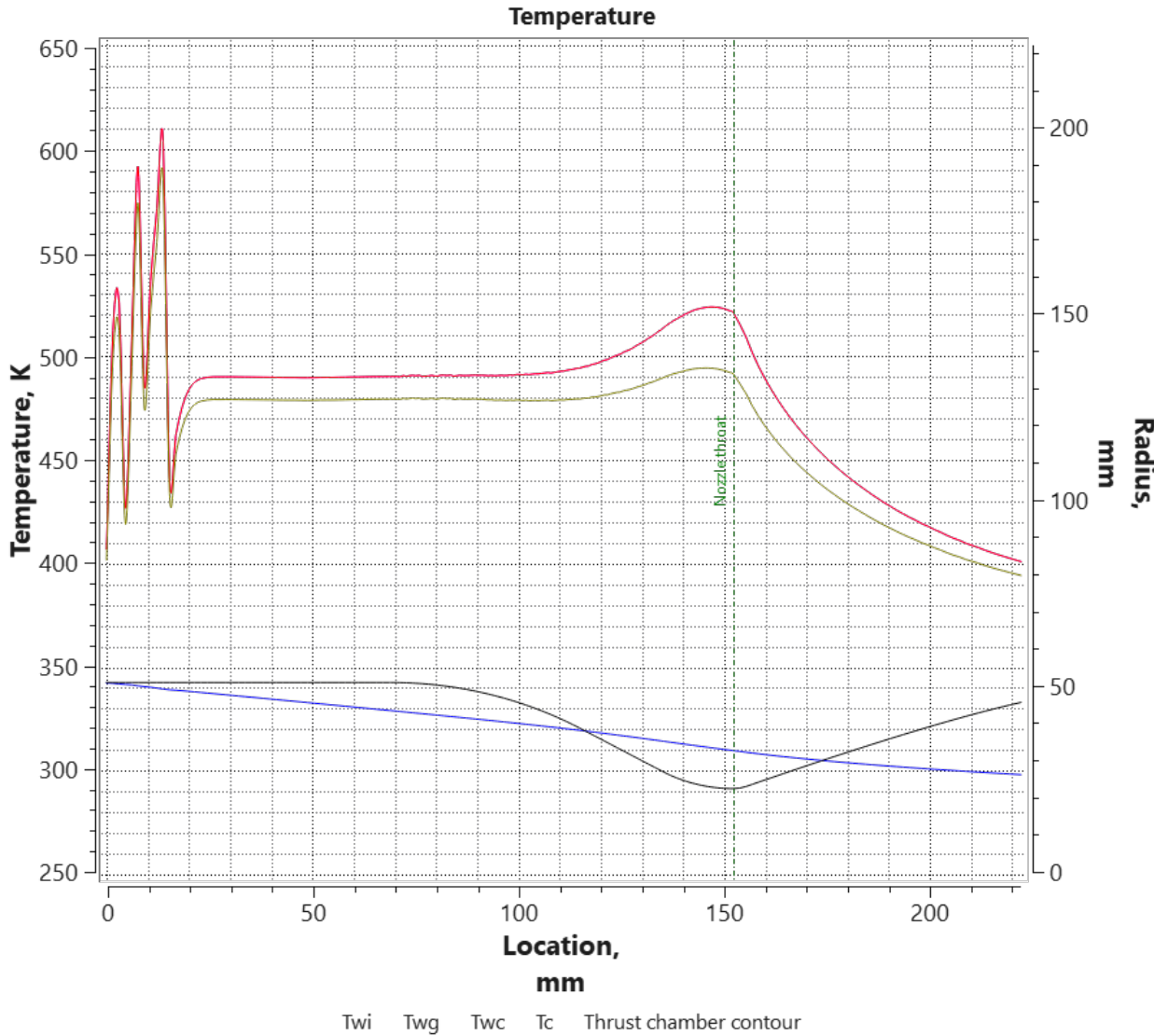


Figure 29: Thermal Profile at 50% Throttle

## 13 MENG Updates

## 14 Design Modifications and CAD Development

### 14.1 Fuel Inlet Modifications

The fuel inlet port was modified from the original design which was an -08 O-Boss to a -06 O-boss configuration to fit within the 6" inscribed circle constraint. This constraint exists so that the rocket engine can fit within CRT's standard airframes.

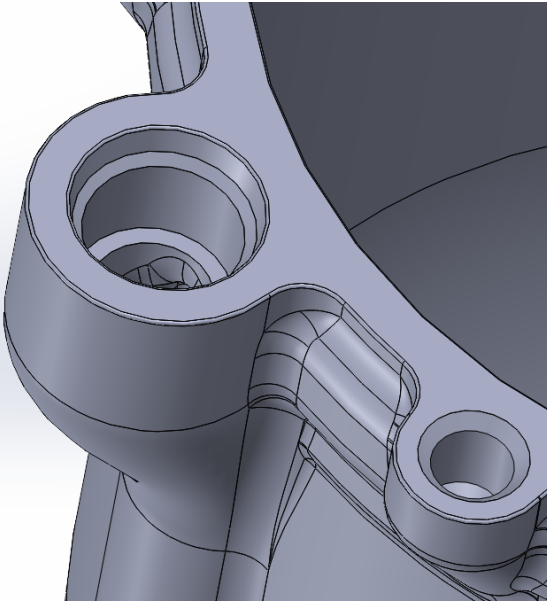


Figure 30: Fuel Inlet

## 14.2 Combustion Chamber Modifications

Additional improvements to the upper fuel channels included the addition of fillets and a reinforcement band around the injector interface. The original minimum wall thickness was approximately 1 mm, but analysis indicated a requirement of at least 3.3 mm to achieve a safety factor of 1.5. The final design increased this dimension to 4 mm (0.157") to provide additional margin.

### Manufacturing

The injector interface dimensions were modified to accommodate an O-ring (size 241). Dimensional tolerance requirements were specified by XMAKE at  $\pm 0.3\%$  with a minimum of 0.3 mm, meaning potential ID variation of 0.0125. To account for this variation and to achieve the correct dimensions post machining, the 3D printed model needed to be modified to add additional material around the bore. The design targets a diametral clearance of 3 thousandths of an inch (0.003") to ensure proper O-ring compression per ORD-5700. This model also has the bolt holes removed, as they will be post machined as well.

## 15 Structural Analysis

### 15.1 FEA Methodology

A comprehensive Finite Element Analysis (FEA) approach was implemented to verify the structural integrity of the engine design. The primary goal of these analyses was to verify that the combustion chamber will survive the thermal and pressure loads resulting from nominal operation of the engine. The combustion chamber, and the combustion chamber assembly were analyzed using ANSYS Static Structural simulations in three separate

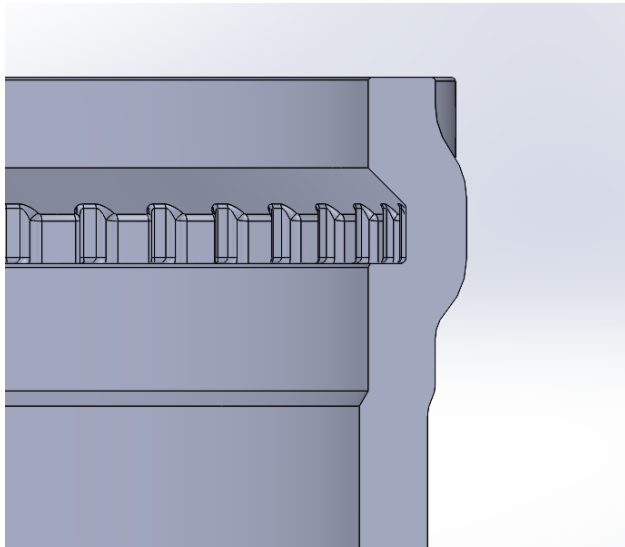


Figure 31: Reinforcement Band

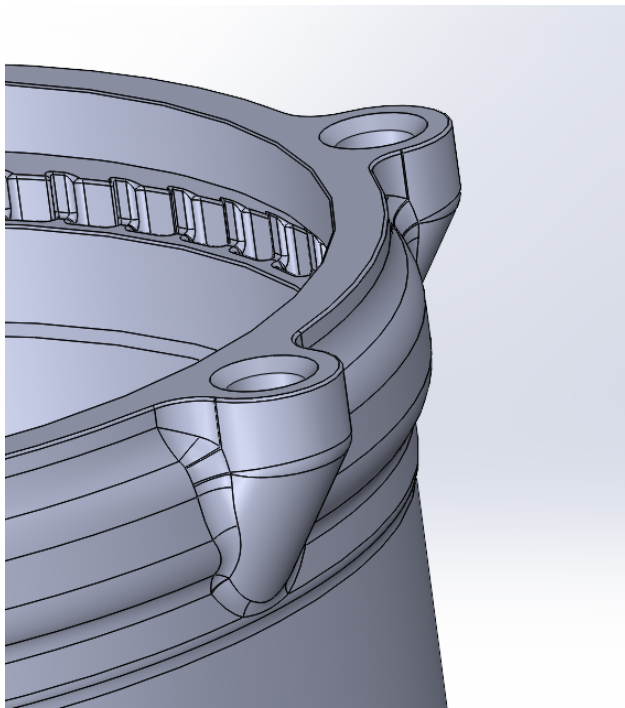


Figure 32: Fuel Channel Fillets and Reinforcement Band

models: Isolated Chamber, Combined Chamber and Injector, and sectioned Combined Chamber and Injector. Thermal and structural loads were considered independently, as well as concurrently. The engine was simulated to standard CRT factors of safety.

## 15.2 Isolated Chamber Analysis

Initial FEA runs on the isolated chamber revealed constraint-related issues causing high stresses in unrealistic locations as seen in As shown in Figure 34. The original ANSYS model for the chamber only consisted of the chamber body, and no other components. However, analyzing the chamber in this way was not accurate. The original model has the bolt holes fixed, but this lead to high stress areas as shown in the figure. To determine whether these stresses were realistic, the bottom was then fixed, and the top was left unconstrained. The stress in the injector interface decreased significantly as seen in Figure 34, however this is an under-conservative estimate, because the constraint on the bolt holes does induce stress in this area of the chamber. This stress is due to the pressure bowing out the areas between the bolts. The degree to which this effect occurs is controlled by the stiffness of the injector.

This prompted refinement of the boundary conditions and constraint methodologies to better represent the actual operating environment. To accurately model this area, the injector was added to the model, along with the bolts.

## 15.3 Boundary Conditions

The following boundary conditions are shared between the breakout sectioned model and the whole combined model, with the exception of the frictionless support added to the breakout sectioned model. This frictionless contact between the bore of the chamber and the injector OD prevents the injector from deflecting through the chamber walls. The bore and injector will be lubricated, and should slide against each-other if they contact. Therefore, frictionless is an appropriate contact scheme. The contact between the injector face to combustion chamber top is modeled as frictional, as these surfaces will be clamped together with no lubricant. The Bolt Threads are modeled as bonded to the combustion chamber threads. This is an appropriate contact to approximate the relationship between the male thread and the female thread.

The injector bolts are modeled as a frictionless contact with the injector through holes. These surfaces should not come into contact with each other unless the joint is slipping.

The bolt heads are modeled as frictional contacts with the top face of the injector. These surfaces will be clamped together by the preload on the bolt. The friction factor is modeled to be around 0.2, as expected with lubricated metal to metal surfaces. A more accurate friction factor can be found through online lookup tables. The injector is constrained with a fixed support on the central port. This is a reasonable constraint, as this part of the injector is already very stiff, so fixing this face will not significantly affect the stiffness of the rest of the model. The sliced breakout model has a frictionless support on the cut plane, which is used as a symmetry boundary condition. The model is not actually symmetric around the cut plane, but it is an accurate approximation when analyzing the top section of the combustion chamber.

## H: Copy of Copy of Copy of Static Structural

Equivalent Stress

Type: Equivalent (von-Mises) Stress

Unit: MPa

Time: 1 s

4/25/2025 4:26 PM

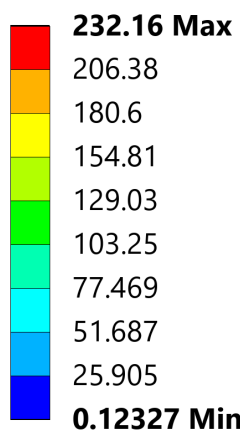


Figure 33: Fixed Bottom

### G: Copy of Copy of Static Structural

Equivalent Stress 2

Type: Equivalent (von-Mises) Stress

Unit: MPa

Time: 1 s

4/25/2025 8:13 PM

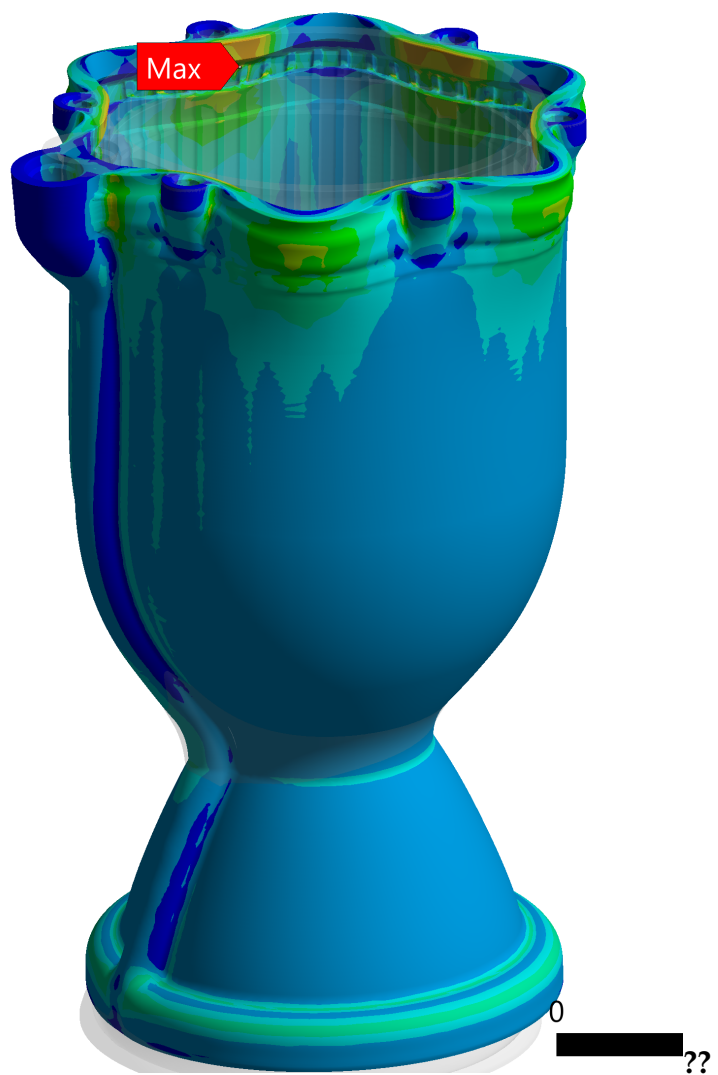
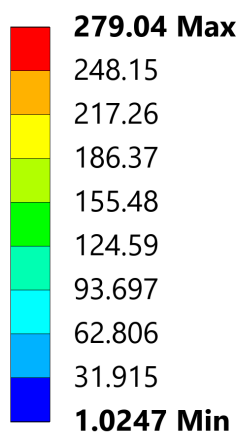


Figure 34: Fixed Bolt Constraint

**D: 1.5x MEOP Pressure Loading+Thermal (yield)**

Combined Yield 2

Time: 2. s

Items: 10 of 11 indicated

5/18/2025 12:10 AM

- A** Pressure: 10.342 MPa
- B** Pressure 2: 3.6197 MPa
- C** Pressure 3: 10.342 MPa
- D** Pressure 4: 3.6197 MPa
- E** Fixed Support
- F** hex bolt\_ai-1: Lock
- G** hex bolt\_ai-4: Lock
- H** hex bolt\_ai-2: Lock
- I** hex bolt\_ai-3: Lock
- J** hex bolt\_ai-5: Lock

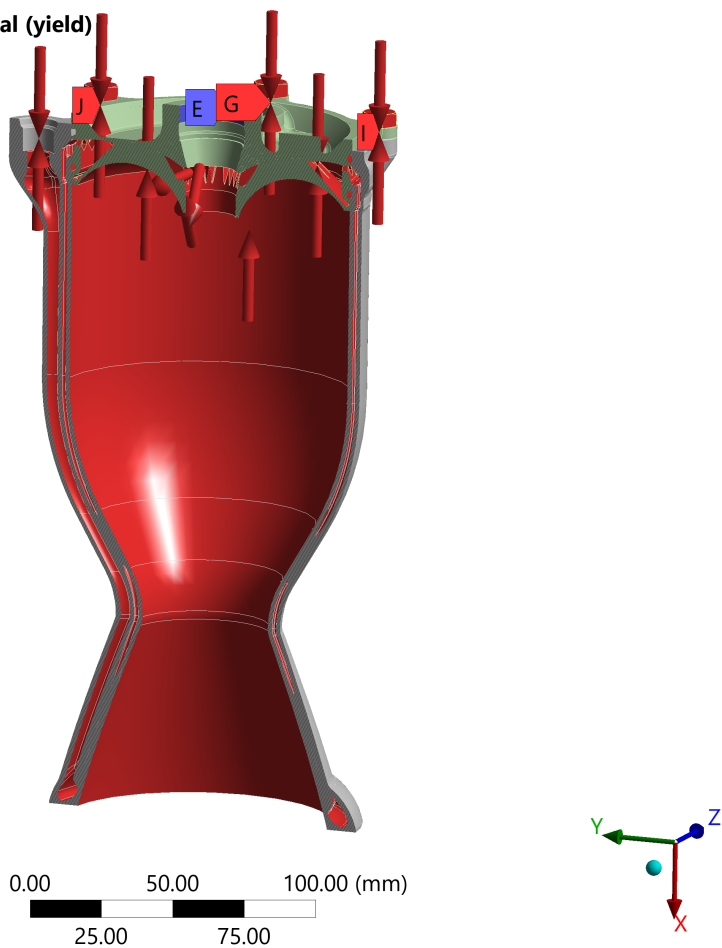


Figure 35: Combined Setup

**Frictionless-Injector to Combustion chamber Bore**

5/14/2025 4:29 PM

- Frictionless-Injector to Combustion chamber Bore (Contact Bodies)
- Frictionless-Injector to Combustion chamber Bore (Target Bodies)

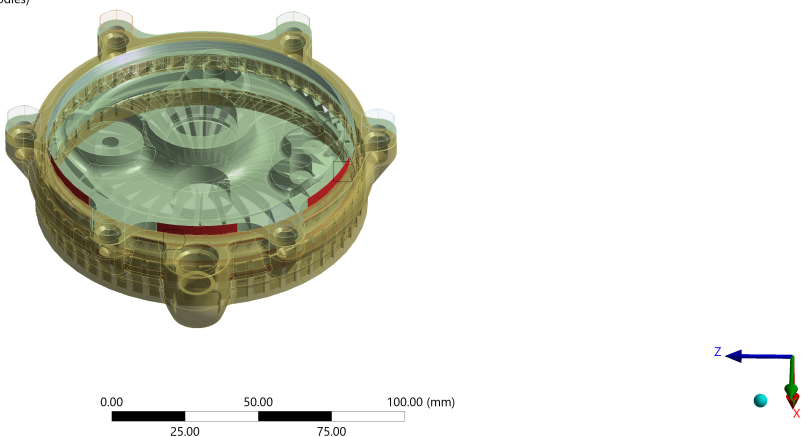


Figure 36: Frictionless Bore Contact

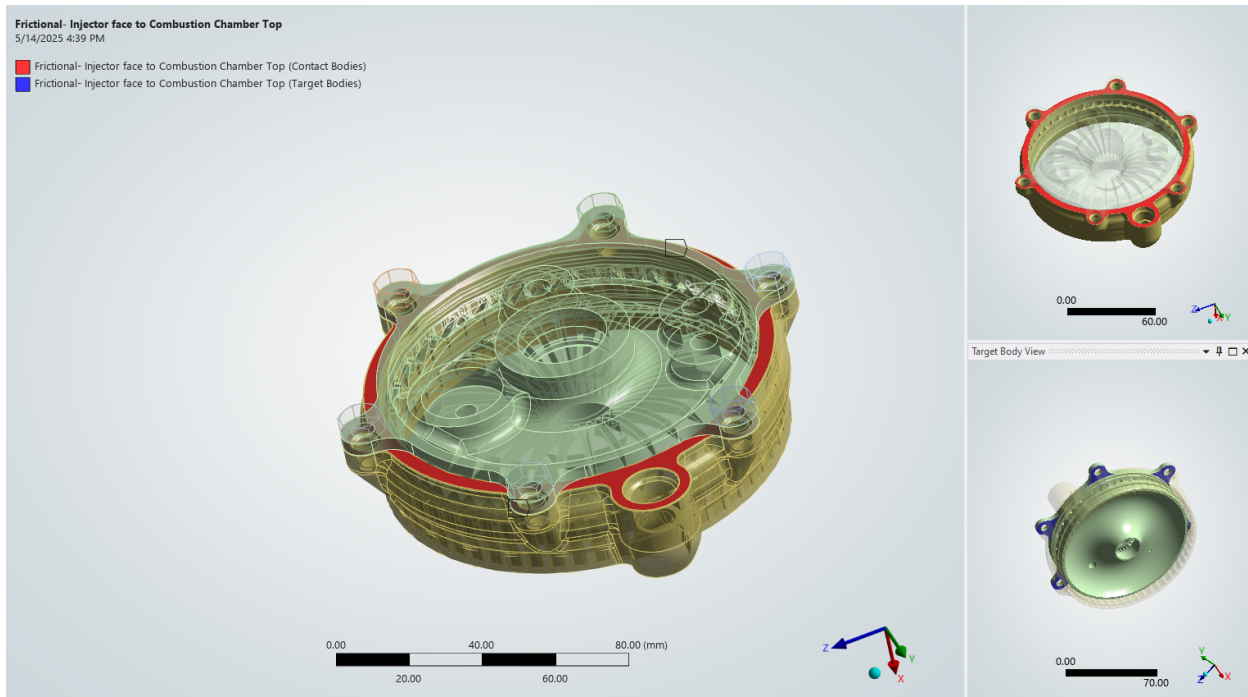


Figure 37: Injector Face to Combustion Chamber Top

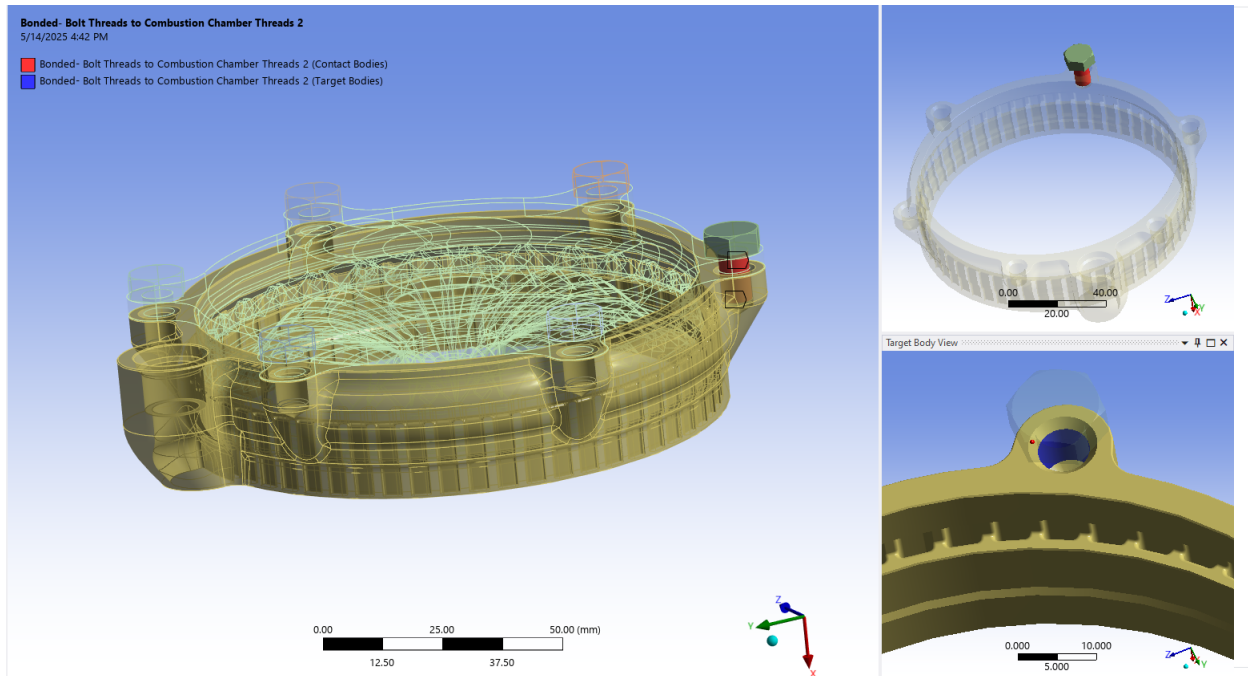


Figure 38: Bonded Bolt Threads to Combustion Chamber Threads

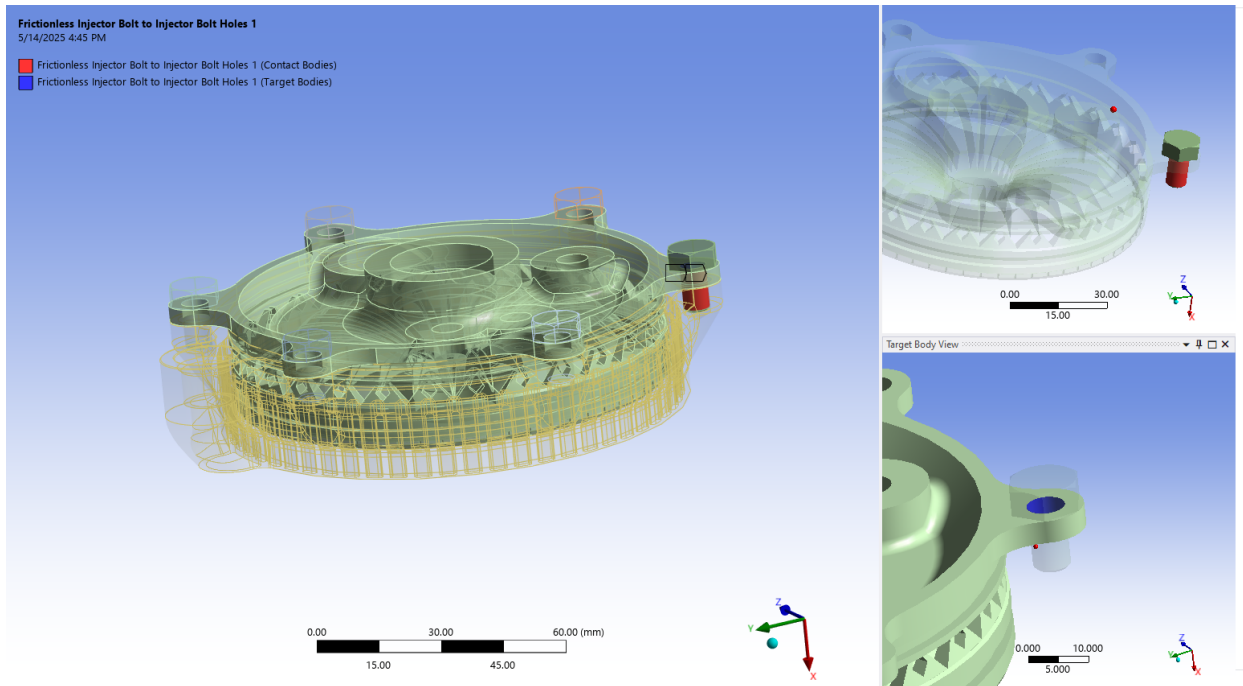


Figure 39: Frictionless Bolt Shank to Injector Clearance Holes

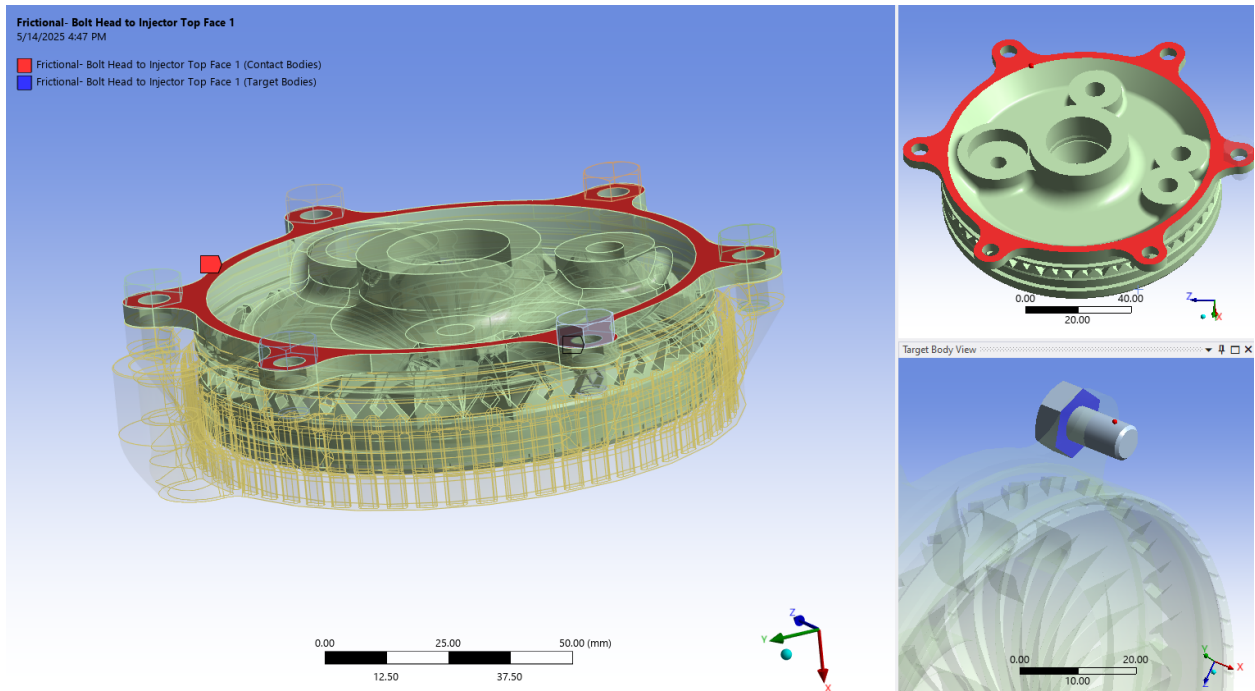


Figure 40: Bolt Head to Injector Top Face

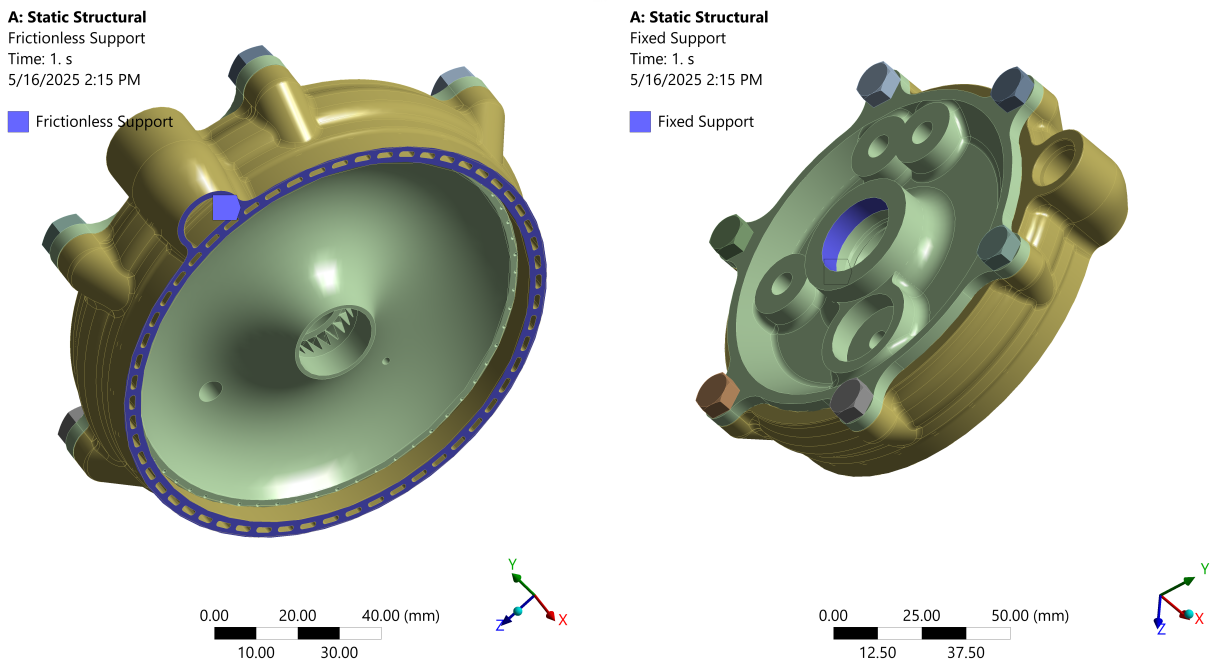


Figure 41: Supports

## 15.4 Loads

The yield load factor is 1.5, and the ultimate load factor is 2.0. The load factor method is used rather than analyzing safety factor because there are nonlinear effects that invalidate any simple scaling of results. Multiple pressure load cases were considered:

### 1. Fuel Channel Pressure

- Yield pressure: 1500 PSI (10.34 MPa)
- Ultimate pressure: 2000 PSI (13.74 MPa)

### 2. Combustion Chamber Internal Pressure

- Yield pressure: 525 PSI (3.61 MPa)
- Ultimate pressure: 700 PSI (4.82 MPa)

### 3. Thermal Stress

- Imported thermal loads from RPA

### 4. Preload

- 9000N of preload is applied to each bolt

## 15.5 Preload

The injector is attached to the chamber body with a bolted joint. The bolted joint in this analysis is modeled with the actual bolt body rather than beams to capture more information about the joint. The bolts must be preloaded such that the joint does not separate when the engine is at operating pressure. The bolts must provide enough clamping force to overcome the force of the chamber pressure pushing on the injector.

$$A = 13.5 \text{ in}^2 \quad (4)$$

$$P = 350 \text{ psi} \quad (5)$$

$$F_{\text{total}} = P A = 350 \frac{\text{lbf}}{\text{in}^2} \times 13.5 \text{ in}^2 = 4725 \text{ lbf} \quad (6)$$

$$= 4725 \text{ lbf} \left( 4.44822 \frac{\text{N}}{\text{lbf}} \right) \approx 2.10 \times 10^4 \text{ N} \quad (7)$$

$$n_{\text{bolts}} = 6 \quad (8)$$

$$F_{\text{per bolt}} = \frac{F_{\text{total}}}{n_{\text{bolts}}} = \frac{2.10 \times 10^4 \text{ N}}{6} \approx 3.50 \times 10^3 \text{ N} \quad (9)$$

$$\approx 786 \text{ lbf} \quad (10)$$

Each bolt must provide at least 786 lbf of clamping force. This value is inputted into the bolted joint spreadsheet, based on NASA STD\_5020.

Because there is a Helicoil, we have to do the bolted joint calculations in several steps as shown in the above figures. The first step is calculating how much preload is required to prevent joint separation. The pressure force is applied as the Tension limit load. There should be no shear load in this joint, but 100 lbf is used as a placeholder value. Next, the joint dimensions are inputted. The Helicoil length is 1.0D which means it is 0.25. This value is used for the engagement depth. Next, the material is inputted, and the insert is stainless steel. The preload is adjusted such that the joint has a positive margin for separation. This is a "separation critical joint" so there is already a 1.4FOS applied to the joint separation.

The negative margin on yield is ignored, as it is local non detrimental yielding of the Helicoil and the fatigue life of this engine is not relevant.

Next, the combustion chamber to Helicoil bolted joint is analyzed in a similar manner. Joint separation is not relevant in this calculation because we are only considering the interaction between the Helicoil and the chamber.

This joint passes. The 1/4 28 fastener should be tightened to 65 in-lbs for a nominal preload of 1733lbf. The preload upper bound is 1950 lbf , which equals roughly 9000N, which is what was used for the preload value in Ansys.

Pressure loads are applied to internal faces as shown below. Fuel pressure is applied to all surfaces that are in contact with fuel, and chamber pressure is applied to all internal faces that are in contact with chamber gases. The same loads are applied to all models as seen in Figure 35.

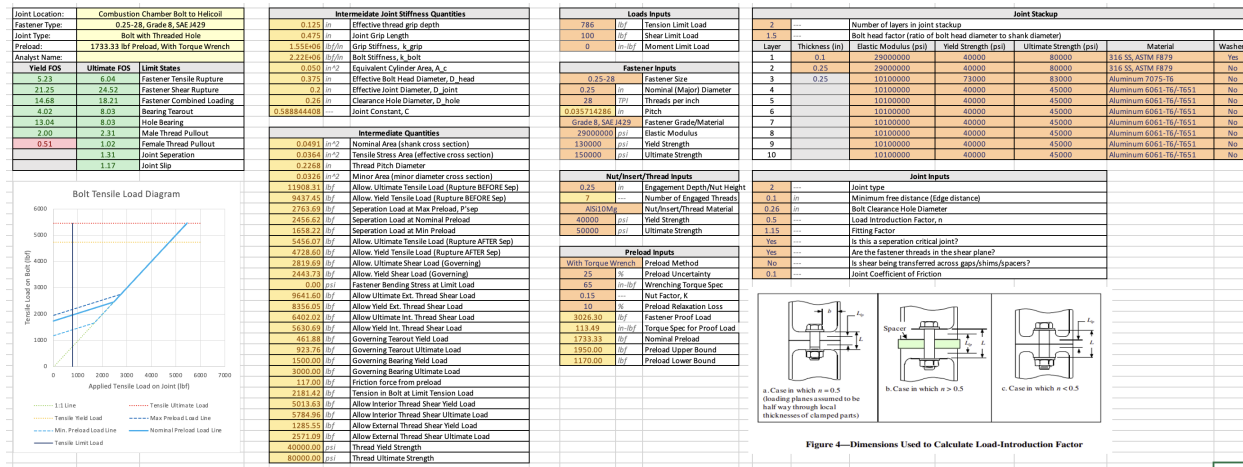


Figure 42: Combustion Chamber Bolt to Helicoil

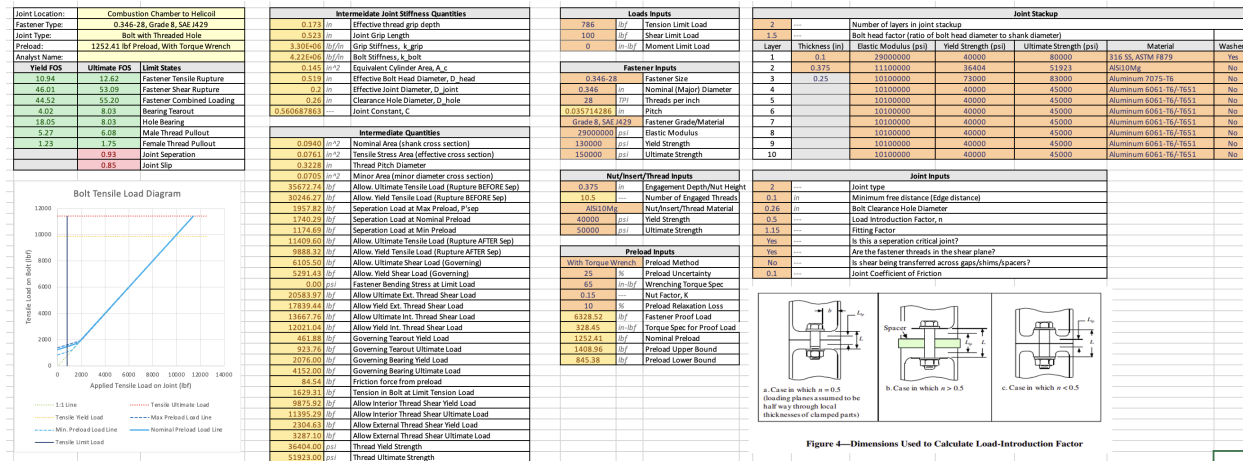
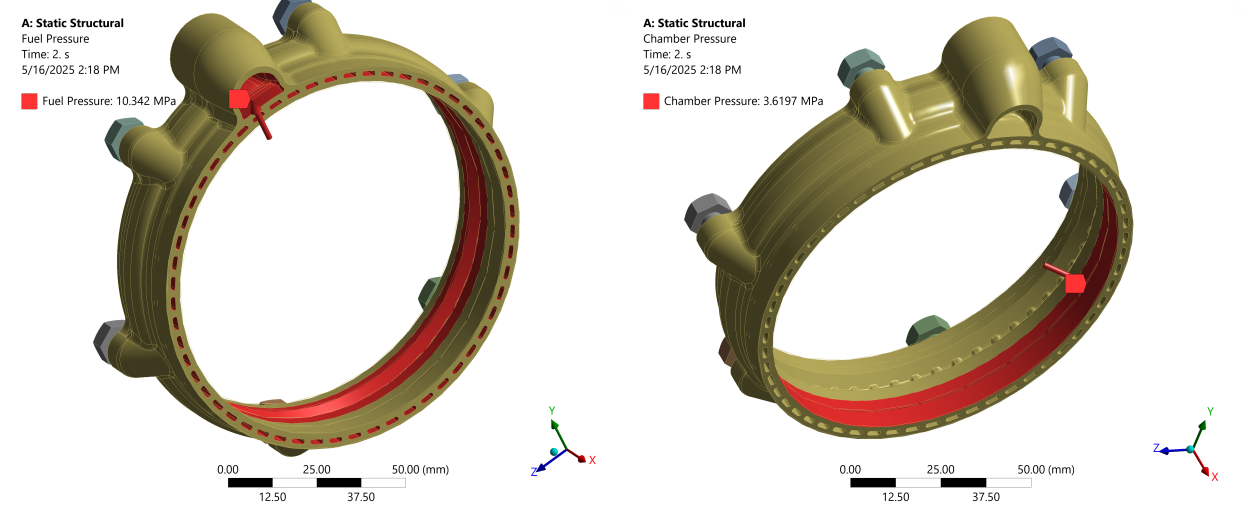


Figure 43: Combustion Chamber to Helicoil



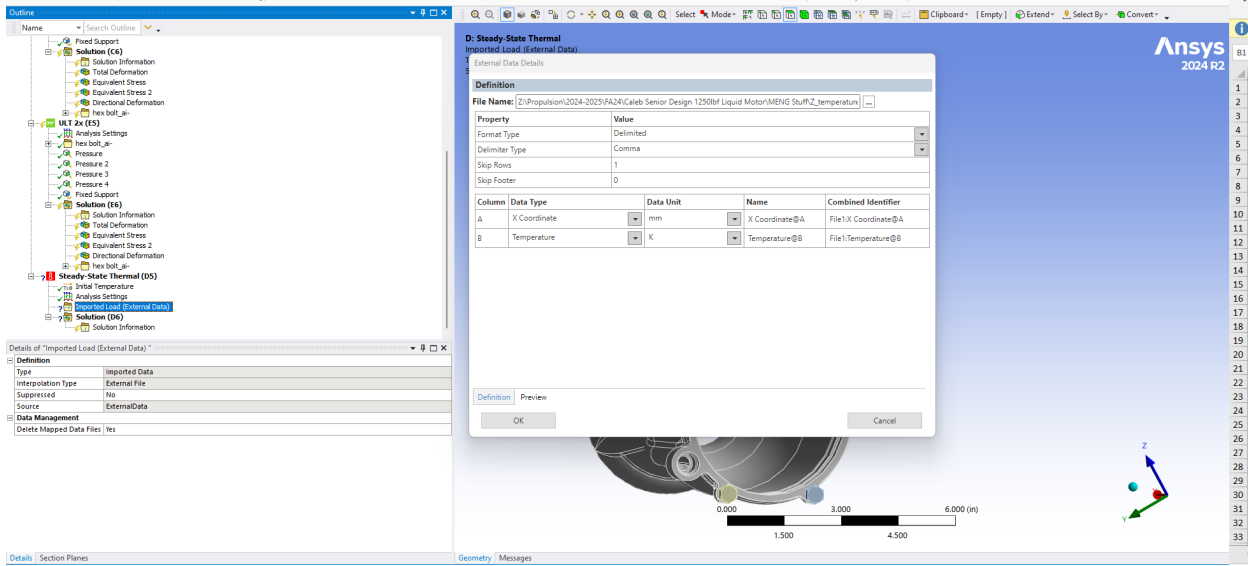


Figure 45: Thermal Coupling Setup

## 15.6 Thermal-Structural Coupling

The temperature results from RPA as seen in Figure 17 were imported into Ansys to evaluate thermal stresses:

1. Temperature data was exported from RPA into CSV format with axial location and wall temperature
2. A steady-state thermal analysis module was created in Mechanical
3. Imported load data was applied to the appropriate surfaces
4. Temperature distributions were mapped to the structural model

The wall temperatures (TWG) are mapped to the inner combustion chamber faces, while the cool side temperatures (TWC) are mapped to the inside of the cooling channels. The spiky initial temperature fluctuations observed in some results were identified as numerical instabilities related to the Bartz singularity, where the convective heat transfer coefficient yielded “nan” values at positions below 20 mm. For analysis purposes, these areas were smoothed using stable temperature values from adjacent regions.

The steady-state thermal analysis yielded wall temperatures reaching a maximum of approximately 465 K at the throat as expected. The thermal gradient is captured accurately, which will serve to model thermal stresses in areas with high temperature differentials.

While these results provide good insight into operational temperatures, they do not capture the initial transient conditions where thermal stresses would be significantly higher. Additionally, the model does not incorporate the complete heat transfer mechanisms present in the actual engine. However, these transient effects are expected to be balanced out by the fact that AlSi10Mg has a much higher yield and ultimate strength when cold.

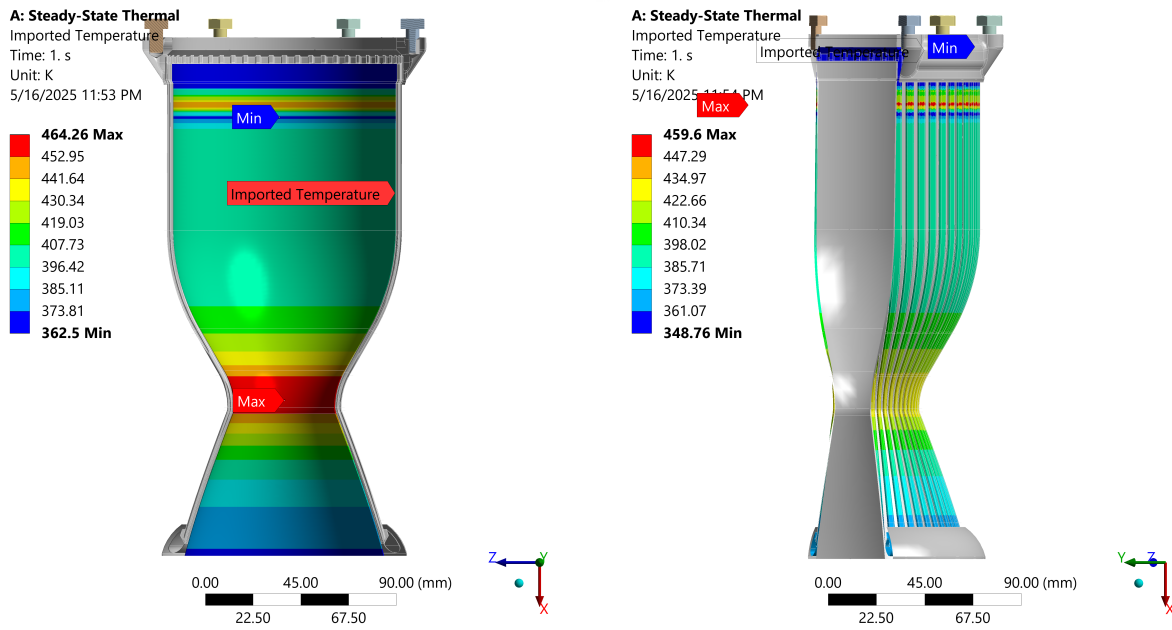


Figure 46: Raw RPA Imported Temperatures

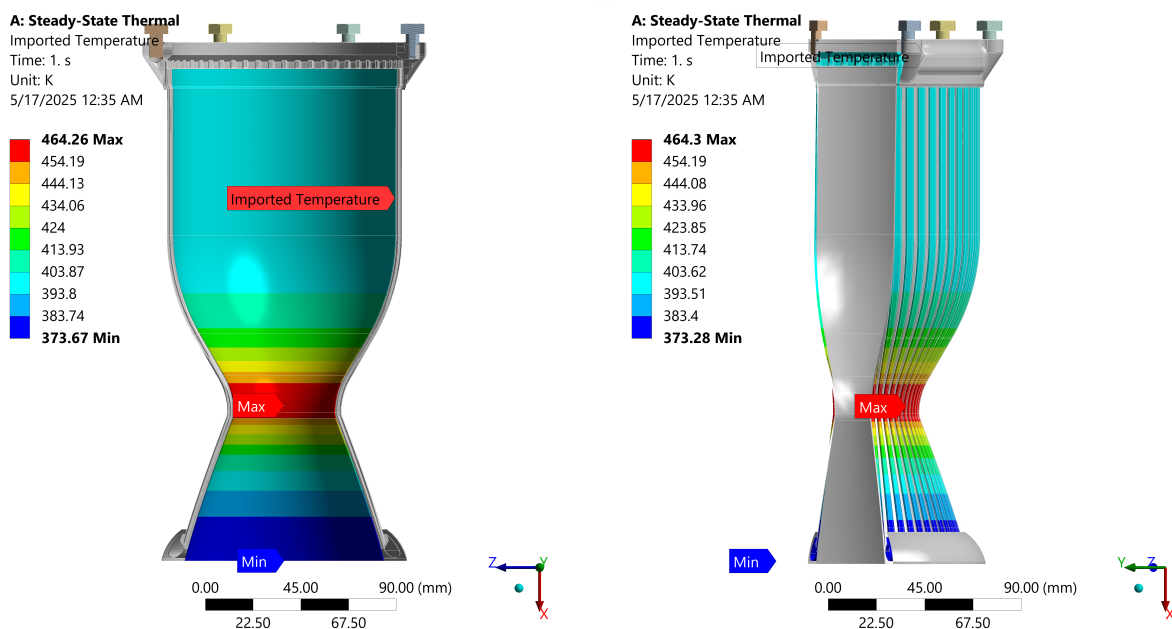


Figure 47: Smoothed RPA Imported Temperatures

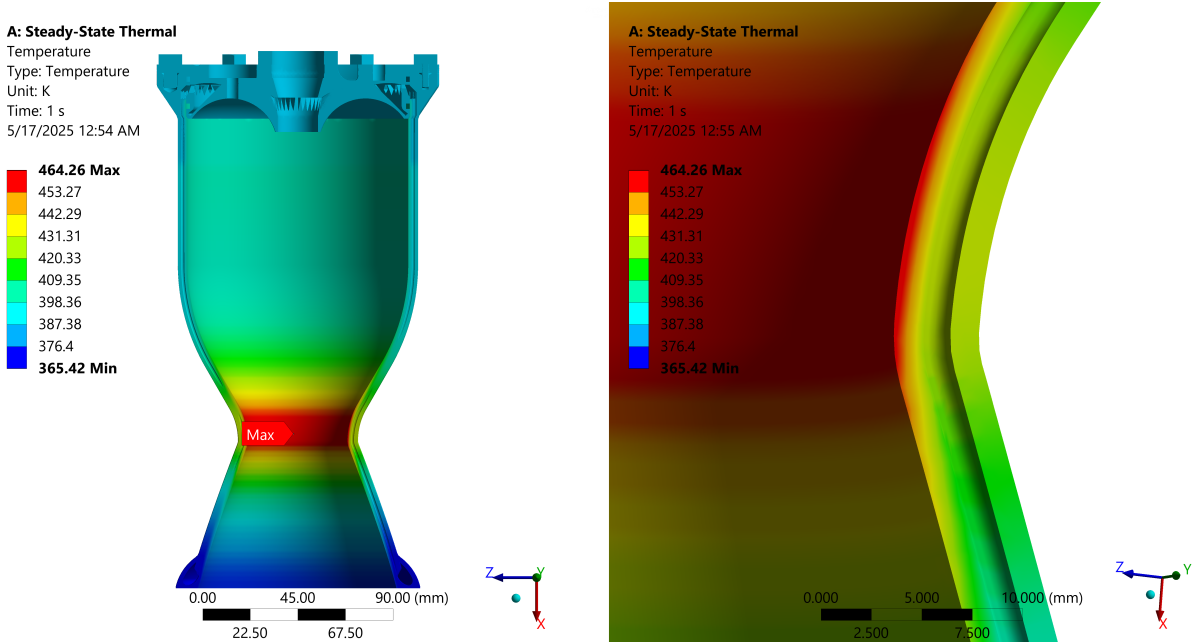


Figure 48: Steady-State Temperature

The Thermal stress reaches a maximum of 90 MPa at the throat. This is expected due to the thermal gradient being the greatest at this area. The results for 1.5x MEOP show that the Von Mises stress does not exceed 253 MPa. The peak stress is observed at the edge of the cooling channel, which is not entirely unexpected. The feature is small, and has sharp edges. Any yielding in this area would be non-detrimental. There is also high stress near the bolt interfaces, however this is also expected. Again, there is a sharp chamfer which is a stress concentration. This is not a concern as the preload will be less in the actual build, which will reduce this stress. Local yielding is also non detrimental in this area. The results for 1.5x MEOP combined with thermal loading show an identical peak stress, but higher mean stress, especially in the chamber. This is acceptable.

Stress does not exceed the Ultimate Tensile Strength at any location in this result. Above is shown the mesh used in the combined analysis modules. This mesh is comprised of 1.6 million elements. Mesh quality is acceptable, but there are many elements with a high aspect ratio. This will reduce accuracy especially in areas of high stress.

A higher mesh fidelity was desired on the top of the combustion chamber, so a breakout model was used there to allow for more elements on the through thickness without exceeding the solve capabilities of the Swanson machines. A nonlinear adaptive method was attempted to increase mesh fidelity where strain energy exceeded a set criterion. This method is promising because it can theoretically reduce the burden of analysis preparation of breakout models by only refining the mesh in areas that are under stress. In this way, the manual labor required to prepare the ANSYS model is much less, so any design changes can be quickly re-analyzed. No breakout models would be needed, because the element count would be low enough to be solved directly. This method did not initially work on the combined chamber, so I made a breakout model to refine the parameters. This breakout model is a bolted joint under preload and pressure. It functioned exactly as expected.

**B: Thermal Stress Only**

Figure

Unit: MPa

Time: 1 s

5/18/2025 12:51 AM

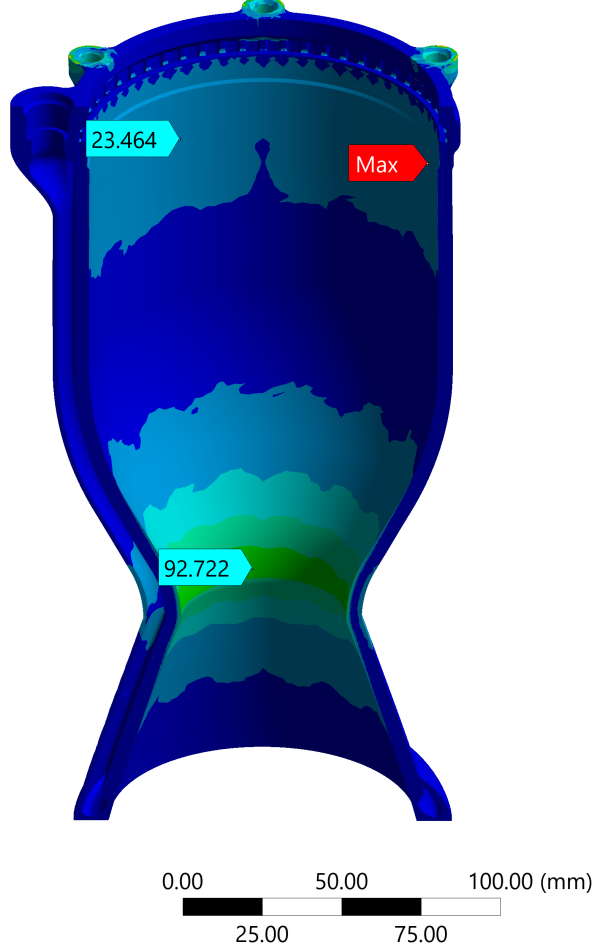
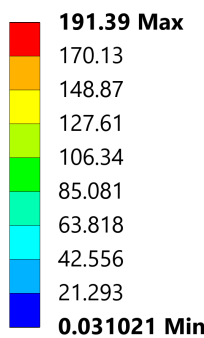


Figure 49: Thermal Stress

**D: 1.5x MEOP Pressure Loading+Thermal (yield)**

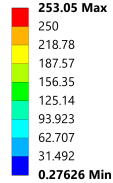
Equivalent Stress 2

Type: Equivalent (von-Mises) Stress

Unit: MPa

Time: 2 s

5/18/2025 1:12 AM

**D: 1.5x MEOP Pressure Loading+Thermal (yield)**

Equivalent Stress 2

Type: Equivalent (von-Mises) Stress

Unit: MPa

Time: 2 s

5/18/2025 1:13 AM

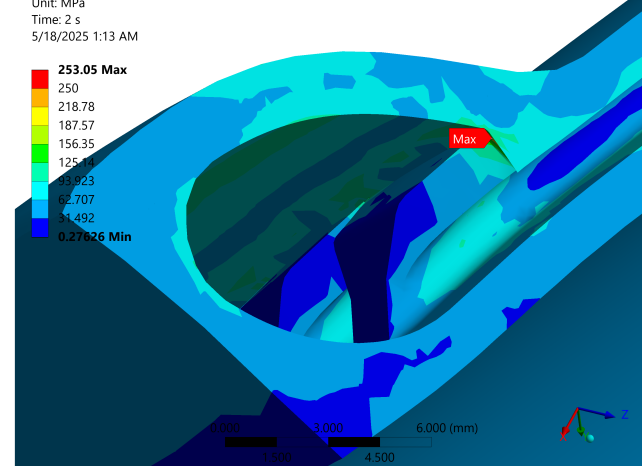
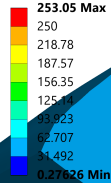


Figure 50: Enter Caption

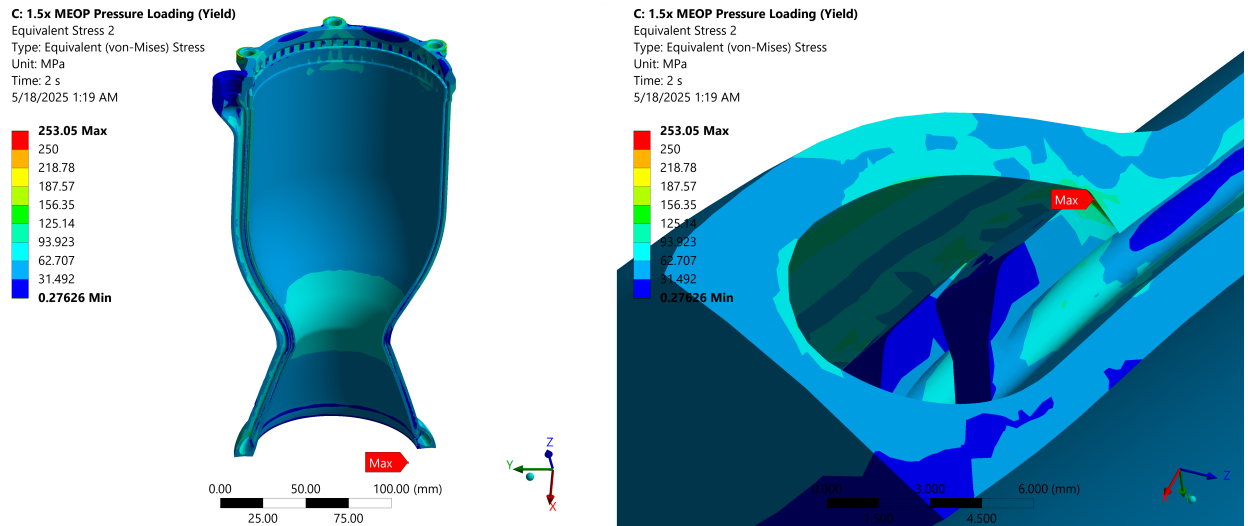


Figure 51: Yield Pressure Only

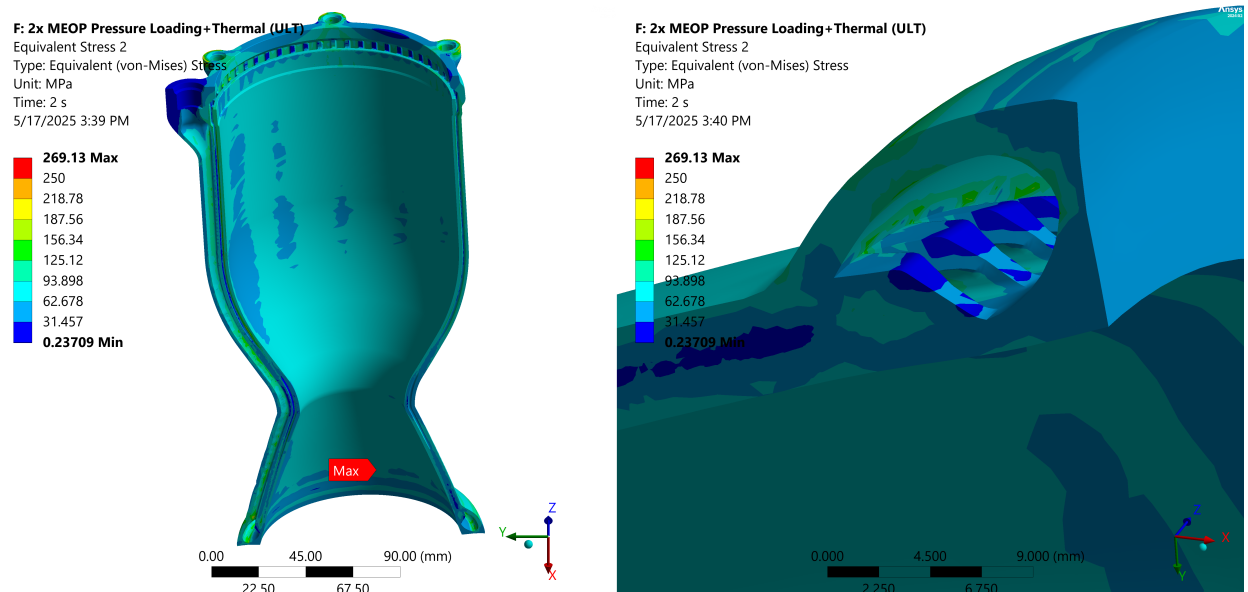


Figure 52: Ultimate Pressure and Thermal loading

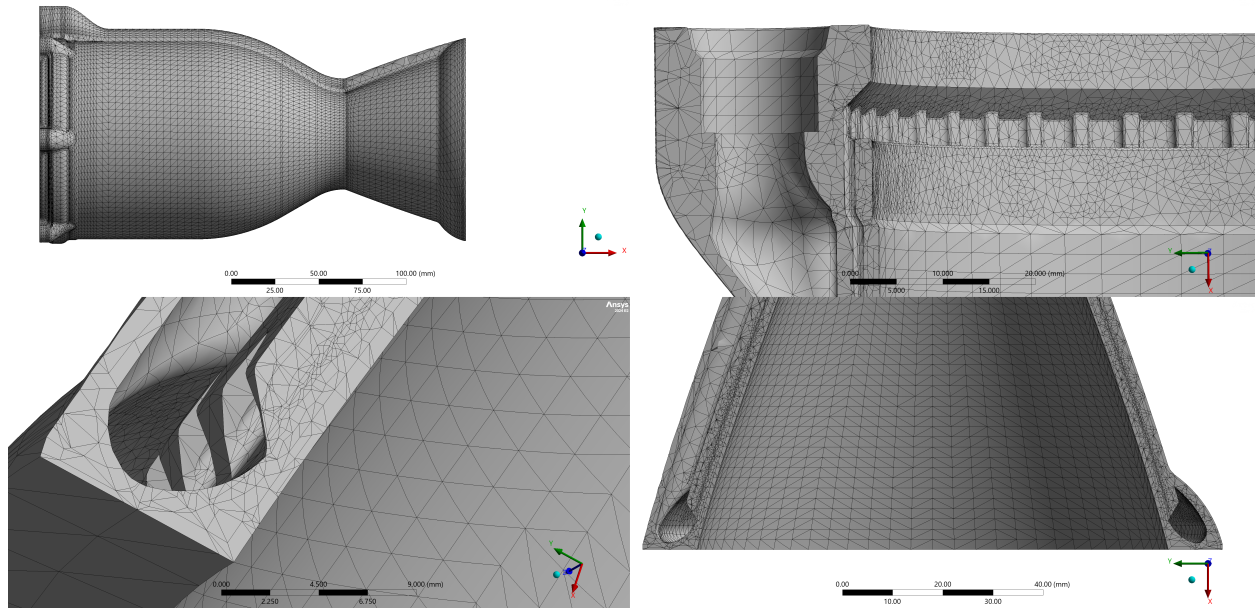


Figure 53: Combined Mesh

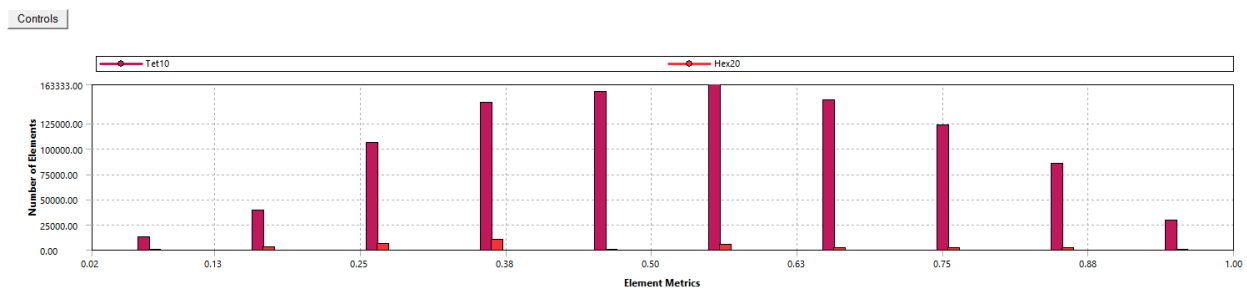


Figure 54: Combined Mesh Quality

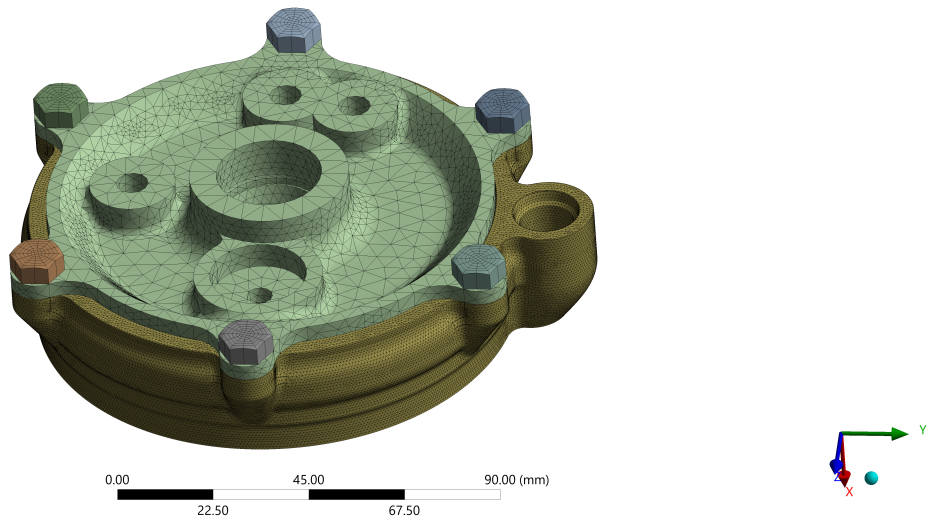


Figure 55: Breakout Model Mesh

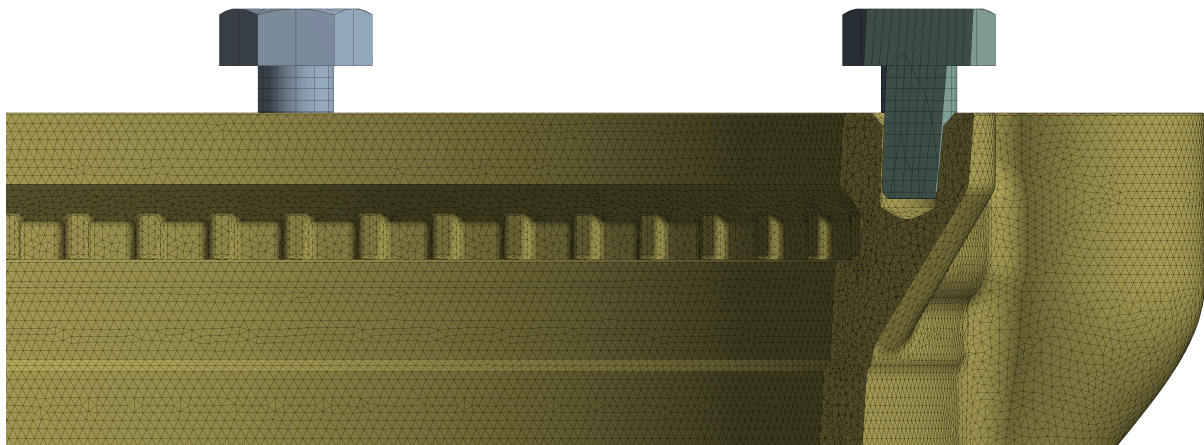


Figure 56: Breakout Mesh-Chamber and Bolts Cross Section

Again, This method was attempted on the full chamber, but because of the geometrical complexity of the engine chamber, the solver rejected this method for unknown reasons. Because there was no diagnostic path to follow, the method was deemed fruitless at this point in time. The nonlinear adaptive region is a new feature that seems to be very promising, but not quite fully developed.

## 15.7 Sectioned Breakout Model

A breakout model was made of the top of the combustion chamber combined with the injector to more accurately analyze the stress in this area. Because the model is smaller, a finer mesh can be used without an unreasonable number of elements. The breakout mesh is comprised of 1.5 million elements, which is comparable to the combined model, however

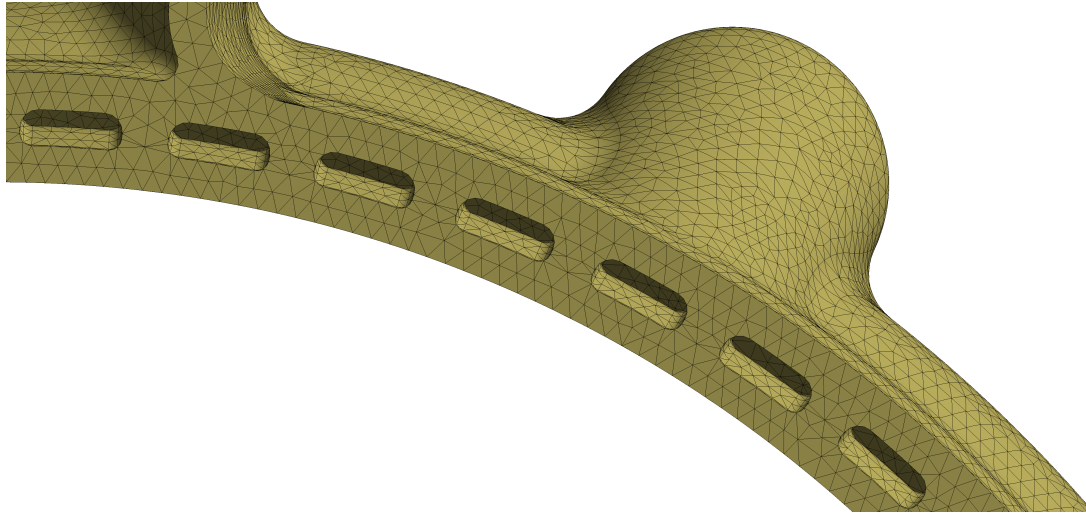


Figure 57: Breakout Mesh Through Thickness

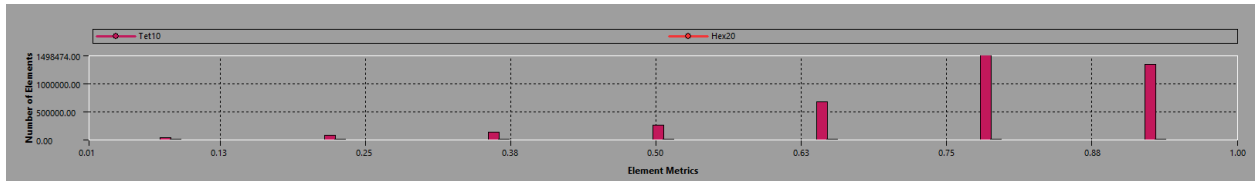


Figure 58: Breakout Mesh Quality

the element size is much smaller, at 0.8mm. This also allowed the element quality to increase significantly, all without increasing computation time. Additionally, two through thickness elements are now present in all areas, greatly increasing the accuracy of stress results due to pressure loading. Thermal loading is not considered in this area because there is no temperature data for the injector. There is an area of high stress on the inner wall of the fuel channel by the fuel inlet port. This area of high stress may exist along the whole length of the fuel transfer tube

This area of high stress is less pronounced on the full ANSYS model. On the breakout model, these areas of particularly high stress are within 2mm of the boundary, which may be contributing to this effect. Because the boundary is frictionless, the wall only has two degrees of freedom, moving outward, or rotating. As the walls are forced outward by the pressure, a local bending moment is created on the inside of the channel. This same area on the full model does not have the same high stress locations. This may be in part due to a less refined mesh, however it is more likely that the boundary condition in the sliced model caused this high stress area.

The other high stress area is right around the bolts, which is expected and does not exceed ULT, or exceed maximum strain values.

Strain reaches a maximum of 0.39% which is far below the fracture strain of 9%. In the 1.5x load factor results, the directional deformation in the radial direction reaches a maximum of 0.0031". This clearance should be considered with the existing O ring clearance to ensure that it does not exceed acceptable values and cause an O ring failure.

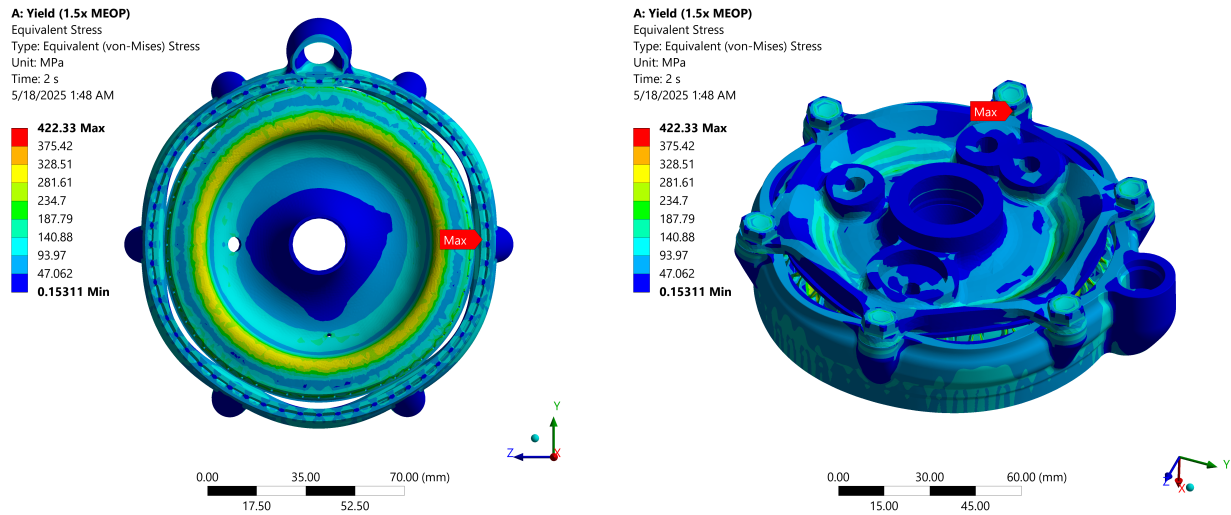


Figure 59: 1.5x MEOP Pressure Load Combined

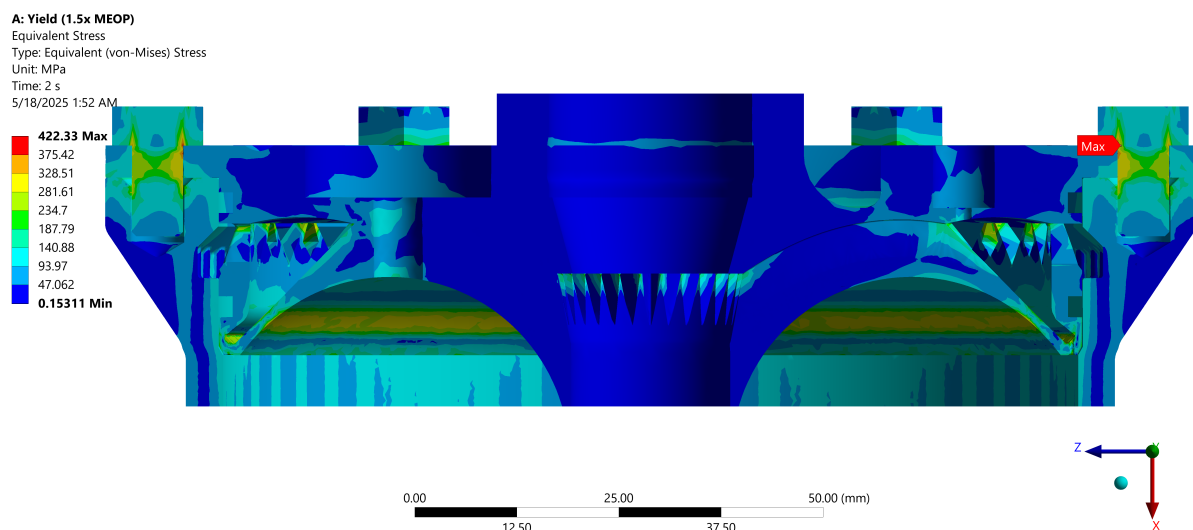


Figure 60: 1.5X MEOP Cross Section

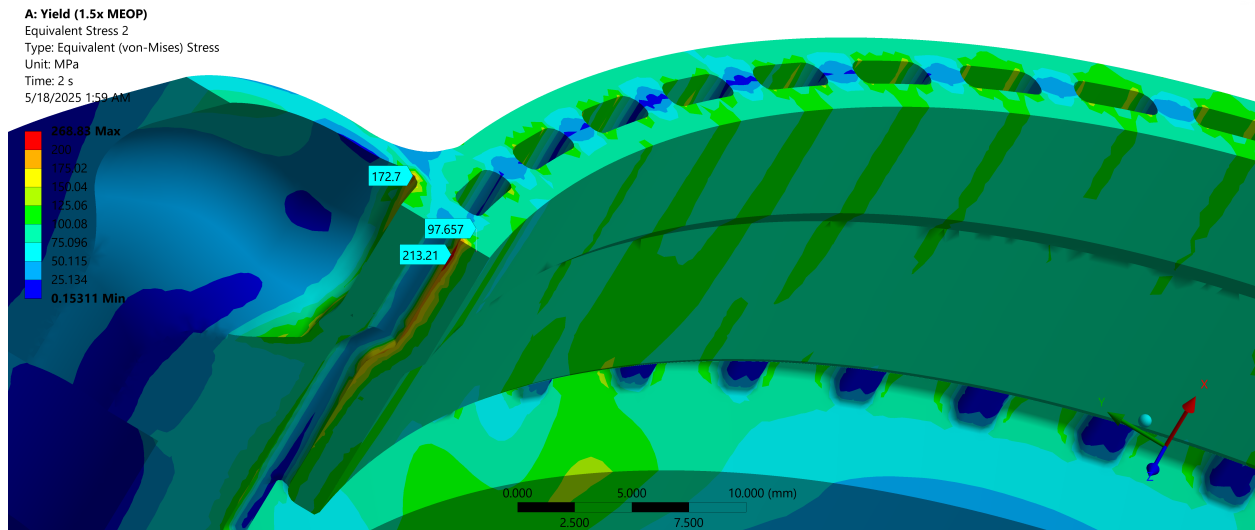


Figure 61: Yield High Stress Locations

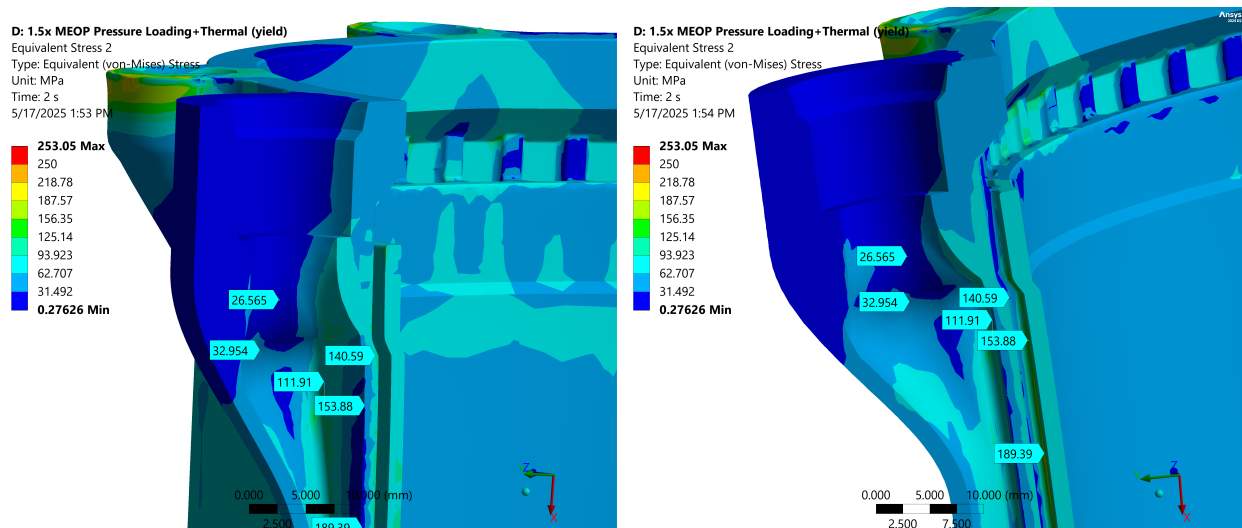


Figure 62: High Stress Areas Combined Model

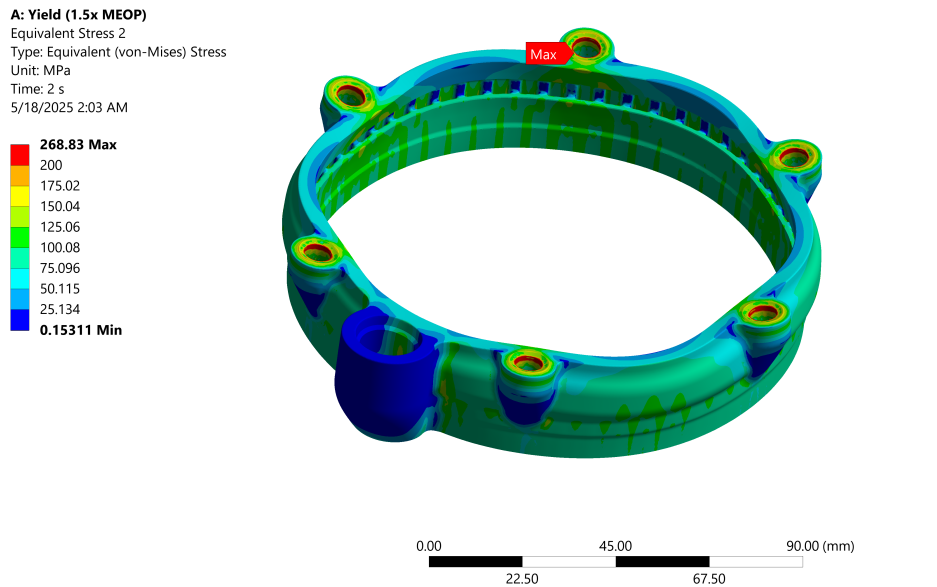


Figure 63: Sliced Chamber Yield Results

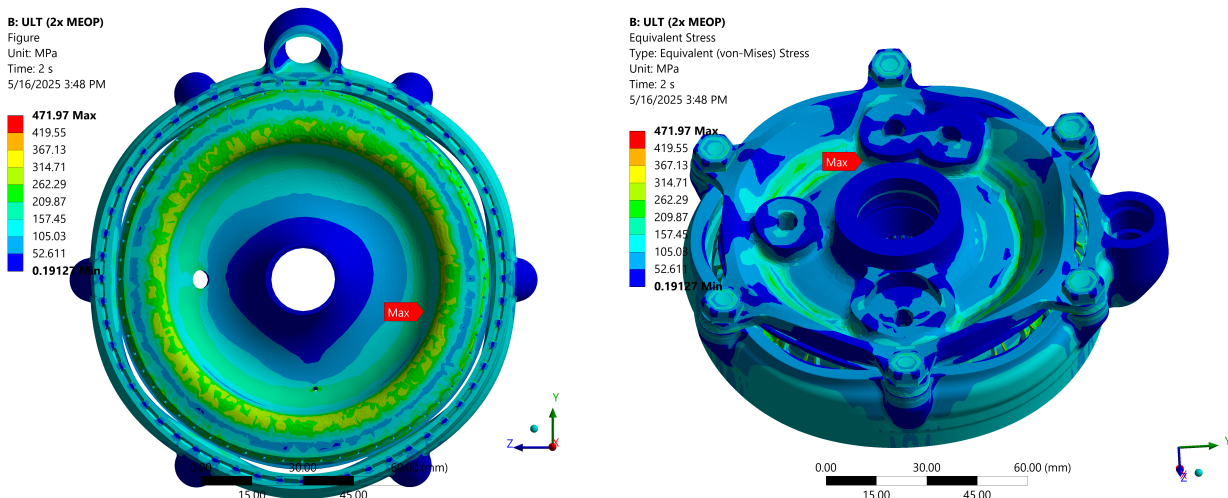


Figure 64: 2x MEOP Ultimate Load Sliced Model

**B: ULT (2x MEOP)**

Figure 2

Unit: MPa

Time: 2 s

5/16/2025 3:56 PM

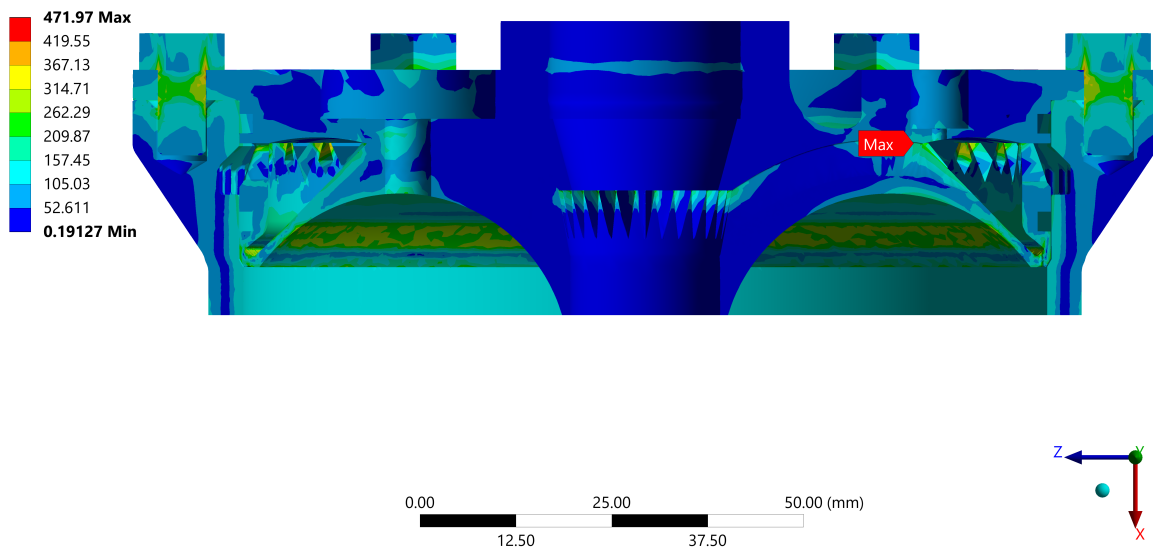


Figure 65: 2x MEOP Ultimate Cross Section

**B: ULT (2x MEOP)**  
Equivalent Stress 2  
Type: Equivalent (von-Mises) Stress  
Unit: MPa  
Time: 2 s  
5/16/2025 3:59 PM

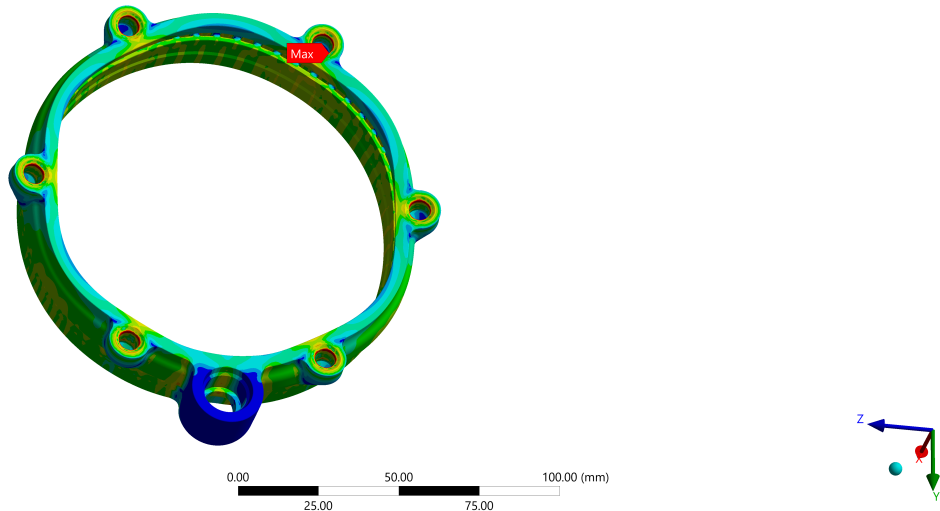
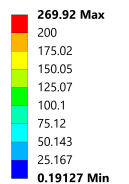


Figure 66: 2x MEOP Ultimate Chamber

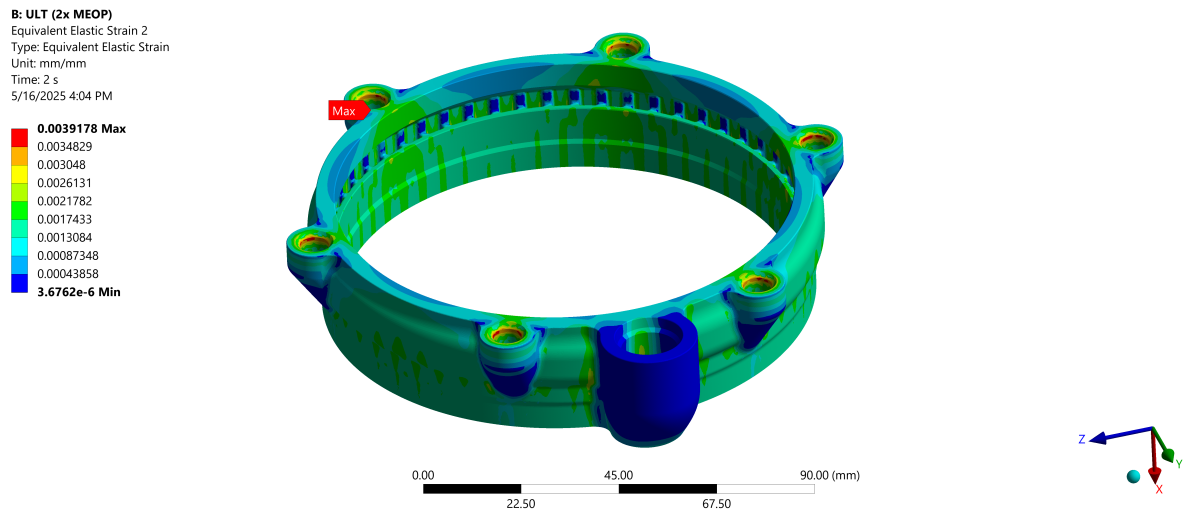


Figure 67: 2x MEOP Ultimate Strain

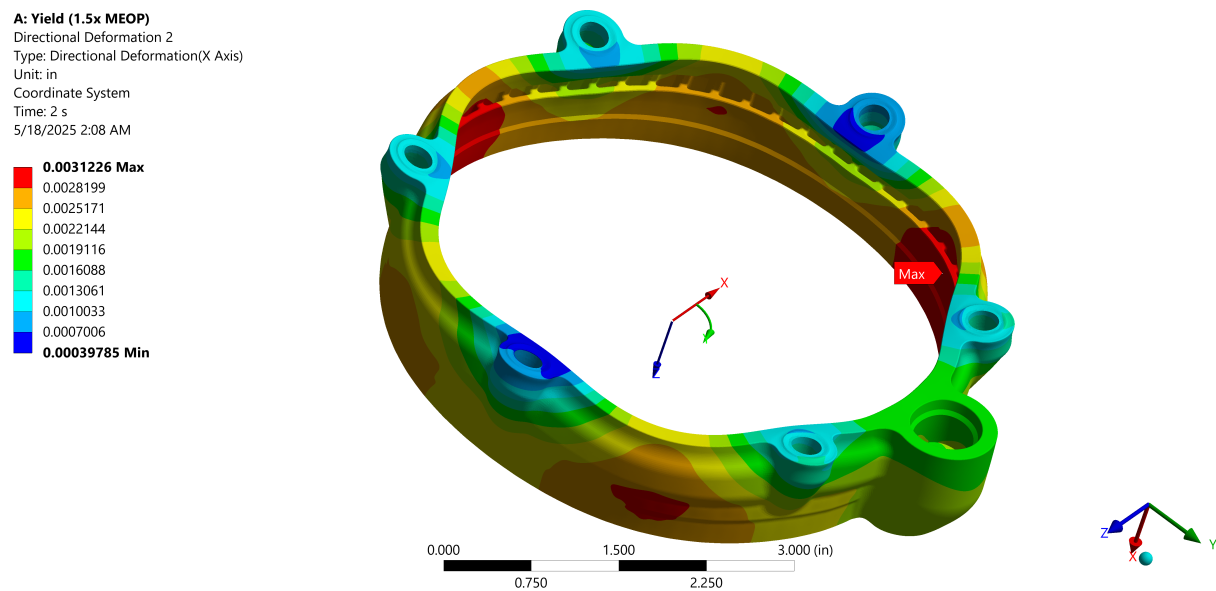
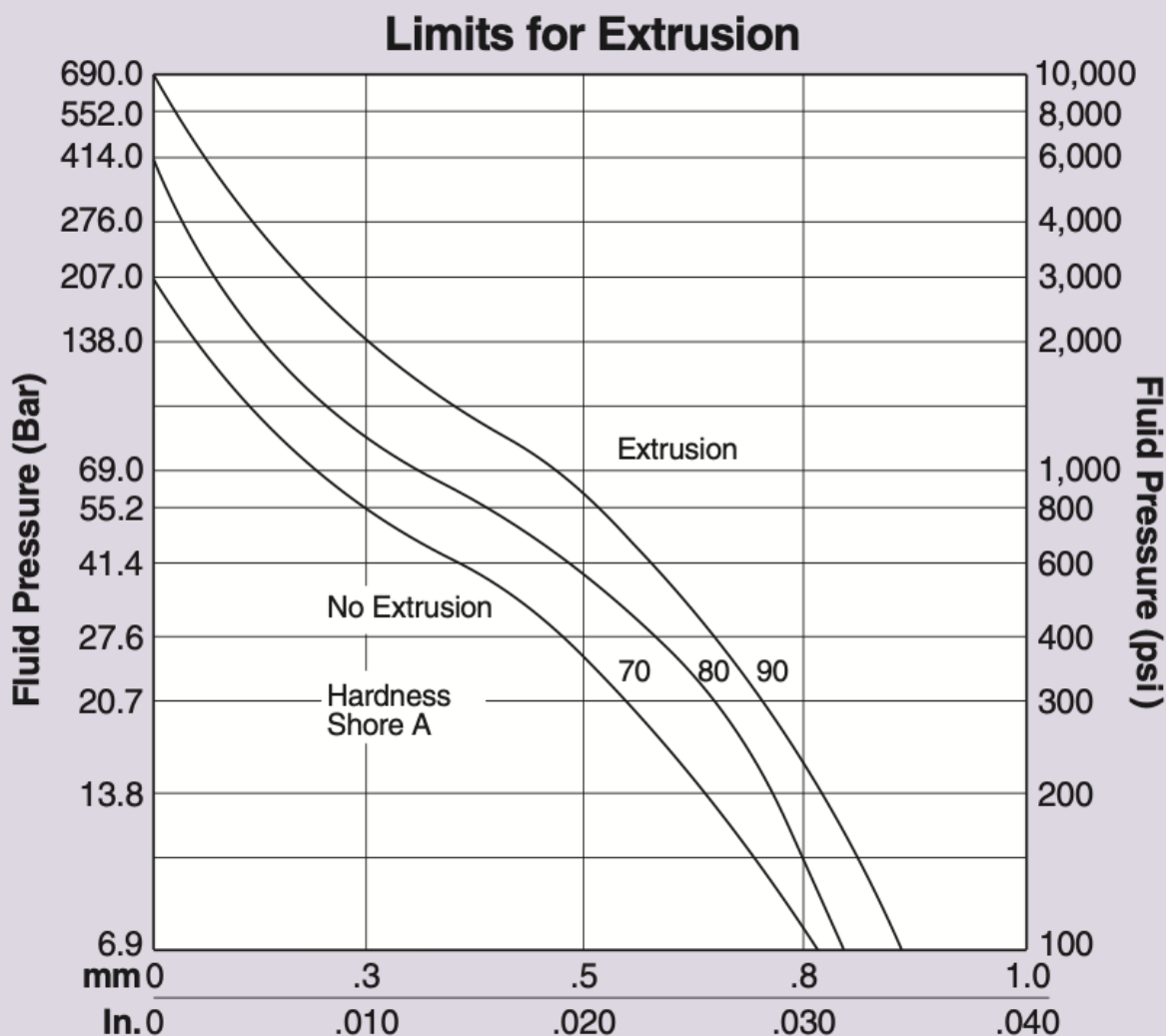


Figure 68: Chamber Directional Deformation



#### Basis for Curves

1. 100,000 pressure cycles at the rate of 60 per minute from zero to the indicated pressure.
2. Maximum temperature (i.e. test temperature) 71°C (160°F).
3. No back-up rings.
4. Total diametral clearance must include cylinder expansion due to pressure.
5. Apply a reasonable safety factor in practical applications to allow for excessively sharp edges and other imperfections and for higher temperatures.

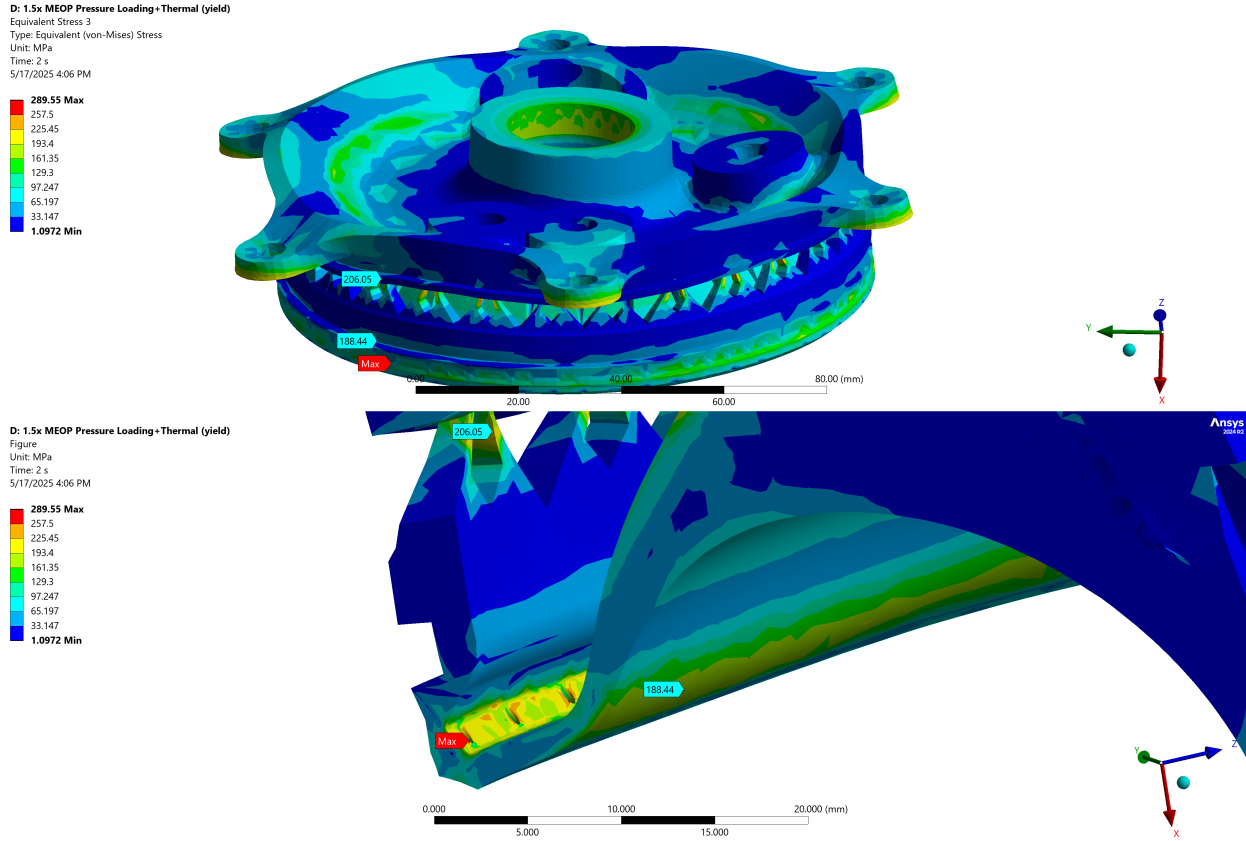


Figure 70: Injector 1.5x MEOP Pressure Loading + Thermal

According to the Parker O-ring handbook, approximately 0.012" of diametral clearance is acceptable at 1000 PSI. The design provides a nominal diametral clearance of 0.003-0.006 inches, which combined with the maximum calculated deformation of 0.003 inches results in a maximum diametral clearance of 0.009 inches during operation. This remains within acceptable limits to maintain proper sealing.

The O-rings will only be in contact with fuel and combustion chamber gases so fluorosilicone O rings are not needed. These O rings will be exposed to combustion chamber temperatures, as well as combustion chamber gases and unburnt fuel and oxidizer. The safest option would be to choose Kalrez or Viton O rings. Viton o rings will be much less expensive, and can withstand up to 500K.

## 15.8 Injector Analysis

The injector was not a focus of the FEA study because the geometry is not completely finalized. However, the ANSYS results can still serve as a reference to inform future design improvements. Apart from the stress concentrations around the film cooling holes, it appears that the injector will withstand nominal structural loading.

## 15.9 Analysis Approach

The implementation of the 3-2-1 method for constraints was applied, which restrains 3 points on a plane in translation to better simulate real-world mechanical constraints. This approach significantly improved the fidelity of the analysis results.

For the CFD analysis, boundary conditions were defined as:

- Inlet pressure: 552,909 Pa
- Outlet pressure: 722 Pa
- Resulting pressure drop: approximately 80 PSI

A combined structural analysis including bolts was conducted to validate whether the observed yielding at the top of the chamber was a real phenomenon or an artifact of the simplified model.

## 15.10 Stress Analysis Results

The von Mises stress distribution showed acceptable levels throughout the chamber body, with localized regions of high stress around bolt holes as expected. Stress in these areas remained below ultimate limits and did not indicate a risk of failure.

The elastic-plastic analysis with large deflection and nonlinear material properties showed that the structure remained intact at ultimate load with no separation of the bolted joint interface. Maximum strain reached 0.39%, which is significantly below the fracture strain of 9% for the AlSi10Mg material.

In the 1.5x load factor analysis, the directional deformation in the radial direction reached a maximum of 0.0031 inches. This deformation was evaluated in conjunction with the existing O-ring clearance to ensure it would not exceed acceptable values or compromise sealing performance.

According to the Parker O-ring handbook, approximately 0.012" of diametral clearance is acceptable for the application. The design provides a nominal diametral clearance of 0.003-0.006 inches, which combined with the maximum calculated deformation of 0.003 inches results in a maximum diametral clearance of 0.009 inches during operation. This remains within acceptable limits to maintain proper sealing.

# 16 Thermal Analysis and CFD

## 16.1 CFD Setup and Methodology

The Computational Fluid Dynamics analysis utilized a 3D pressure-based model with SST k-omega turbulence modeling. The mesh generated for the analysis contained 9,950,025 cells with 49,014,118 faces and 32,472,736 nodes. Mesh quality metrics were monitored, with:

- Minimum orthogonal quality = 0.26141

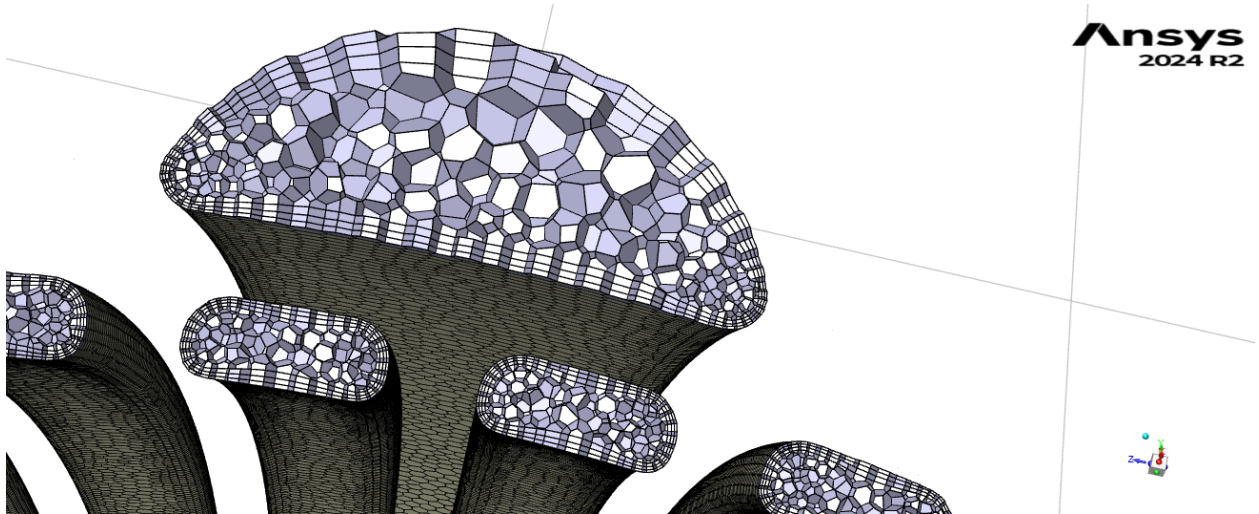


Figure 71: Inlet Mesh Cross Section

- Maximum aspect ratio = 88.737

Mass flow boundary conditions were implemented at both inlet and outlet, with modeled surface roughness to capture realistic flow behavior. The model geometry was prepared using watertight meshing in SolidWorks and Ansys Discovery.

## 17 CFD Results

The fluent results for coolant velocity closely matches the RPA results. The discrepancy in velocity is likely due to the slightly different geometry in CAD vs the cooling channels modeled in RPA, as the RPA channels are rectangular but the CAD channels have rounded corners, slightly reducing the cross sectional area. This increases peak velocity a minor amount. A more significant effect is seen from 0-0.09m from the outlet, where the coolant velocity is around 0.9m/s less than in RPA on average. This will increase the temperature of this region, as the heat transfer coefficient is heavily dependent on velocity. A cross section was taken at the throat and at the middle of the combustion chamber. The throat experiences extremely high heat flux, so it is critical that the coolant is traveling at the correct velocity and that the coolant is uniformly distributed around the chamber. The midchamber cross section is analyzed to determine the average coolant velocity, because the single streamline plot is not accurate enough to conclude whether the coolant is matching the RPA simulated values.

The coolant is traveling significantly faster through the channels which are at a similar clocking to the fuel inlet channel. This is not unexpected, as the pressure is highest at the base of the fuel inlet. Although there is an imbalance in fuel velocity, the average velocity is still in line with the RPA simulations which suggests that this mismatch is acceptable. The fuel imbalance could be remedied by changing the cross section of the bottom coolant distribution manifold such that the coolant is always traveling at the same velocity regardless of distance from the fuel inlet.

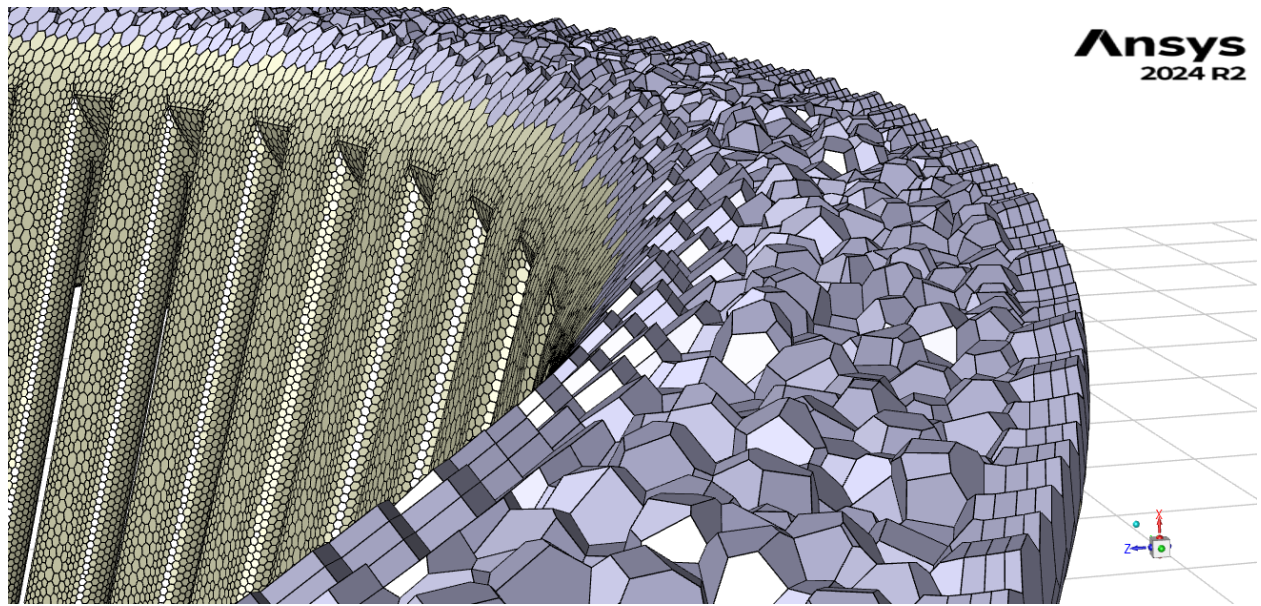


Figure 72: Manifold Mesh Cross Section

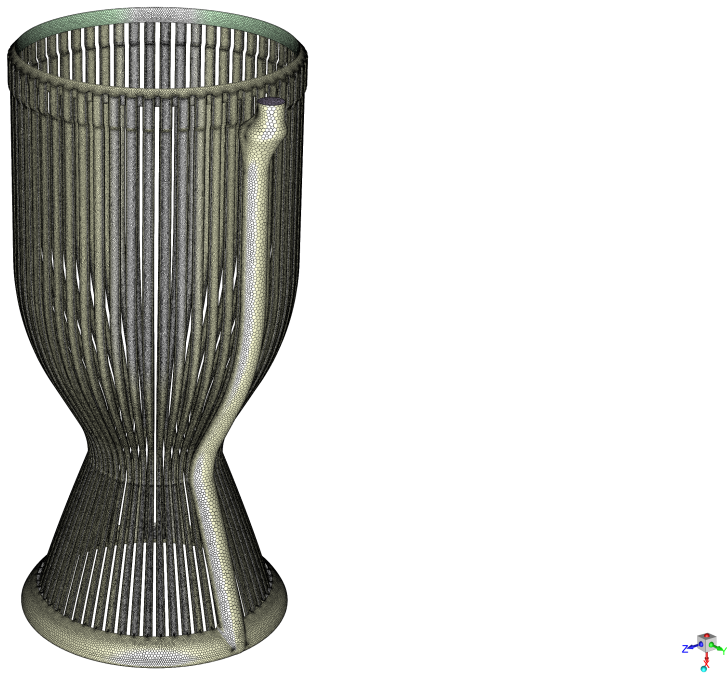


Figure 73: CFD Surface Mesh

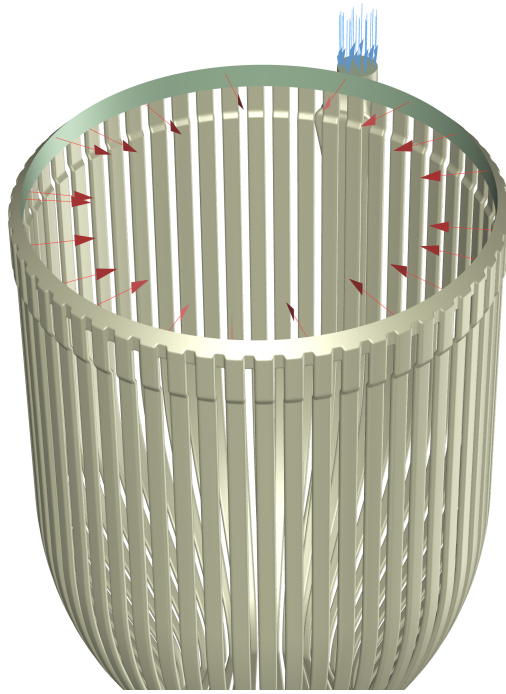


Figure 74: Mass Flow Rate Inlet and Outlet

## 17.1 Pressure Loss Results

The pressure loss across the fuel flow path was measured by taking the difference in pressure between the inlet and outlet. The resulting pressure drop is approximately 80 PSI. Inlet pressure: 552909 pa Outlet pressure: 722 pa Pressure drop= 80 PSI

The pressure loss calculated by hand was 24.76 PSI, which is around a third of what was calculated in FLUENT. The pressure loss calculated by RPA was 6.15 PSI.

# 18 Material Properties and Considerations

## 18.1 AlSi10Mg Properties

The analysis utilized AlSi10Mg aluminum alloy material properties, with particular attention to temperature-dependent characteristics. The material exhibits significant variation in mechanical properties at elevated temperatures:

Different values of yield strength (YS) and ultimate tensile strength (UTS) are reported by various manufacturers. The analyzed sample had been stress relieved, resulting in relatively lower strength values compared to other processing conditions.

According to XMake (the manufacturing partner), their as-built AlSi10Mg has the following properties:

- Tensile strength (horizontal direction):  $430 \pm 20$  MPa

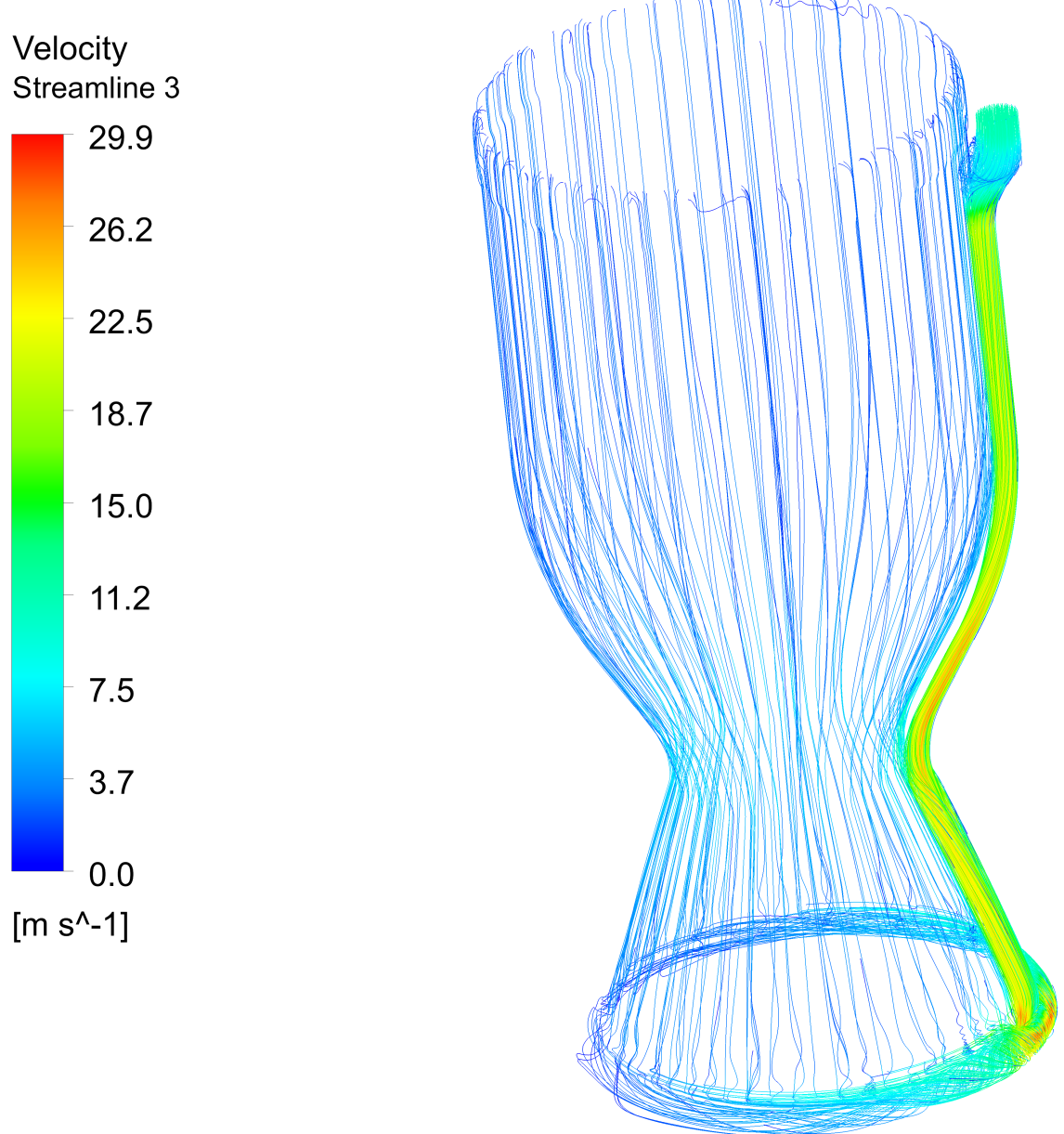


Figure 75: Coolant Velocity Streamlines

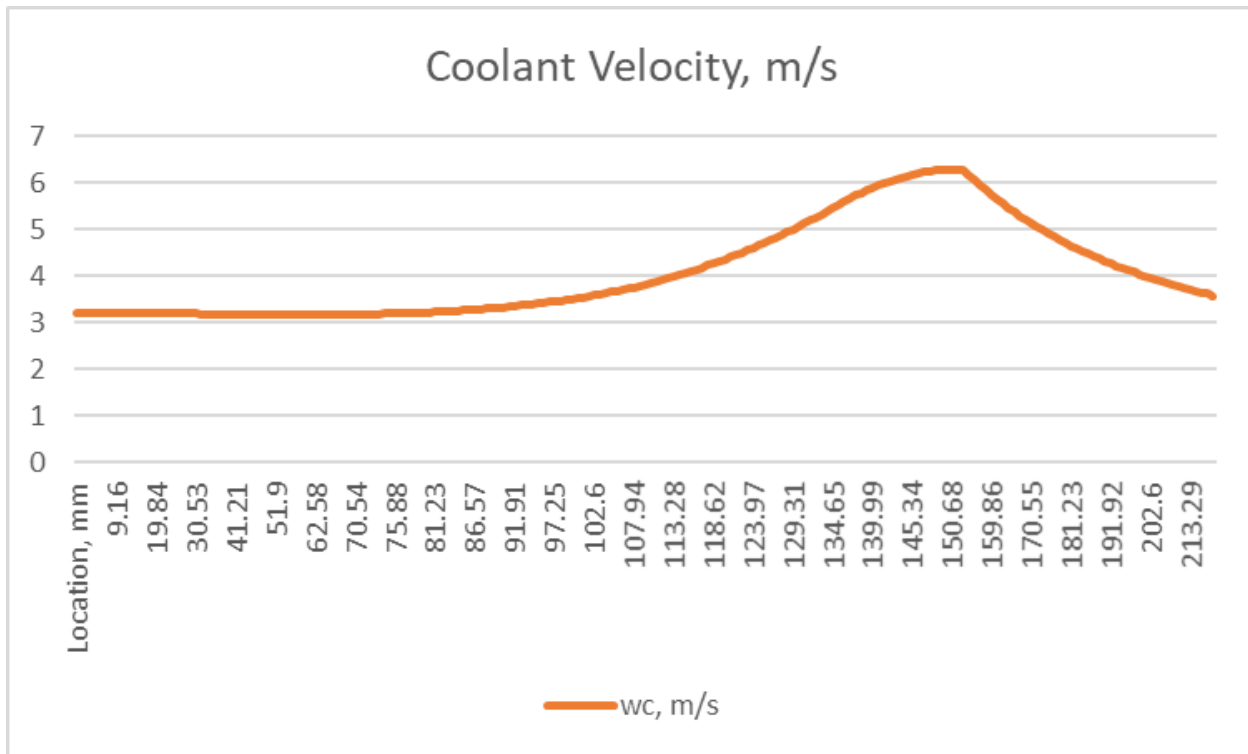


Figure 76: RPA Coolant Velocity Graph

Table 10: Temperature-dependent mechanical properties of AM-SLM AlSi10Mg specimens

Temperature (°C)	Elastic Modulus ( $E$ , GPa)	Yield Stress (YS, MPa)	Ultimate Tensile Stress (UTS, MPa)	Elongation at fracture ( $\varepsilon_f$ , %)
25	77.6	204	358	7.2
50	75.5	198	341	8.5
100	72.8	181	286	10.0
150	*	182	241	14.7
200	*	158	189	16.4
250	*	132	149	30.9
300	*	70	73	41.4
350	*	30	33	53.8
400	*	12	14	57.4

\* Young's modulus cannot be determined accurately above 100°C.

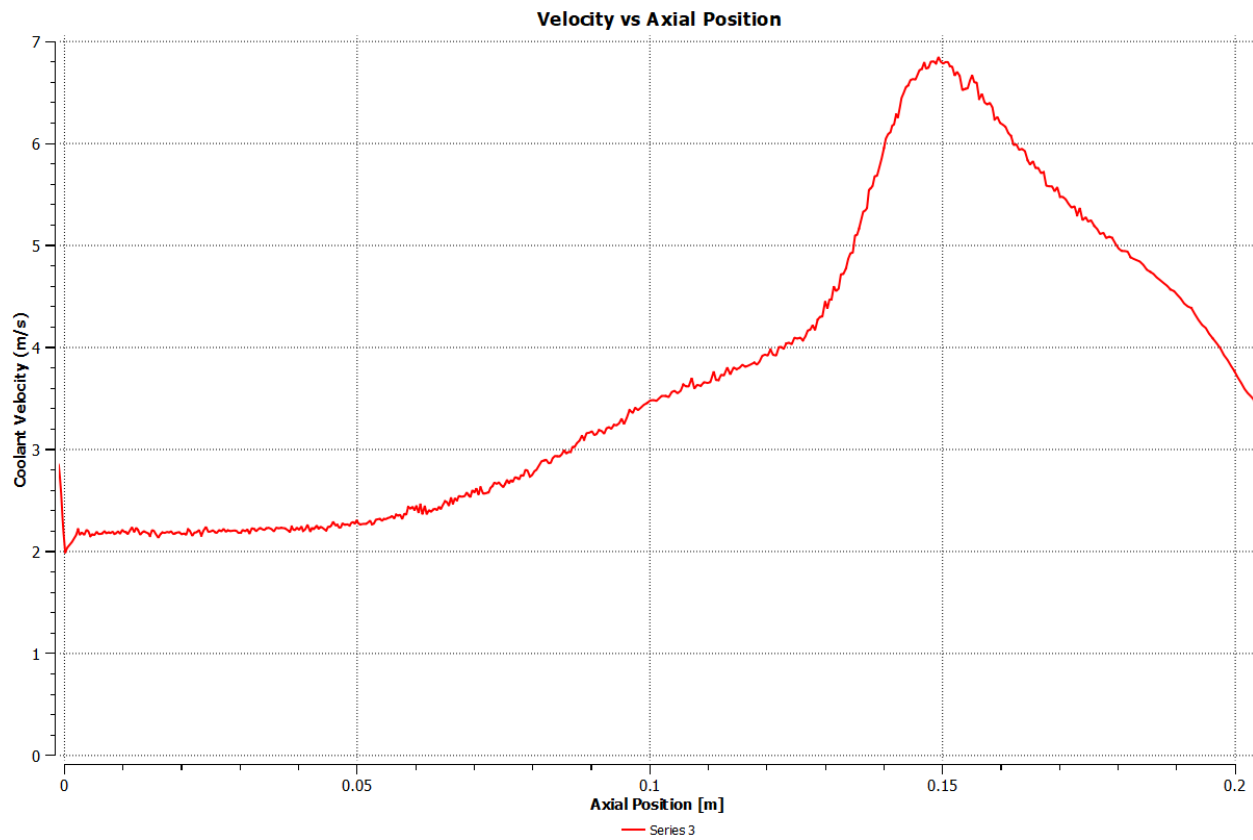


Figure 77: Single Streamline Velocity vs Axial Position

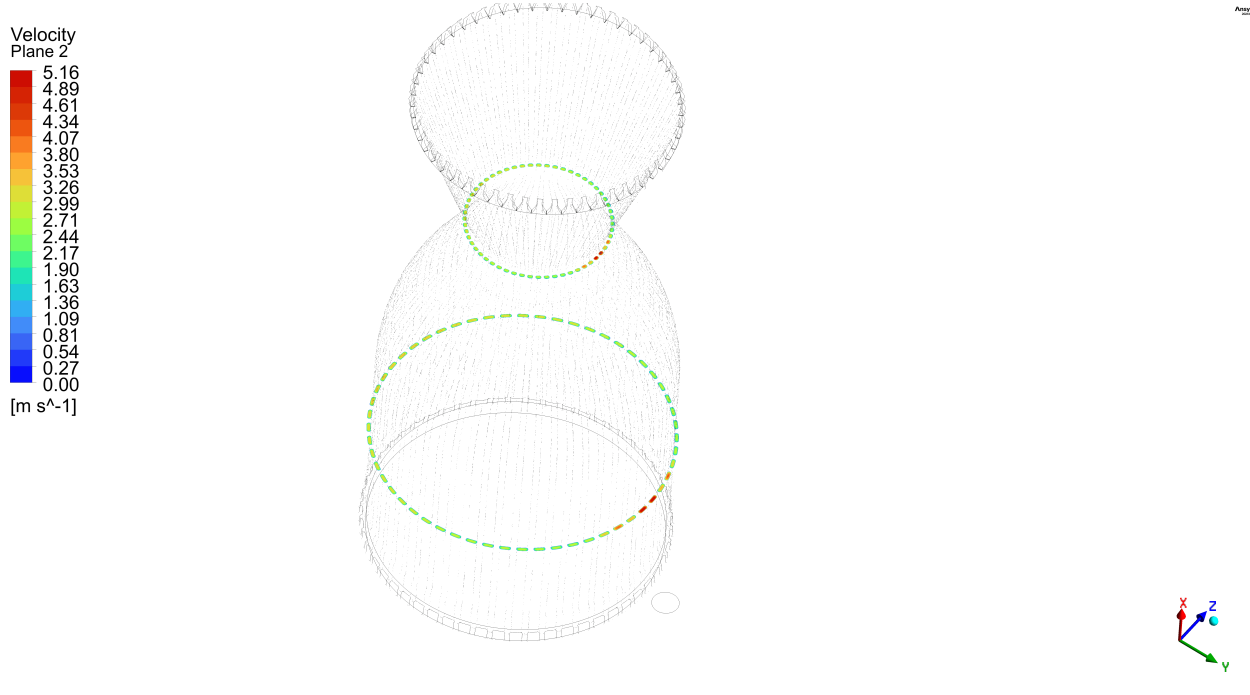


Figure 78: Velocity Cross Sectional Profiles

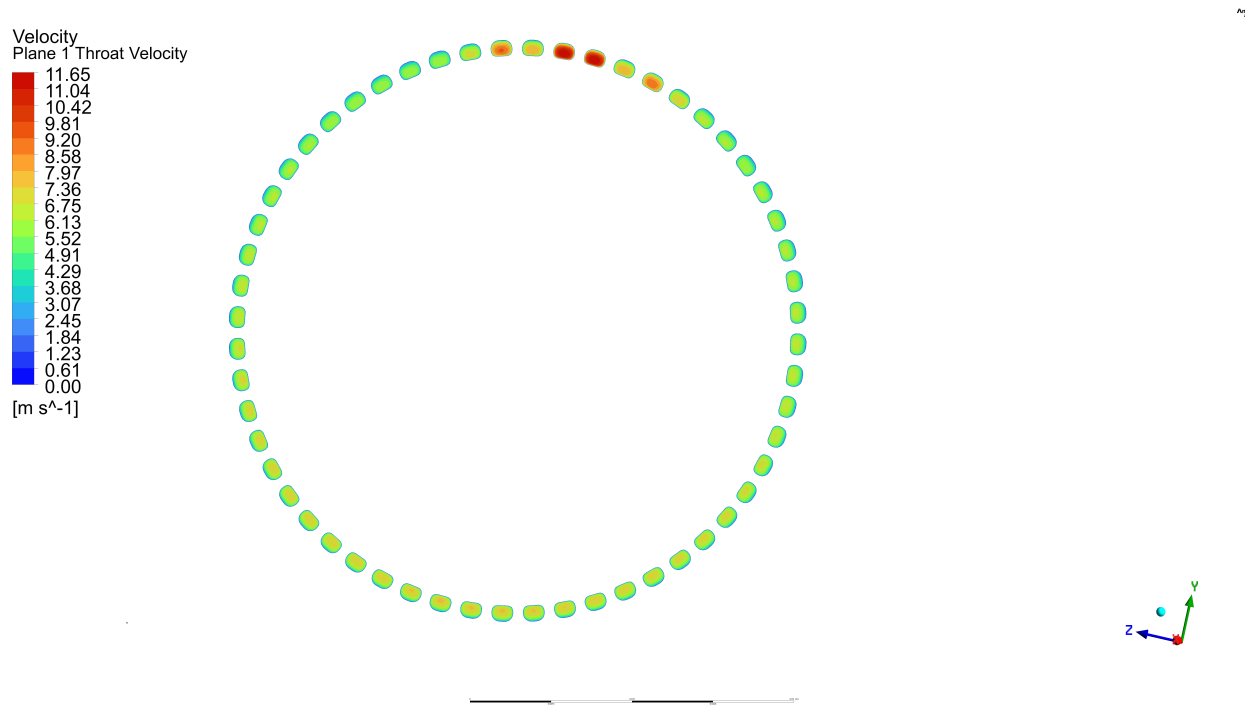


Figure 79: Throat Velocity Profiles

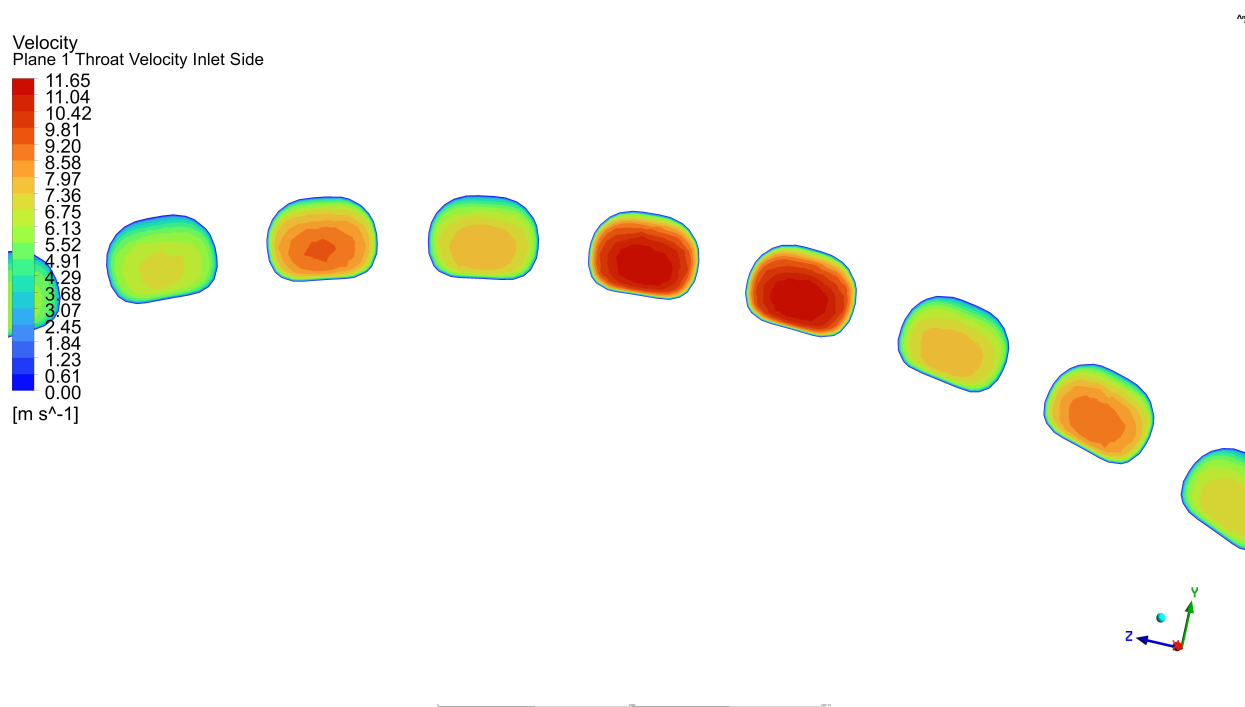


Figure 80: Throat Velocity Inlet Side

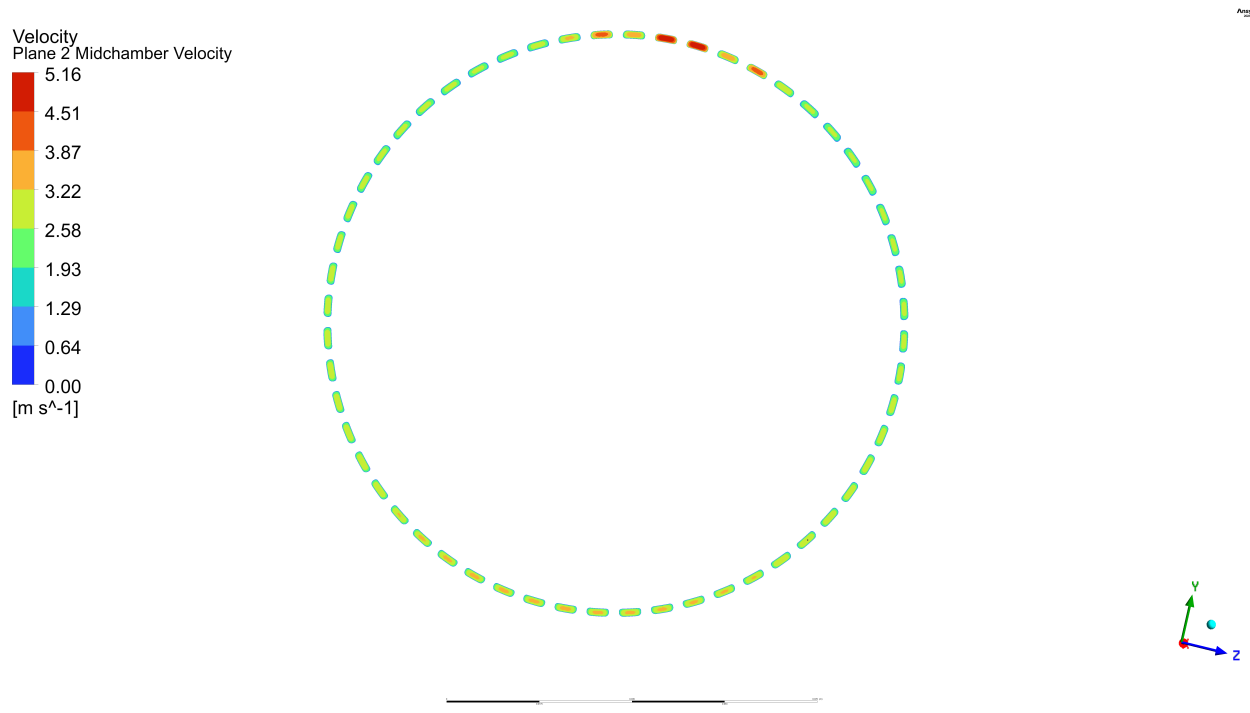


Figure 81: Midchamber Velocity

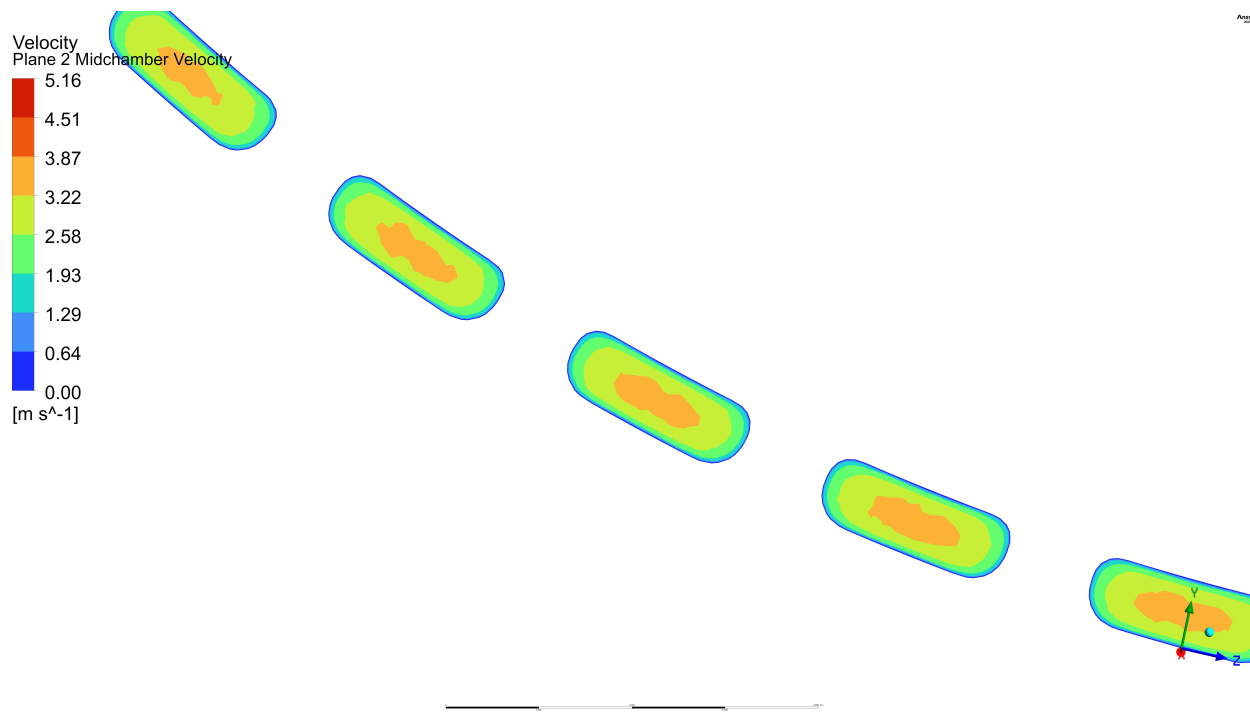


Figure 82: Midchamber Velocity Far From Inlet

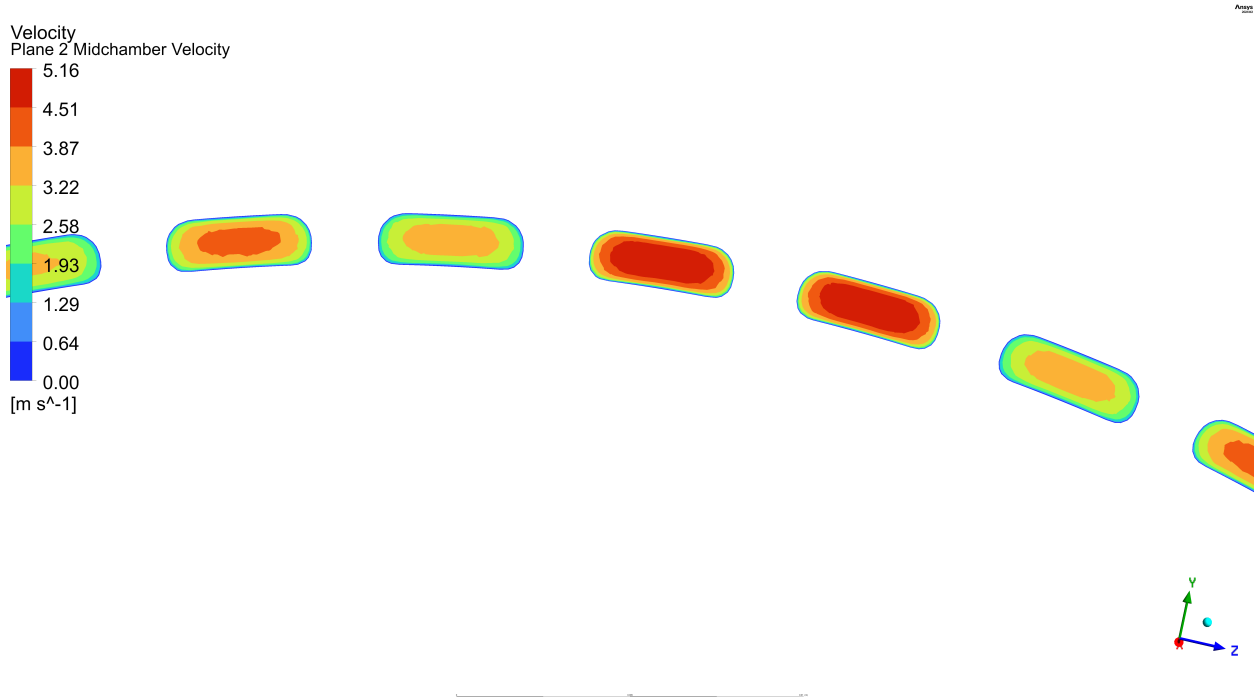


Figure 83: Midchamber Velocity Close to Inlet

- Yield strength:  $245 \pm 10$  MPa
- Elastic modulus:  $70 \pm 5$  GPa
- Elongation:  $9 \pm 2\%$
- Hardness:  $120 \pm 5$  HV
- Long-term operating temperature: Below 250°C

XMake did not provide yield strength vs temperature, however the ANSYS AlSi10Mg material card has a similar yield strength at room temperature. Therefore, it can be assumed that the ANSYS material will perform similarly to how the Xmake material will under higher temperatures. The ANSYS data is used for all yield safety margin calculations in this report.

## 18.2 Thermal Conductivity Considerations

Thermal conductivity was modeled as  $110 \text{ W/m} \cdot \text{K}$  for the analysis. Research indicates that heat treatment can significantly improve the thermal performance of AlSi10Mg [8]:

- Post-manufacture annealing eliminates thermal conductivity anisotropy present in the as-built condition
- Annealing enhances conductivity by approximately 30% in the transverse direction

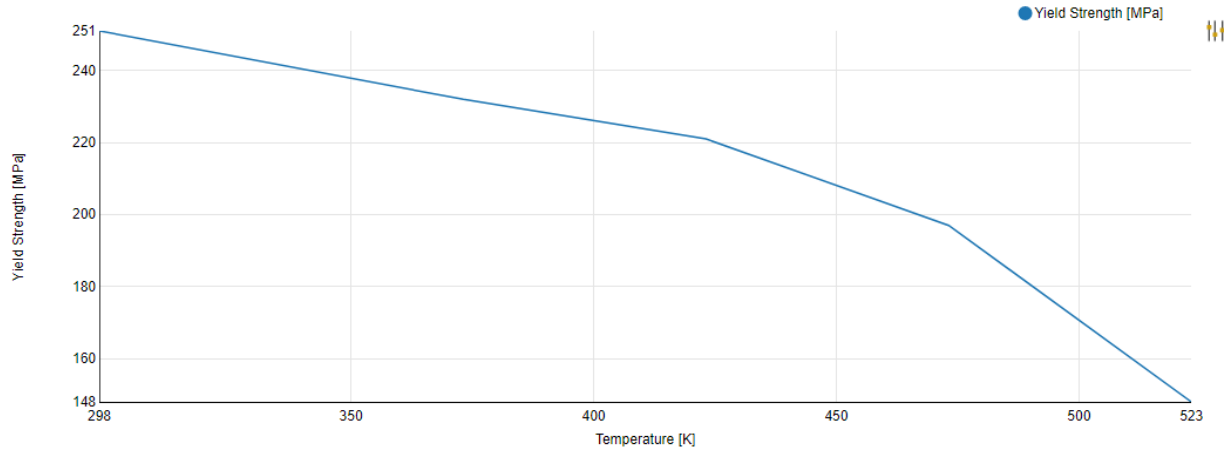


Figure 84: AlSi10Mg Yield Strength vs Temperature GRANTA

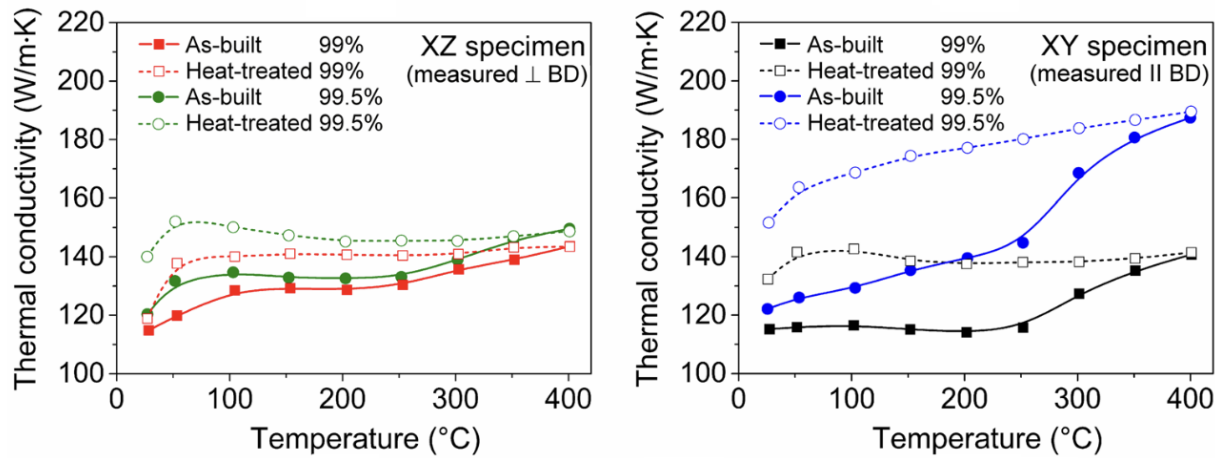


Figure 85: Thermal Conductivity vs Temperature [8]

- Solution heat treatment increases thermal conductivity by 36% compared to as-built
- T6-like treatment provides the greatest improvement (44% over as-built) [8]

If the printed component were heat treated to bring thermal conductivity closer to 140 W/m · K, peak temperatures would be reduced by approximately 10 K to 455 K. This improvement is related to the evolution of the AlSi10Mg microstructure, particularly the breakdown of the Si cellular structure. The EOS T6 temper appears to be the optimal heat treatment for more uniform material properties.

According to XMake (the manufacturing partner), their as-built AlSi10Mg has the following properties:

- Tensile strength (horizontal direction):  $430 \pm 20$  MPa
- Yield strength:  $245 \pm 10$  MPa
- Elastic modulus:  $70 \pm 5$  GPa

- Elongation:  $9 \pm 2\%$
- Hardness:  $120 \pm 5$  HV
- Long-term operating temperature: Below  $250^\circ\text{C}$

## 19 Manufacturing Process

The engine will be printed nozzle side down using a Han metal 3D printer. Critical features such as the injector interface bore on the chamber will require post-machining according to the detailed engineering drawings per Appendix B, “Liquid-Engine Chamber Post-Processing Report”. To achieve the correct dimensions after machining, the 3D printed model was modified to incorporate additional material around the bore.

The manufacturing model also has the bolt holes removed, as these will be drilled and tapped during the post-machining process. This approach ensures proper thread engagement and dimensional accuracy for critical fastening features.

As of 5/18/25 the engine has been 3D printed, and is now undergoing post process machining at XMAKE in China.

## 20 Future Work

- **Additional Computational Fluid Dynamics (CFD) and flow-path optimization:** perform CFD simulations on the internal flow path through the injector body.
- **Injector design optimization:** improve the pintle injector to enhance fuel–oxidizer mixing and investigate optimal momentum ratios; explore methodologies for independent throttling of fuel and oxidizer while maintaining stable combustion.
- **Throttle-control investigation:** investigate mechanical and flow-based solutions to independently throttle fuel and oxidizer, enabling dynamic thrust modulation; evaluate thermal-management strategies under varying throttle conditions to prevent overheating at low power levels.
- **Instrumentation integration:** evaluate the integration of thermocouples and pressure transducers for real-time chamber-condition monitoring.
- **Manufacturing validation:** inspect the combustion chamber through dimensional measurements; send the injector body to Xmake for manufacturing.

## **A Manufacturing Drawings**

## **B Supporting Documents**

### **B.1 Liquid-Engine Chamber Post-Processing Report**

DESCRIPTION	DATE	APPROVED
Liquid Engine Chamber	4/22/25	N/A

The technical drawing illustrates a mechanical assembly. On the left, a vertical support structure is shown with dimensions: height 0.450, thickness 0.097, and a top hole diameter of  $\phi 0.508$ . The support features a flange at the bottom. A curved track is attached to the support, forming a transition from a vertical to a horizontal plane. A section view labeled "SECTION A-A" shows a cross-section of the track's profile. A callout provides the following details: a hole diameter of  $\phi 0.508 \downarrow 0.320$ , a thread specification of 9/16-18 UNF 2B, and angles of 45° and 12° indicated by arcs.

# SECTION F-F

## SCALE 1:1.5

Technical drawing showing a cross-sectional view of a mechanical part. The part features a top surface with a central rectangular cutout and a series of vertical slots along its bottom edge. A note on the left specifies "Break Edges, 0.005" Radius Typical". Key dimensions include:

- Width of the main body: 0.235
- Height of the main body: 0.483
- Total height: 0.813
- Width of the central cutout: 0.040
- Radius of the top corner: 0.01
- Angle of the top transition: 45°
- Angle of the bottom corner: 30°
- Width of the bottom slot area: 0.010
- Radius of the bottom corner: 0.005

Material is indicated by diagonal hatching.

ALL DIMENSIONS IN  
INCHES

ALL DIMENSIONS IN INCHES		APPROVALS	DATE	 Cornell Rocketry Team 124 Hoy Road Ithaca, NY 14853 <a href="http://www.cornellrocketryteam.com">www.cornellrocketryteam.com</a>
		DRAWN: Caleb Farrelly	4/22/25	
		CHECKED:		
		ANALYSIS:		
THIRD ANGLE PROJECTION	MANUFACTURING:		PARENT ASSEMBLY:	REVISION:
	APPROVED:			03
DEFAULT TOLERANCES: .X = ± .025 .XX = ± .01 .XXX = ± 0.005				

8

7

6

5

4

3

2

1

DESCRIPTION

DATE

APPROVED

D

D

C

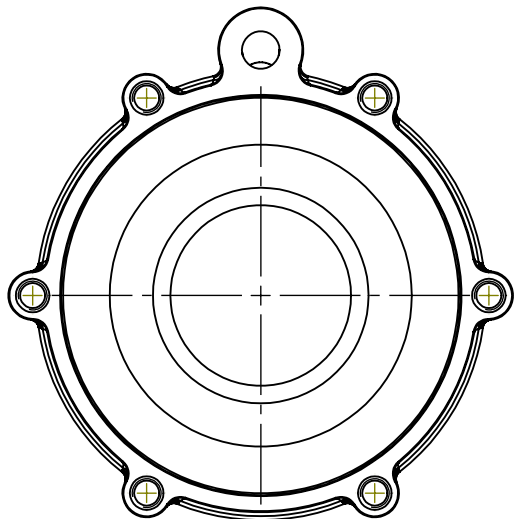
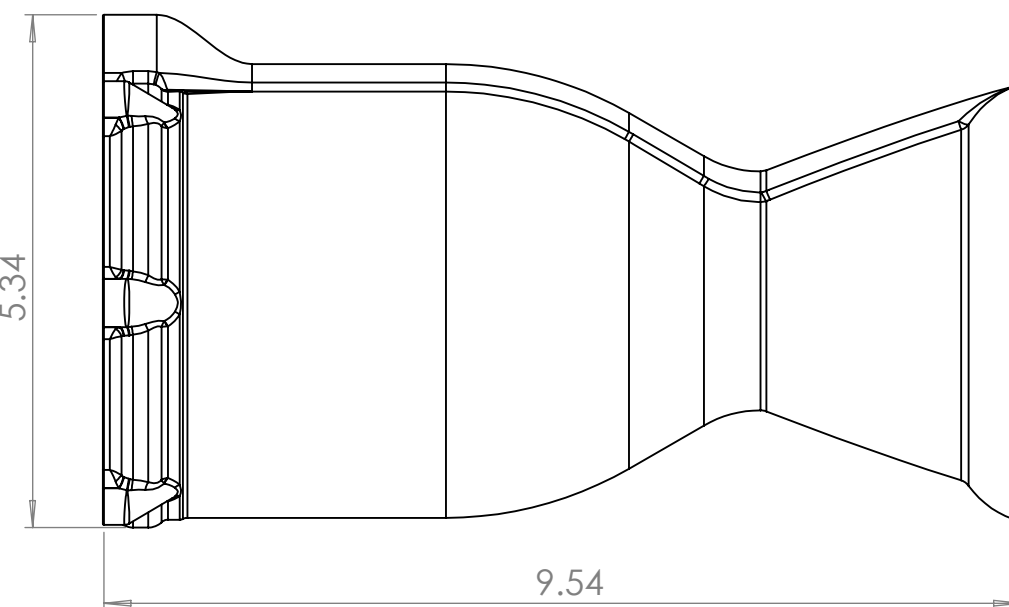
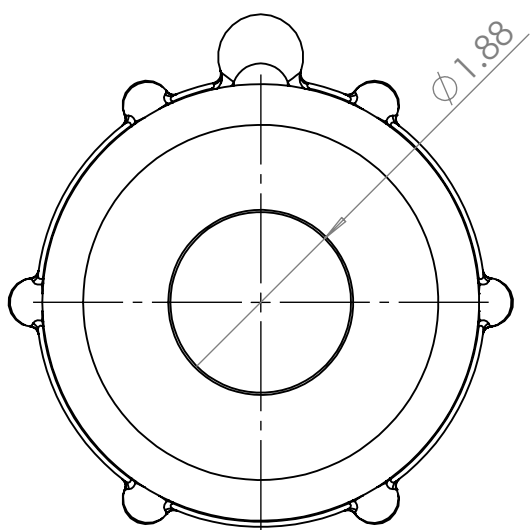
C

B

B

A

A



ALL DIMENSIONS IN INCHES

MATERIAL: AISI10Mg  
FINISH: Sand BlastedDEFAULT TOLERANCES:  
.X = ± .025  
.XX = ± .01  
.XXX = ± 0.005

THIRD ANGLE PROJECTION

APPROVALS

DATE

DRAWN:

4/21/25

CHECKED:

ANALYSIS:

MANUFACTURING:

APPROVED:

Cornell Rocketry Team  
124 Hoy Road  
Ithaca, NY 14853  
[www.cornellrocketryteam.com](http://www.cornellrocketryteam.com)

DOCUMENT TITLE:

Combustion Chamber

PARENT ASSEMBLY:

REVISION:

8

7

6

5

4

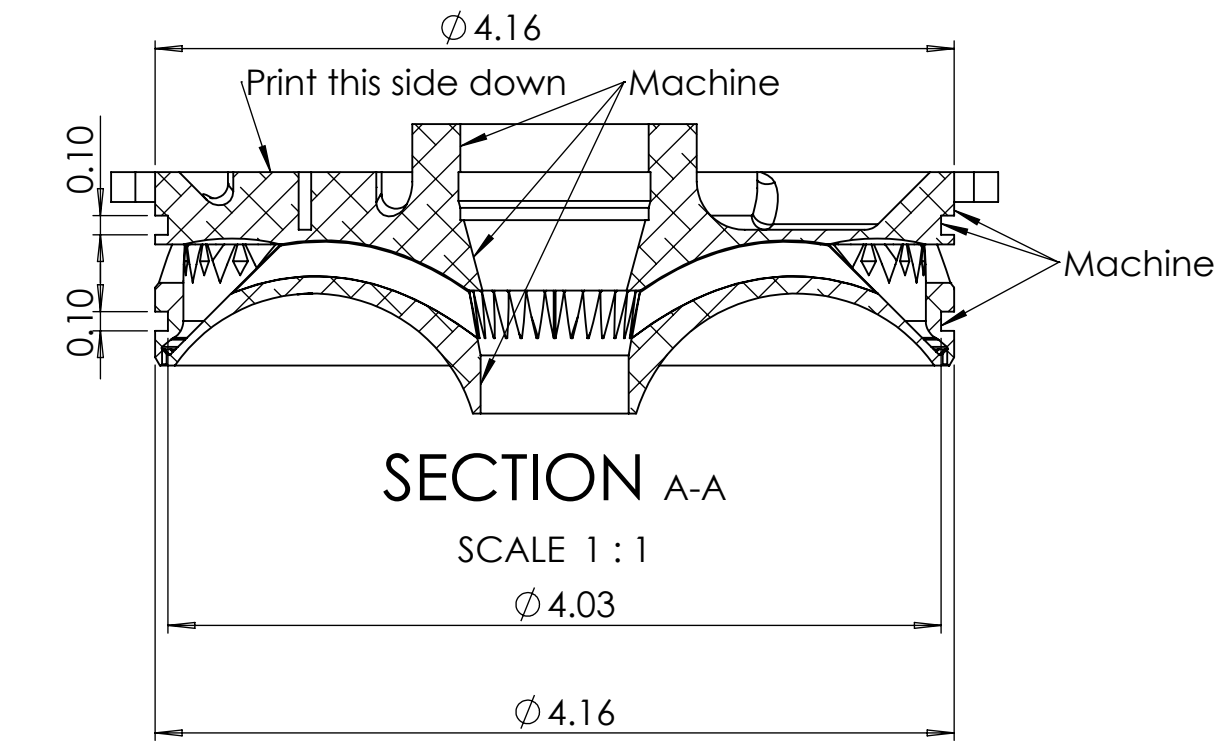
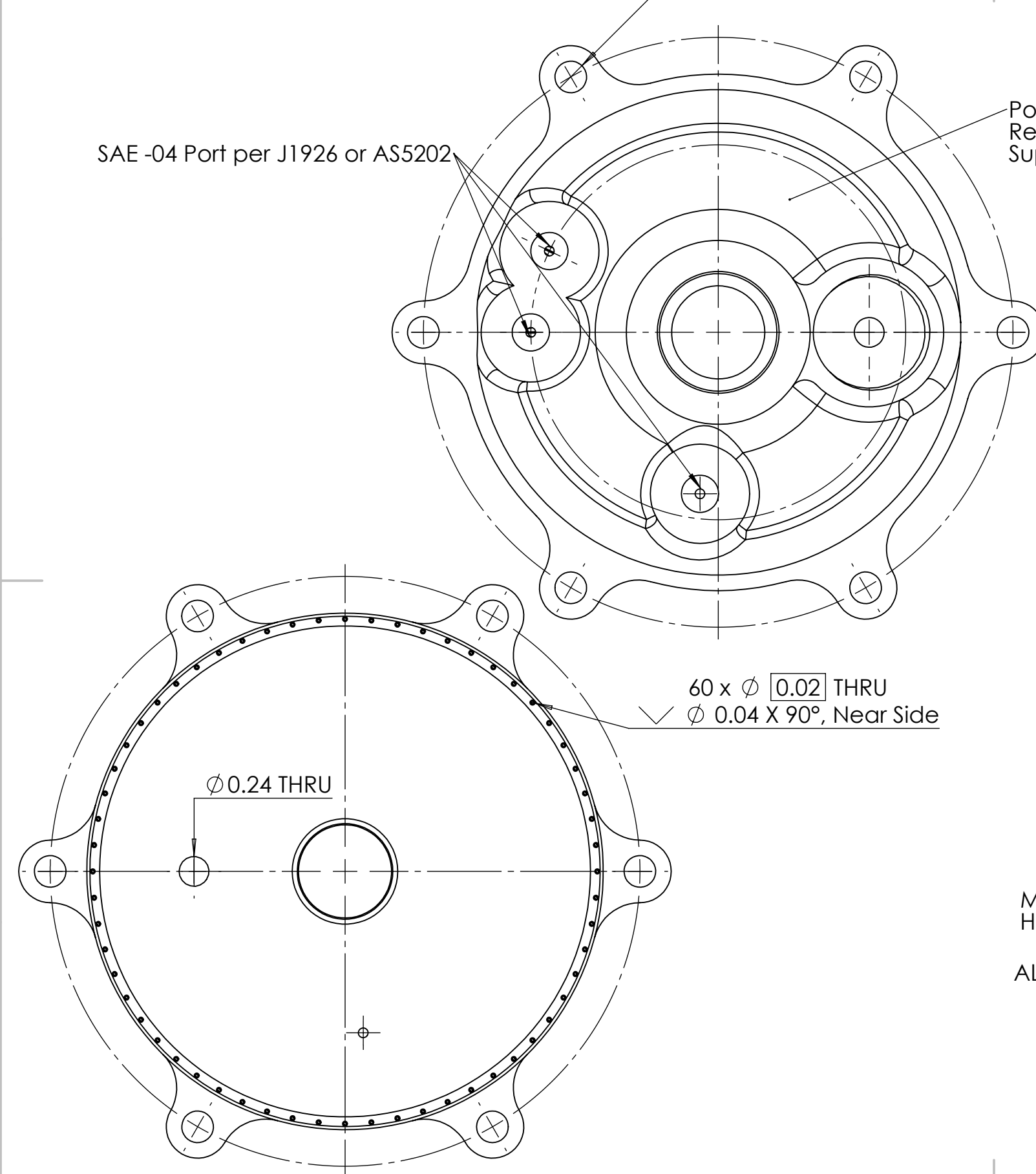
3

2

1

DESCRIPTION	DATE	APPROVED
-------------	------	----------

# ROUGH DRAFT- NOT FOR PRODUCTION



Metal 3D print from AISI10Mg  
High Quality Print Settings

ALL DIMENSIONS IN INCHES

DEFAULT TOLERANCES:  
.X = ± .025  
.XX = ± .01  
.XXX = ± 0.005

THIRD ANGLE PROJECTION

APPROVALS	DATE	Cornell Rocketry Team 124 Hoy Road Ithaca, NY 14853 www.cornellrocketryteam.com
DRAWN:		
CHECKED:		
ANALYSIS:		
MANUFACTURING:		
APPROVED:		
		DOCUMENT TITLE: <b>Injector Post Processing</b>
		PARENT ASSEMBLY:      REVISION:

## C MATLAB Scripts for Engine Analysis

This appendix contains the MATLAB scripts used for various calculations related to the design of the 1250 lbf bipropellant rocket engine. These scripts include fuel flow calculations, cooling channel analysis, and structural stress analysis.

```
clc; clear;

% === Input Parameters ===
% === Ethanol Flow Through Annular Orifice ===
% Given Data
Cd = 0.82;           % Discharge coefficient
rho = 780;           % Density of ethanol (kg/m^3)

% Orifice Inner Diameter in Inches (Given)
d_inner_in = 0.74525; % Inner diameter of orifice (inches)

% Desired Mass Flow Rate in kg/s
desired_mass_flow_kg_s = 0.68; % Desired mass flow rate (kg/s)

% Pressure in PSI
P1_psi = 700;         % Upstream pressure (PSI)
P2_psi = 350;         % Downstream pressure (PSI)

% Convert Units
P1 = P1_psi * 6894.76; % Upstream pressure (Pa)
P2 = P2_psi * 6894.76; % Downstream pressure (Pa)
deltaP = P1 - P2;      % Pressure drop (Pa)
d_inner = d_inner_in * 0.0254; % Inner diameter in meters

% Solve for Pintle Gap
syms pintle_gap
d_outer = d_inner + 2 * pintle_gap; % Outer diameter in meters
A = pi * (d_outer^2 - d_inner^2) / 4; % Annular area (m^2)

% Flow Equation: Mass Flow Rate = rho * Cd * A * sqrt(2 * deltaP / rho)
Q_m3s = Cd * A * sqrt(2 * deltaP / rho); % Volumetric flow rate (m^3/s)
mass_flow_eq = rho * Q_m3s;                 % Mass flow rate (kg/s)

% Solve for Pintle Gap
solution = vpasolve(mass_flow_eq == desired_mass_flow_kg_s, pintle_gap);
solution = max(solution); % Take the first valid solution
pintle_gap_in = double(solution / 0.0254); % Convert to inches

% Display Results
fprintf('Ethanol Flow Through Annular Orifice:\n');
fprintf(' - Desired Mass Flow Rate: %.2f kg/s\n', desired_mass_flow_kg_s);
fprintf(' - Pressure Drop: %.2f PSI\n', P1_psi - P2_psi);
```

```

fprintf(' - Pintle Gap: %.6f m (%.6f inches)\n', double(solution),
        → pintle_gap_in);

% === Cooling Calculations ===
% Chamber Data
chamber_flux = 3.2574; % Chamber mass flux (kg/s) from RPA
cooling_fraction = 0.053; % Fraction of fuel for film cooling
fuel_injector_mdot = 0.6786; % Fuel mass flow rate from injector (kg/s)

% Coolant Mass Flow Rate
cool_film_mdot = cooling_fraction * chamber_flux;
total_fuel_mass_flow_rate = fuel_injector_mdot + cool_film_mdot;

% Percent of Fuel Used for Regenerative Cooling
percent_regen = total_fuel_mass_flow_rate / chamber_flux;

% === Fluid Properties of Ethanol ===
mu = 0.001095; % Dynamic viscosity (Pa·s) at ~20°C
epsilon = 60e-6; % Aluminum surface roughness for 3D printing (m)

% === Cooling Channel Geometry ===
channel_length = 0.25; % Channel length (m)
num_channels = 58; % Number of cooling channels
A_channel = 2.66291e-6; % Cross-sectional area per channel (m^2)
P = 5.938e-3; % Perimeter from CAD model (m)

% Perimeter was calculated by taking the cross-section of the cooling
% channels at the smallest area, around the throat. Smaller channels at the
→ throat
% increase flow velocity, enhancing heat transfer from the walls to the fluid.

% Calculate Hydraulic Diameter
D_h = 4 * (A_channel / P);

% Calculate Flow Velocity
Q = total_fuel_mass_flow_rate / (rho * num_channels);
v = Q / A_channel;

% Calculate Reynolds Number
Re = (rho * v * D_h) / mu;

% === Friction Factor Calculation ===
if Re < 2300
    f = 64 / Re; % Laminar flow
elseif Re >= 4000
    % Turbulent flow using Colebrook-White equation
    syms f_sym

```

```

colebrook_eq = -2 * log10((epsilon/(3.7*D_h)) + (2.51/(Re*sqrt(f_sym)))) ==
    1/sqrt(f_sym);
f = double(vpasolve(colebrook_eq, f_sym, 0.02));
else
    % Transitional flow (Blasius approximation)
    f = 0.079 * Re^(-0.25);
end

% Calculate Pressure Drop Using Darcy-Weisbach Equation
deltaP_Pa = f * (channel_length / D_h) * (rho * v^2 / 2); % Pressure drop (Pa)
deltaP_PSI = deltaP_Pa / 6894.76; % Pressure drop (PSI)

% === Orifice Calculations for Film Cooling ===
% Film coolant mass flow rate
orifice_diameter = 0.4e-3; % Orifice diameter (m)
Cd_orifice=0.6; %typical sharp edged orifice
A_orifice = pi * (orifice_diameter / 2)^2; % Orifice cross-sectional area (m^2)

% Flow Rate Through One Orifice
syms orifice_mdot
orifice_eq = rho * Cd * A_orifice * sqrt(2 * deltaP / rho) == orifice_mdot;
orifice_mdot_sol = double(vpasolve(orifice_eq, orifice_mdot));

% Calculate Number of Orifices
num_orifices = ceil(cool_film_mdot / orifice_mdot_sol);

% === Display Results ===
fprintf('\nCooling and Flow Results:\n');
fprintf(' - Total Fuel Mass Flow Rate: %.2f kg/s\n', total_fuel_mass_flow_rate);
fprintf(' - Reynolds Number: %.2f\n', Re);
fprintf(' - Flow Velocity: %.2f m/s\n', v);
fprintf(' - Friction Factor: %.4f\n', f);
fprintf(' - Pressure Loss: %.4f Pa (%.4f PSI)\n', deltaP_Pa, deltaP_PSI);
fprintf(' - Film Coolant Mass Flow Rate: %.6f kg/s\n', cool_film_mdot);
fprintf(' - Orifice Flow Rate: %.6f kg/s per orifice\n', orifice_mdot_sol);
fprintf(' - Number of Orifices Required: %d\n', num_orifices);

% Determine Flow Regime
if Re < 2300
    fprintf(' - Flow Regime: Laminar\n');
elseif Re <= 4000
    fprintf(' - Flow Regime: Transitional\n');
else
    fprintf(' - Flow Regime: Turbulent\n');
end

```

```

% Cooling Channel Stress Analysis
clc; clear;

% Constants and Inputs
pc = 350 * 6895; % Chamber pressure (Pa) from psi
fp = 1000 * 6895; % Fuel MEOP (Pa) from psi
t = 0.0015; % Cooling channel min wall thickness (m)
ri = 0.046; % Inner radius of the cooling channel (m)
sf = 1.5; % Safety factor
yall = 125e6; % Allowable material yield strength (Pa) at 250c for EOS EOS
    ↳ Aluminium AlSi10Mg

% Cooling Channel Inside Stress
rcooling = 0.0015; % Cooling channel width (m)
sigcool = (pc * sf * rcooling / t) / 1e6; % Cooling channel stress (MPa)
margincool = (yall / (sig * 1e6)) - 1; % Safety margin

% Fuel distribution manifold stress calculation
ptank = 800 * 6895; % Fuel tank pressure (Pa)
sig = (pc * sf * ri / t) / 1e6; % Main wall stress (MPa)
margin = (yall / (sig * 1e6)) - 1; % Safety margin

% Cooling Mass Flux Calculations
coolf = 0.053; % Cooling mass fraction
chamberflux = 3.2574; % Chamber flux (kg/s)
coolmflux = coolf * chamberflux; % Cooling mass flux (kg/s)
fuel = 0.6786; % Base fuel flow (kg/s)
totalfuel = fuel + coolmflux; % Total fuel flow (kg/s)
percentregen = totalfuel / chamberflux; % Regen fuel percentage

% Convert wall thickness to thousandths of an inch
thou = t * 1000 * 39.37; % Wall thickness in thousandths of an inch

% Cooling Channel Pressure Data
pout = 6.1629; % Outlet pressure (MPa)
pin = 6.20528; % Inlet pressure (MPa)
dpcool = (pin - pout) * 145; % Pressure drop in cooling channel (psi)

% Display Results
fprintf('Structural and Flow Analysis Results:\n');
fprintf(' - Cooling Channel Stress: %.2f MPa\n', sigcool);
fprintf(' - Main Wall Stress: %.2f MPa\n', sig);
fprintf(' - Safety Margin: %.2f%\n', margin * 100);
fprintf(' - Total Fuel Flow: %.4f kg/s\n', totalfuel);

```

```
fprintf(' - Regen Fuel Percentage: %.2f%%\n', percentregen * 100);
fprintf(' - Cooling Channel Pressure Drop: %.2f psi\n', dpcool);
fprintf(' - Wall Thickness: %.2f thou\n', thou);
```

## References

- [1] MIT Rocket Team. (2023). *Topic 6: Injector Design*. Retrieved from <https://wikis.mit.edu/confluence/display/RocketTeam/Topic+6%3A+Injector+Design>.
- [2] HalfCat Rocketry. (2023). *Mojave Sphinx Hybrid Rocket Project*. Retrieved from <https://www.halfcatrocketry.com/mojave-sphinx>.
- [3] Questionable Engineer. (2023). *Questionable Engineer - Rocket Engine Design and Engineering Channel*. Retrieved from <https://www.youtube.com/@QuestionableEngineer>.
- [4] Huzel, D. K., & Huang, D. H. (1971). *Modern Engineering for Design of Liquid Propellant Rocket Engines*. Progress in Astronautics and Aeronautics. American Institute of Aeronautics and Astronautics (AIAA).
- [5] EOS GmbH - Electro Optical Systems. (2023). *Material Datasheet - EOS Nickel Alloy IN718*. Retrieved from [https://vetted3d.com/pdf/materials/material\\_datasheet\\_eos\\_nickelalloy\\_in718\\_en.pdf](https://vetted3d.com/pdf/materials/material_datasheet_eos_nickelalloy_in718_en.pdf).
- [6] Sutton, G. P., & Biblarz, O. (2016). *Rocket Propulsion Elements* (9th ed.). Wiley.
- [7] Waxman, B. S. (2014). *An Investigation of Injectors for Use with High Vapor Pressure Propellants with Applications to Hybrid Rockets* (Ph.D. dissertation). Stanford University. Retrieved from <https://purl.stanford.edu/ng346xh6244>.
- [8] MartínezMaradiaga, D., Mishin, O. V., & Engelbrecht, K. (2020). Thermal properties of selectively laser-melted AlSi10Mg products with different densities. *Journal of Materials Engineering and Performance*, 29(11), 7125–7130. <https://doi.org/10.1007/s11665-020-05192-z>.